AN INVESTIGATION OF SURFACE-TO-BOREHOLE TRAVEL-TIME TOMOGRAPHY FOR MINERAL EXPLORATION

OLUWATOSIN ONABIYI

AN INVESTIGATION OF SURFACE-TO-BOREHOLE TRAVEL-TIME TOMOGRAPHY FOR MINERAL EXPLORATION

by

© Oluwatosin Onabiyi

A thesis submitted to the

School of Graduate Studies

in partial fulfillment of the requirements for the degree of

Masters of Science

Department of Earth Sciences

Memorial University of Newfoundland

June 2013

St. John's Newfoundland

ABSTRACT

This thesis analyses the capabilities of the surface-to-borehole travel-time tomography method as a tool for mineral exploration and resource evaluation. Compared to electrical, electromagnetic, induced polarization and potential field methods, which are the currently preferred geophysical methods used in mineral exploration, the surface-to-borehole tomography methods offers the potential for higher resolution imaging of the subsurface. Despite the potential for improved subsurface imaging, this method has been somewhat untested for mineral exploration purposes.

Assessment of the surface-to-borehole tomography capabilities was done using a series of increasingly realistic geological models. Acoustic finite-difference modeling was used to generate seismic travel-time data for the series of synthetic models and a minimum-structure inversion approach was used to perform the inversions on first-arrival travel-times. Evaluation of the accuracy of the inversion was done by comparing the true models to the slowness tomograms and the observed travel-times to the predicted travel-times.

Through the use of the 2-dimensional synthetic modeling experiments, this thesis successfully demonstrates the potential for deeper and higher resolution subsurface imaging than the currently used geophysical methods. Based on the acquisition parameters (vertical receiver boreholes, 50 – 60 Hz peak source frequency, and velocity contrasts expected for sulfide mineral deposits in hardrock environments), the results from the synthetic data show that resolution in the tomogram is good down to a depth of 40-50% of the borehole used. In addition, only objects on the scale of 100 m – 150 m or greater are resolvable with this method. Also, in comparison to other directions, it was observed that the best resolution in the tomograms is obtained in the direction perpendicular to the raypaths. Furthermore, we demonstrate that improved resolution in a tomogram is obtained by increasing the angular ray coverage of the region and by using structural and slowness constraints to perform the inversion.

ACKNOWLEDGEMENTS

I would like to thank my supervisor Dr. Charles Hurich for providing me with the opportunity and finances required to carry out this research. I also want to thank him for his support, patience and time sacrificed in order to see me through the completion of this thesis. I extend gratitude to my co-supervisor Dr. Colin Farquharson for his academic contribution and his patience in helping me understand a topic which was fairly new to me at the start of my program.

Dr. Peter Lelièvre provided the inversion codes I used in this thesis and many thanks go out to him for developing the code, fixing bugs in a timely manner and for his extra-ordinary patience in answering the multitude of questions I asked about how to use or understand his codes.

I would also like to acknowledge the contributions of Dr. Sharon Deemer for helping me with several ProMAX issues I had over the course of this research. My thanks also go out to SeyedMasoud Ansari for sacrificing time to help me read and edit my thesis. Special thanks go out to Landmark geophysics for providing the ProMAX software used in my research. I also have to acknowledge Jonathan Richard Shewchuk for providing the Triangle program used in my thesis.

Special thanks go out to my family for the never ending support they provided throughout my master's program and in my life as a whole. I also wish to thank my fellow geophysics colleagues for several contributions they provided over the course of my research.

Table of Contents

List of Figures

Chapter 1 : Introduction

Most of the earth's larger and easily accessible mineral deposits have already been discovered and extracted, leaving a reduced number of large deposits available to be explored. Despite the lessened number of larger deposits, industrial and societal demand for mineral commodities continues to grow. In order to satisfy the increasing demand it has become necessary to explore for deeper deposits (Bellefleur et al., 2004). Furthermore, sites previously mined are being re-assessed to ensure that all available resource has been fully extracted.

For many decades, gravity, electromagnetic (EM), induced polarization (IP), and several other potential field methods have been the tools of choice for mineral exploration. Although electromagnetic and potential fields methods work well at shallow depths (<500m), they are inhibited by their limitations due to their sensitivities and lack of resolving power with increasing depth (Eaton et al., 2003). When compared to potential field methods, seismic methods retain their resolution better with depth and therefore offer the best alternative for exploring minerals at depth. Conventional seismic reflection methods, which have been successfully used in the oil and gas industry for mapping stratigraphy and structure in the subsurface, have had limited use in mineral exploration (Eaton et al., 2003). Reflection seismology in mining suffers due to the structural complexity of hardrock geology as well as low signal-to-noise ratios. In addition, acoustic impedance contrasts in the hardrock environment are not always large enough (>6%) to resolve rock interfaces (Salisbury and Snyder, 2007). Hence the best results using seismic methods are obtained by carefully designed surveys as well as modifications to existing styles of survey (Salisbury and Snyder, 2007).

As an alternative to seismic impedance based techniques such as reflection seismology, velocity based travel-time tomography techniques have occasionally been used to image the subsurface (Mao and Stuart, 1997). Seismic travel-time tomography makes use of arrival times of transmitted waves to estimate subsurface velocity distribution (Lee, 1990). Travel-time tomography, being a seismic based technique, possesses the characteristic of maintaining its resolution with depth because seismic waves retain most of their frequency content with depth. Seismic tomography differs from conventional reflection seismic methods because it uses only travel-time information for imaging rather than impedance contrast. Tomography methods image volumes of rocks in the subsurface while reflection seismology images rock interfaces in the subsurface.

This thesis aims to evaluate the capabilities of surface-to-borehole travel-time tomography as a tool for mineral resource delineation. In addition to these capabilities, the parameters used for generating optimal results using surface-to-borehole tomography will be analysed. The geometry (figure 1.1) has been relatively unused for inversion purposes despite some of the advantages it potentially possesses. A major advantage of this configuration is the possibility to scan across a large area of the subsurface and in multiple directions around a borehole, this is particularly important in an exploration sense because it helps in the delineation of geology surrounding a borehole.

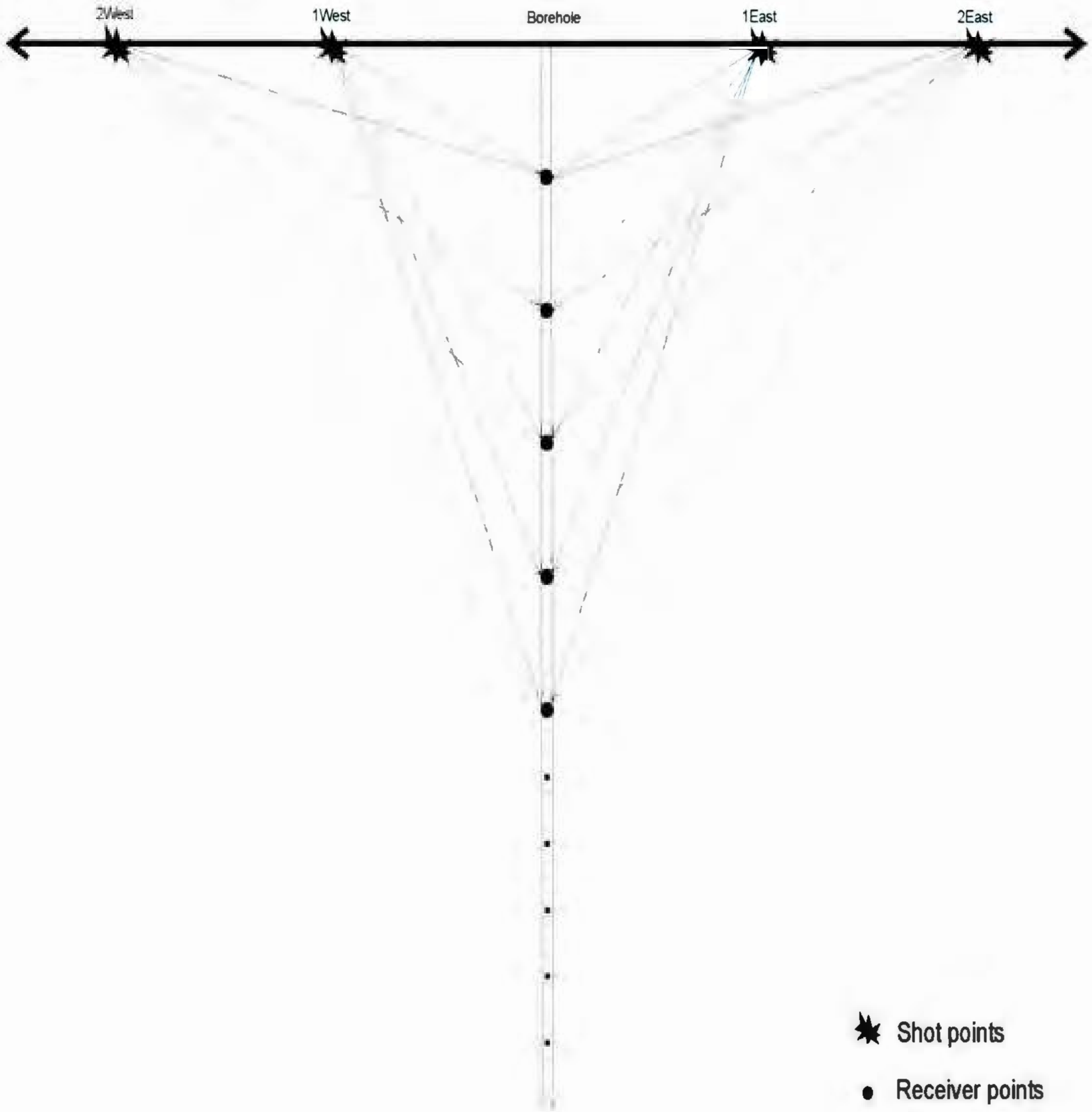

Figure 1.1: Experiment geometry and subsurface ray coverage of surface sources and receivers in a borehole

To carry out the evaluation of this geometry for tomography, a series of synthetic models with increasing complexity was generated. The first few models were designed to determine the resolution, depth and size, to which objects can be resolved. The second series of models was created to test a variety of geometries and orientations of typical environments encountered in a mining setting. The last series of models also mimicked real geology, but they incorporated a near-surface overburden layer as well. As part of the evaluation, field data collected from the Voisey's Bay mine in Labrador were inverted and analysed.

The approach to obtaining results for this study included generating travel-time data by the forward modeling of the synthetic geologic models. After the models were designed, the rock units were assigned velocity values as desired and forward modeling was carried out to create shot records. Following the creation of shot records, the first arrival travel-times to be used for inversions were picked. First arrival travel-times carry information about the rocks they propagate through between the sources and receivers. First arrivals are traditionally preferred over later arrivals because they incur less interference from other waves and still contain important velocity information of the rocks which they travel through; they were also the most consistent travel-times to pick on a shot record. Following the picking of the travel-times, they were inverted to generate slowness tomograms of the subsurface. For this study, the inversion method of preference was the minimum-structure inversion. Minimum-structure inversions produce smeared images of the targets in the subsurface but overall usually reproduce the target objects in their approximate locations in the subsurface and the method is generally reliable and robust (Lelièvre et al., 2011b).

1.1: Review of Literature

After an extensive search for literature pertaining to previous surface-to-borehole tomography experiments, it was discovered that very little work using this configuration has been published in hardrock exploration. The majority of the work done using travel-time tomography has been focused primarily on cross-well tomography, for estimating the velocity variation between two boreholes, or surface-to-surface (wide-angle refraction) tomography, used to analyse the geology of the earth's crust and upper mantle.

In comparison to surface-to-borehole geometry with a dominant frequency of up to 100Hz (Wardell, 1970), the cross-well method and wide-angle refraction technique operate on much different acquisition and resolution scale. For instance, the typical dominant frequency used for cross-well methods can range from several kHz (Harris 1989) to tens of kHz (Abdalla et al., 1990) while frequencies used for wide-angle tomography can be as low as 5Hz. With seismic resolution increasing as the frequency content of the source wavelet increases (Widess, 1973), it is expected that the cross-well method will have a higher resolution potential than the surface-to-borehole geometry which, in turn, will have a higher resolution than the wide-angle refraction tomography. In addition to resolution related items, cross-well tomography surveys require 2 boreholes , and that they be in close range to one another (typically 100-1000m), while the area examined by a wide-angle refraction tomography survey is usually on the scale of a few kilometers to tens of kilometers in depth. The survey area for surface-to-borehole tomography surveys will fall within the range of just a few kilometers, based on the frequency content of the source signal used.

Previous work done using surface-to-borehole geometry for inversion dates as far back as 1983 when McMechan tested out the geometry on a synthetic slab in a half-space model. McMechan concluded that in order to resolve the slowness of a region in space, independent sampling of that region by many rays is required. Rogers et al. (1987) used the same method for delineation of a coal seam but they concluded that the resolution of the slowness in a region does not depend only on the number of rays but the angular range of coverage. A similar conclusion on ray density and angular coverage is drawn by other authors (Kanli et al., 2008 and Leblanc et al., 2004), with Leblanc et al (2004). further suggesting that the slowness resolution is limited in the directions parallel to the ray paths.

With the knowledge gained from previous work done, this study examined an application of surface-to-borehole travel-time tomography in mining exploration. This thesis contains some background information on tomography in Chapter 2. The same chapter also describes the methods of synthetic data generation, picking the travel-times and inverting the travel-time data. Chapter 3 contains inversion results of each model produced, along with preliminary observations and discussions of the results. Chapter 4 is dedicated to presenting the results from data collected at the Reid Brook area of the Voisey's Bay mine site in Labrador. Chapter 5 contains an extended discussion of the results obtained from the models and field data inversion. Final conclusions and recommendations on how to improve this study are suggested in Chapter 6.

Chapter 2 : Research theory and methodology

2.0: Introduction

Surface-to-borehole travel-time tomography has been a relatively unused tool for exploration in the mining industry. Some of the potential advantages of using this geometry include: the opportunity to scan several hundred meters away from the borehole; the possibility of scanning around the borehole, thereby increasing the chances of characterizing the geology around the borehole. Also, with a peak frequency range of 50-100Hz (Wardell, 1970) used in land seismology, there is also a possibility to image geology at depths >500 m. Potential uses, such as those listed, make an investigation into the capabilities of this geometry important.

The evaluation of surface-to-borehole travel-time tomography was done using a series of carefully selected synthetic models. These models were designed and forward modeled to generate synthetic seismograms; then, the first-arrival travel-times from the seismic shot records generated were picked and assigned source-receiver coordinates accordingly. Following this, the travel-time data picked were inverted using the minimum-structure inversion method.

As a background for the modeling experiments, this chapter describes the velocity contrast required between rocks for travel-time tomography to be successfully applied. Following the physical properties discussion, I discuss the forward modeling technique that provides the data for the tomography throughout this study. A summary on the theory of travel-time inversion and minimum-structure inversion is given in this chapter, followed by a description of the inversion steps used to carry-out the data inversion during this study.

2.1: Physical Properties Discussion

All geophysical methods require a variation in the rock properties of the target rock and the host rock in order for the methods to work successfully. Reflection seismology, for instance, requires an acoustic impedance contrast to be on the order of 6% (Salisbury and Snyder, 2007) in order to record a detectable reflection; gravity methods require a density contrast between adjacent rocks in order to be able to distinguish the rocks. In the case of seismic travel-time tomography, a velocity contrast between the rocks is required, making it important to have an understanding of the velocity contrasts between target rocks and host rocks. Chen et al. (2006) used first-break travel-times and a curved-ray tracing algorithm to study the effect of velocity contrasts on inversion results. They discovered that a high velocity contrast (>30%) produced tomographic results that were deformed when compared to the true model, while a moderate contrast (15%-30%) produced acceptable results and low contrasts (<15%) produced good tomography results. They attributed the cause of the deformed results to uneven ray coverage caused by high velocity contrasts between neighboring geological bodies.

The Nafe-Drake curve (figure 2.1) illustrates the P-wave velocity and density relationship of common rocks from compiled laboratory measurements. The curve demonstrates that the velocity of silicate rocks generally increases with density and that both velocity and density increase as composition shifts from felsic to mafic. Sulfide rocks lie to the far right of the Nafe-Drake curve silicate trend and although their velocities are comparable to the silicates, their densities are generally significantly higher. In addition, the velocity and density of sulfide rocks vary considerably depending on their mineralogy.

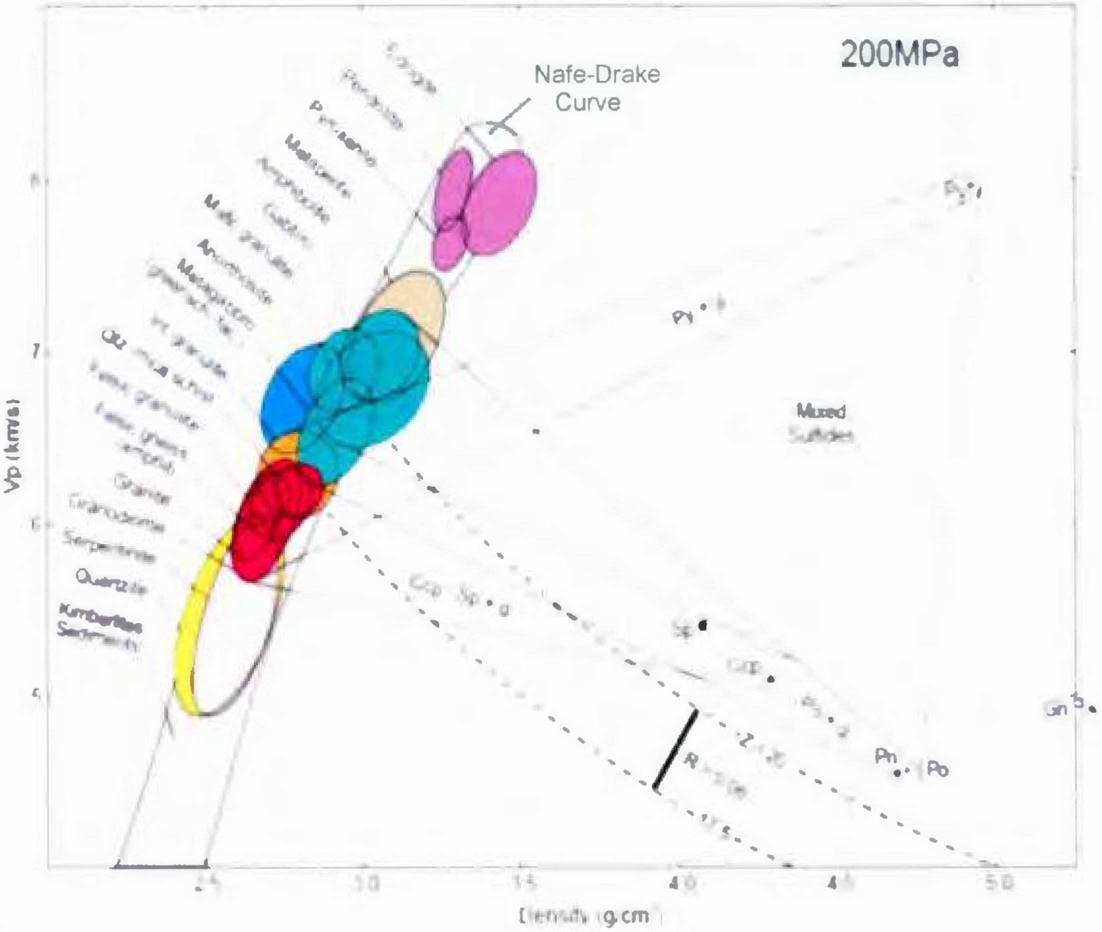

Figure 2.1: Lines of constant acoustic impedance (Z) superimposed on velocity-density fields and Nafe-Drake curve (grey) for common hardrocks at a standard confining pressure of 200 MPa. Also shown are values for pyrite (Py), pentlandite (Pn), pyrrhotite (Po), chalcopyrite(Ccp), sphalerite (Sp), gangue (g), galena (Gn). (Courtesy of Salisbury and Snyder, 2007)

Depending on the rocks that host a sulfide deposit and the mineral composition of the deposits, it is possible to have high to no velocity variation between the ore and host rock. For example, a sulfide that is rich in pyrite will have a high p-wave velocity of approximately 7.0km/s. If this type of pyrite-rich sulfide is hosted in a mafic/ultra-mafic rock such as a gabbro (~7.0km/s), there will be no velocity variation. When the same pyrite-rich sulfide is hosted in a felsic rock such as granite (~6.0km/s), then a velocity variation of approximately 17% exists between the ore body and host rock. On the other hand, a pentlandite-rich sulfide (~5.0km/s) will have a good velocity contrast (17%) in a felsic host (~6.0km/s) and a high contrast (37%) in an ultra-mafic (8.0km/s) host rock.

A velocity contrast between ore and host rocks is known to exist in mines around Canada and around the world (Goulty, 1993). As an example, in the Reid Brook area of the Voisey's Bay deposits, the massive sulfides are hosted by para-gneiss. The massive sulfides have an average velocity of 4.7 +/- 0.328 km/s and the gneisses have an average velocity of 5.6 +/- 0.279 km/s (Duff, 2007). The velocity contrast (16%) between the sulfides and para-gneiss suggests that tomography is a suitable tool to use for imaging in the Reid Brook area. Another example is the exploration of the Tsumeb and Kombak ore deposits in Namibia. A significant target horizon in the mine area is the Otavi/Mulden contact, and from physical properties measurements done in the area, the Otavi group have an average P-wave velocity of 5.1km/s and the Mulden group have an average velocity of 3.4km/s (Stevenson et al., 2003). The 33% velocity contrast between the two rocks that make up the contact in this region makes tomography a suitable tool for exploration in that area as well.

For the purposes of this study, velocity data and geometric examples from the Voisey's Bay massive sulfide deposit and from the Sossego copper deposit (in Brazil) will be used. The Voisey's Bay and Sossego deposits provide a range of velocity contrasts (5%-33%) and a range of geometries that make them suitable for use in assessing the capabilities of the surface-to-borehole tomography method.

2.2 Seismic Forward modeling

Geophysical forward modeling involves computing the geophysical response of a model which one is trying to study or understand. Forward modeling in this study involves generating seismic data that is used for tomographic inversions. Synthetic seismic data was generated in Seismic Unix using a 2nd order acoustic finite-difference algorithm. In the finite-difference approach, the two-dimensional partial differential wave equations that describe the propagation of seismic waves in an acoustic medium are approximated by suitable finite-difference equations. These equations are solved on a discrete spatial grid by numerical procedures. The system uses a time-marching procedure that solves the wave equation recursively in time for the motion in a medium (Kelly et al., 1976). The finite-difference program uses a source signal that generates a perfect pulse with no multiples or losses due to transmission or attenuation intrinsic to encountered layers (Mari and Coppens, 2003).

To prepare a model for finite difference calculations, there are several steps and factors that have to be followed and taken into account. First, a geological model is built in which the rock units of interest are assigned grayscale tones according to the slowness values that are to be assigned to each body. For the stability condition of the finite-difference method to be sufficiently satisfied, the models require at least 10 grid nodes per wavelength (Levander, 1988). The limiting wavelength is calculated by dividing the smallest P-wave velocity by the largest source signal frequency to establish the shortest wavelength. The geologic model is then exported into a UNIX environment as a bitmap (PCX) with pixel spacing that satisfies the stability criteria. In UNIX, the bitmap file is converted to ASCII and slowness values are assigned to the various grayscale tones in the image. The new file with slowness values assigned is converted to binary and used as an input file in the finite-difference calculator (Refer to appendix C for forward modeling procedure and input files).

In the finite-difference input file, parameters such as the grid spacing and peak frequency are specified; the total number of shots to be taken is specified, the x and z location of the first shot is specified and the shot spacing distance is specified as well as the z-location of the receiver borehole. To deal with the possibility of reflections from the outer boundaries of the model, the boundary conditions applied to the model was such that the outer walls acted as an absorbing media and therefore eliminated any side reflections from the walls of the model. After assigning of all required parameters, the finite difference program is run to generate seismograms which are written out as SEG-Y files. The SEG-Y file format is the acceptable input format for Landmark Graphics ProMAX software, which is used to do the data processing and travel-time picking.

2.3 Data Processing and Picking First-Arrival Travel-times

Each seismic dataset was imported into ProMAX for processing and picking travel-times. Processing steps done to prepare the data for picking included assigning each shot and receiver x and z coordinates in 2-dimensional space. The travel-times picked, along with associated source and receiver coordinates, are used to generate the tomograms. Therefore, it was important to ensure that the proper geometry information was assigned to each travel-time because, as described later, the distance between shot-receiver offsets are integral components of travel-time inversion. Figure 2.2 shows a selected model example with select shot points included. The corresponding seismograms, assigned shot/receiver locations and first-arrival travel-time picks (red) for the shot points can be seen in figures 2.3, 2.4 and 2.5.

After travel-times have been picked as accurately as possible (+/- 1ms), they are written out as an ASCII file. The travel-time file written out consisted of several columns, the first column contained the trace number or index number, and the next 6 columns contained information about the x, y and z coordinates of the shot and receiver location for each trace. The last column contained the travel-time picked for each trace. This file format was the accepted file format for the inversion programs provided by Dr. Peter Lelièvre.

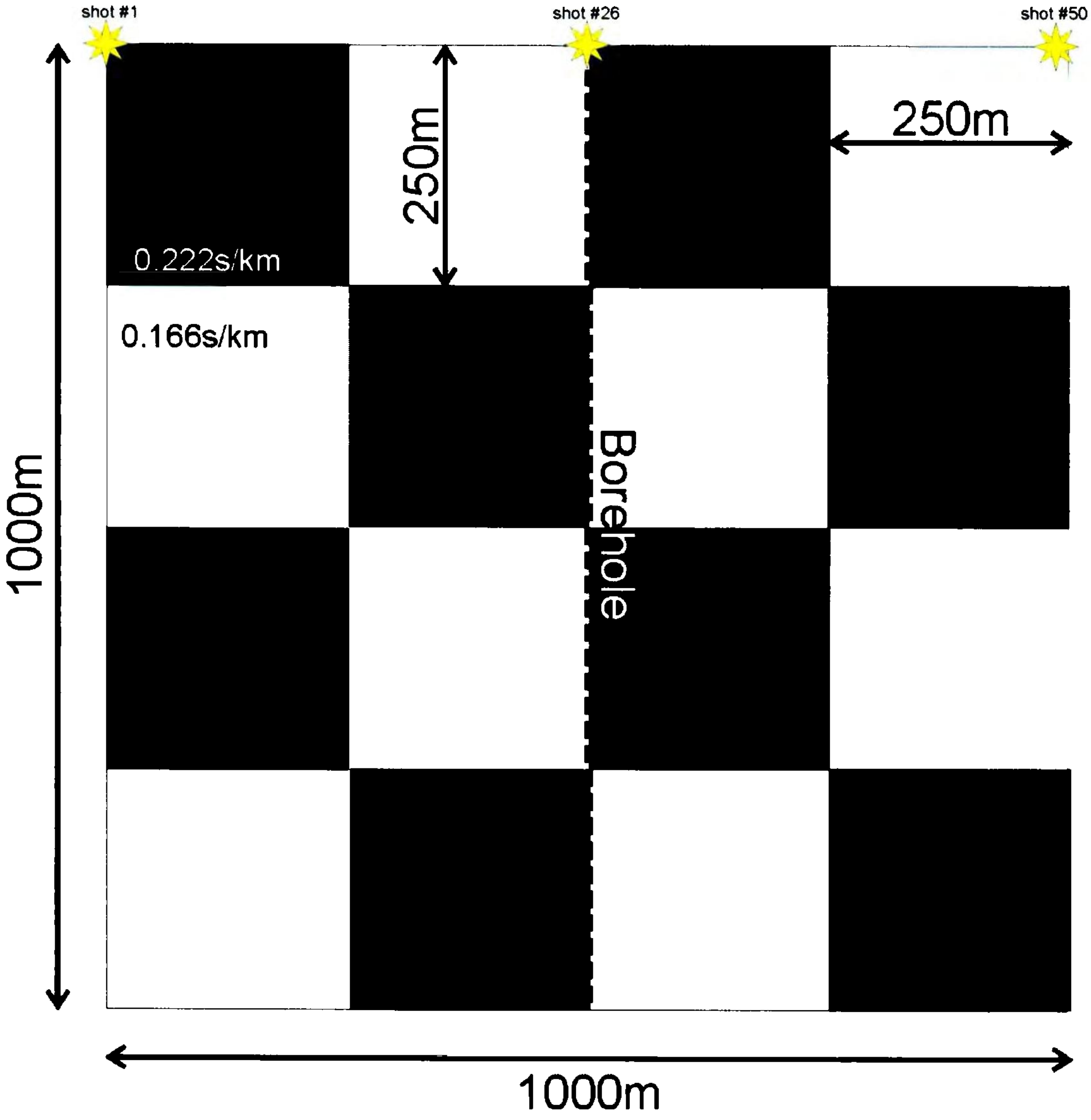

Figure 2.2: A model example showing shot points 1, 26 and 50. The resulting seismogram from forward-modeling this model and the corresponding first-arrival picks can be seen in figure 2.3, 2.4 and 2.5, respectively.

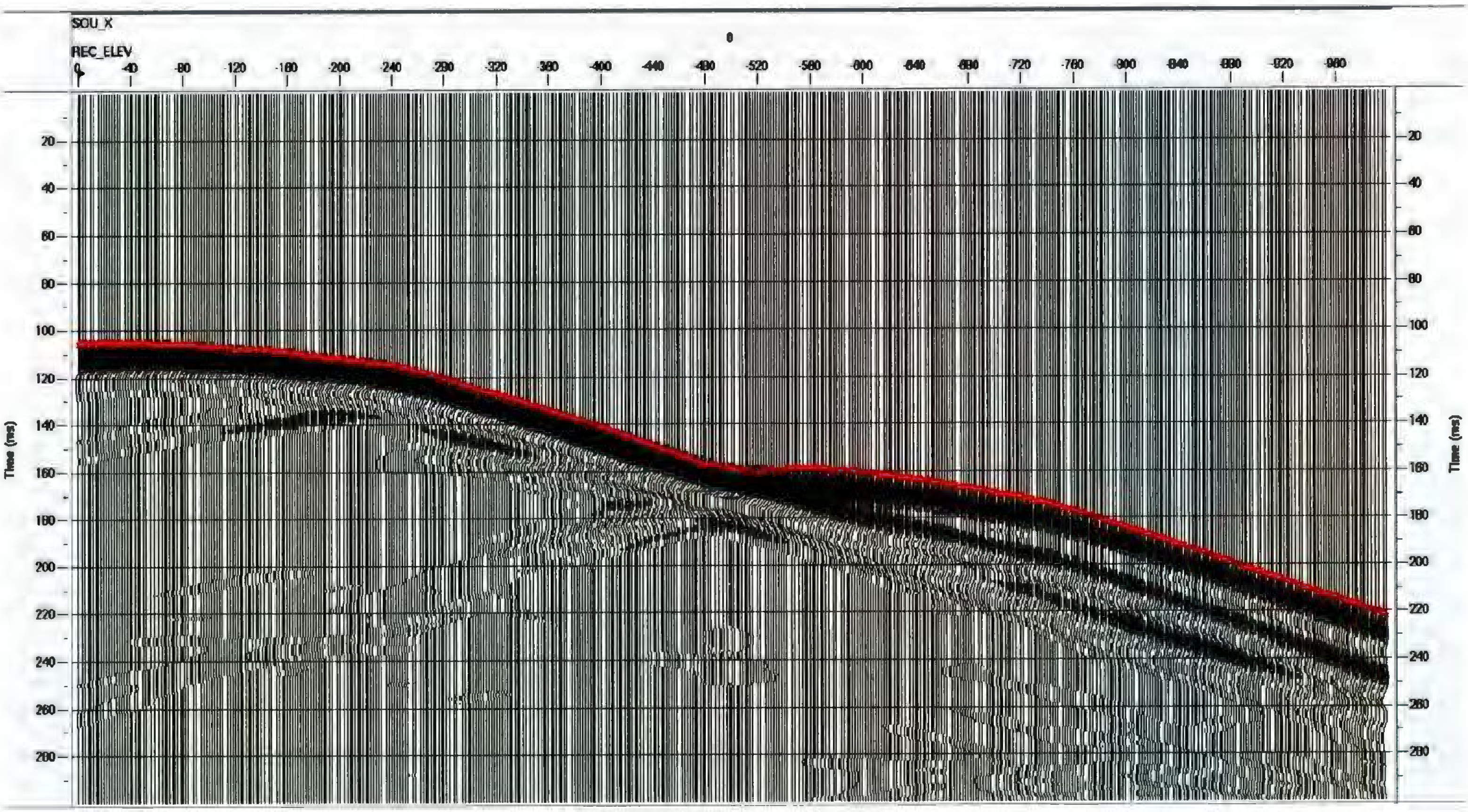

Figure 2.3: Shot record showing first arrival travel-time picks (red) for model, shot number 1.

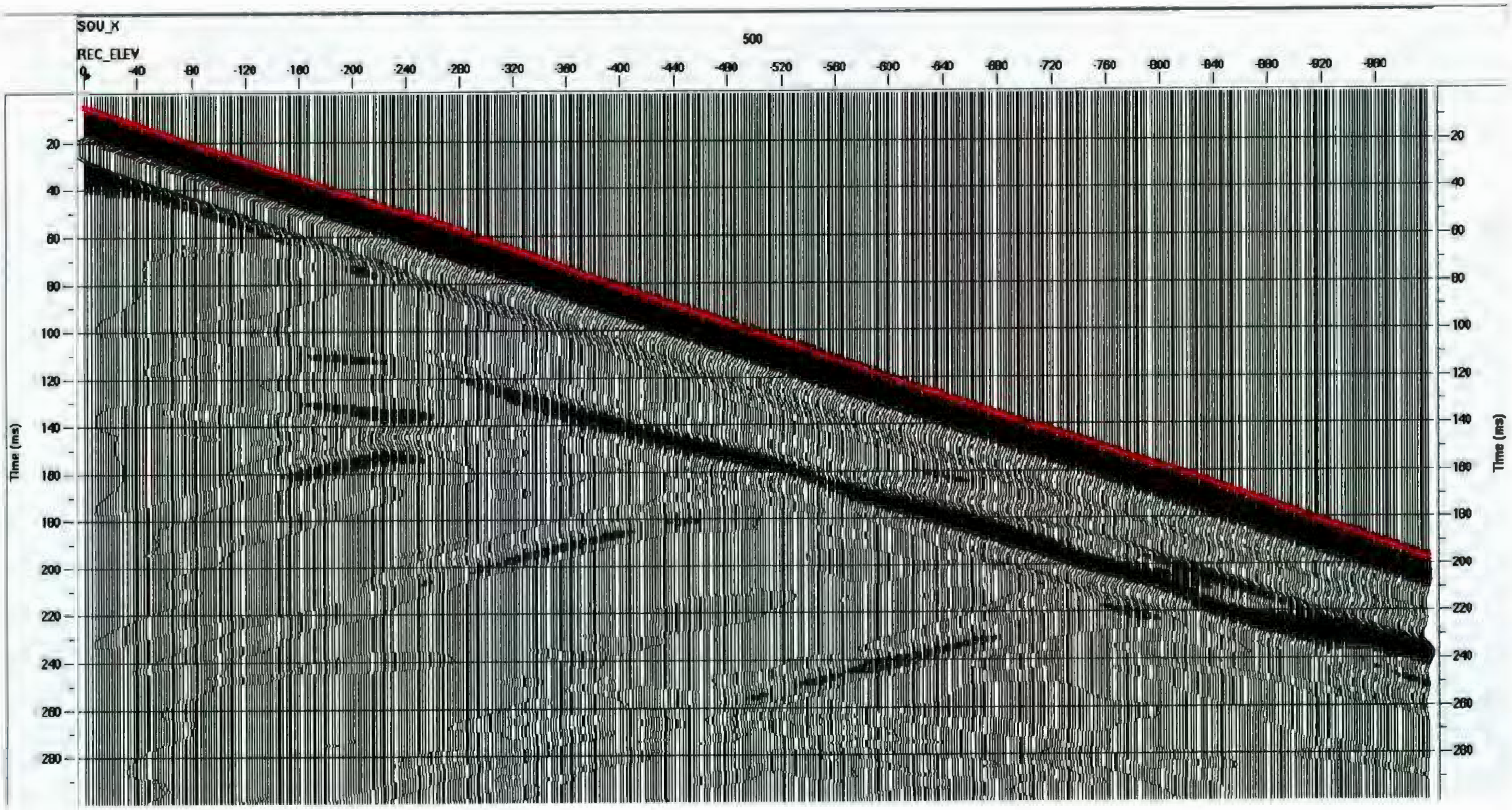

Figure 2.4: Shot record showing first arrival travel-time picks (red) for model, shot number 26.

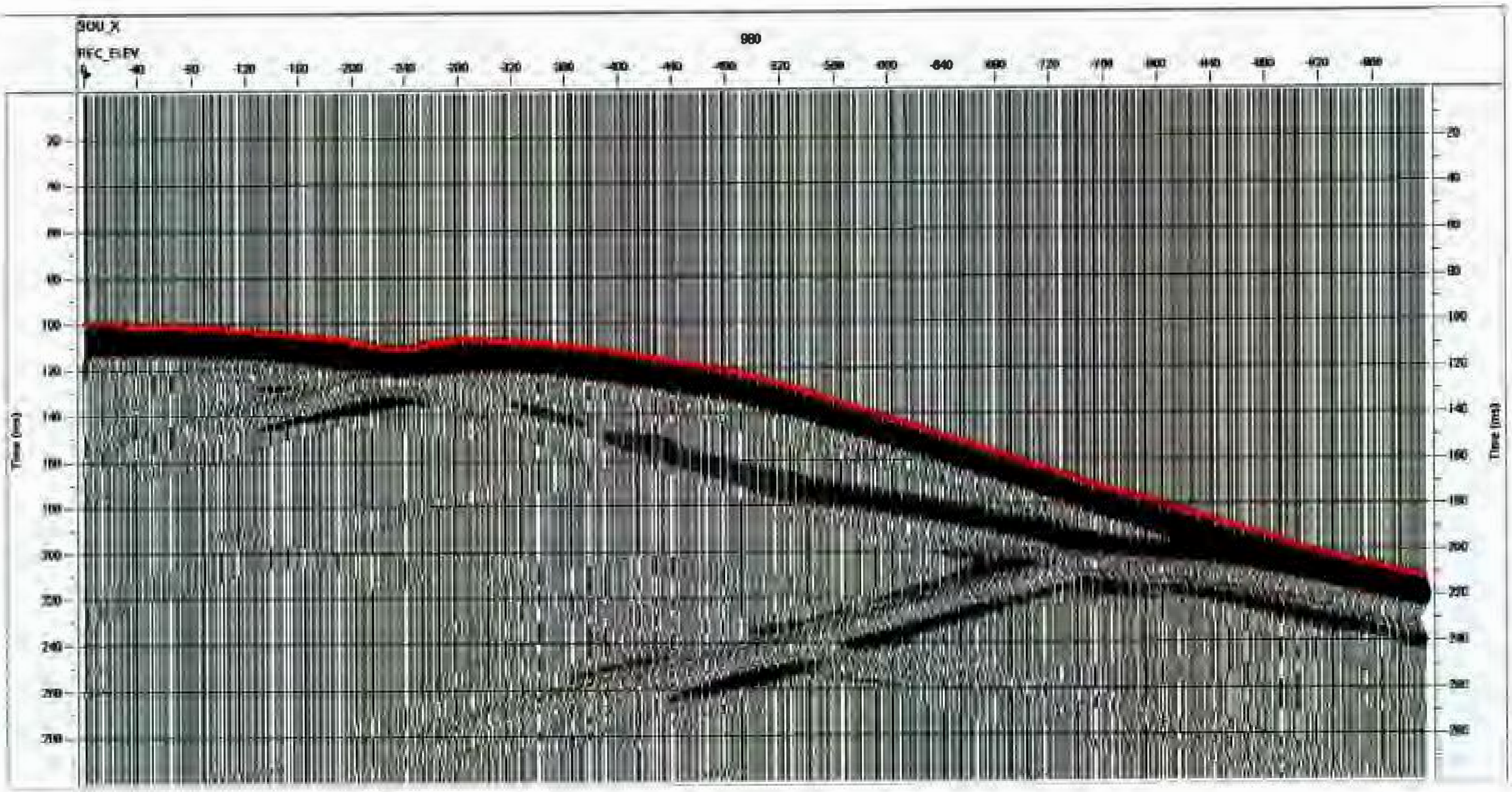

Figure 2.5: Shot record showing first arrival travel-time picks (red) for model, shot number 50.

2.4 Seismic Travel-time Tomography

Seismic travel-time tomography is a technique used to obtain an image of the subsurface by estimating the subsurface velocity distribution from the source to receiver travel-times. The travel-times can be derived from a number of different survey geometries such as the surface-to-borehole, cross-well and surface seismic reflections (Li et al., 2005). The travel-time measured is a line integral of the velocity of the individual rock units the ray passes through. To solve for each rock unit velocity, the subsurface is divided into square or triangular cells of a certain dimension in which rock properties of that medium are assumed to be constant in a cell.

In a simplified schematic of a subsurface discretized into square cells, the travel-time of a ray segment traveling through a particular cell is described as a function of the velocity of the cell and the length of the ray segment. Assuming straight-ray approximation, figure 2.6 shows 9 discrete square elements in which each of the elements has a constant slowness (inverse of velocity) value. Consider ray AB, whose parts consist of 3 segments each with distance x_3 in slowness s_7, x_2 in slowness s_4 and x_1 in slowness s_1. The total travel time TAB for ray AB is

$$TAB = x_3 s_7 + x_2 s_4 + x_1 s_1 \qquad (1)$$

A set of ray equations like the equation (1) above can be represented in matrix form as Xs = T, where X is an NxM matrix of distance elements; M is the total number of slowness elements in the subsurface; N is the total number of rays; s is the slowness vector (length M) and T is the travel times (length N). For the 3 rays in figure 6, Xs = T in matrix form is written as:

$$\begin{bmatrix} x_1 & 0 & 0 & x_2 & 0 & 0 & x_3 & 0 & 0 \\ 0 & x_4 & 0 & x_5 & 0 & 0 & x_6 & 0 & 0 \\ 0 & x_8 & x_7 & x_{10} & x_9 & 0 & x_{11} & 0 & 0 \end{bmatrix} \times$$

$$[s_1 \quad s_2 \quad s_3 \quad s_4 \quad s_5 \quad s_6 \quad s_7 \quad s_8 \quad s_9]^{Tr} = [TAB \quad TAC \quad TAD]^{Tr} \tag{2}$$

where superscript Tr denotes transpose (McMechan, 1983). In performing the inverse computation (assuming straight-ray approximation), X is known, values for travel-times T are observed and values for s are computed. If a curve-ray method is used, then the matrix X is unknown because it not known beforehand what directions the rays will travel. Also, if a non-ray based approach is used, then the length of rays in a cell is not required. For instance, the fast marching approach used in this thesis calculates first arrival travel-times through propagation of wave fronts rather than rays. Lelièvre et al. (2011a and b) contains a detailed discussion of the fast marching approach and more details about the method can be found there.

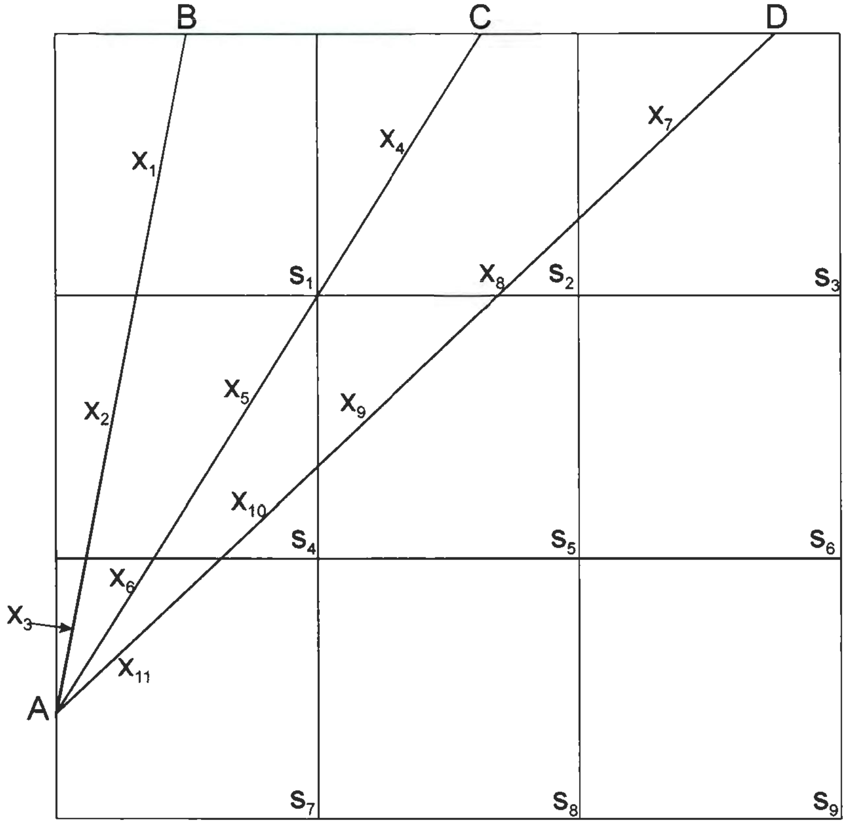

Figure 2.6: Subsurface area to be imaged discretized into square elements (Modified from McMechan, 1983).

Overall, the tomography concept discussed above is the general approach to solve for velocity distribution in the subsurface. However, the inversion algorithm that can be used to solve the computation above can vary and the choice of inversion procedure used in this thesis is the sum-of-squares minimum-structure inversion method. Although this approach spreads out changes in cell properties gradually (rather than having sharp boundaries) over a number of adjacent cells, thereby producing a smeared-out image of the subsurface, it is a method that is reliable, robust and produces models with enough features to reproduce the observations while limiting the number of artefacts due to noise in observations. The minimum-structure method also allows the user to include constraints (velocity and/or structural) into the inversion with the hope of achieving a better inversion result (Farquharson, 2008).

2.5 Minimum-Structure Inversion

In the minimum-structure inversion method, the subsurface is first discretized into a (rectilinear or triangular) mesh. The rock property (velocity/slowness) in each cell is uniform throughout the cell but can change over the course of the inversion. An initial velocity/slowness value is input into the mesh and forward modeled to obtain a predicted travel-time dataset. This predicted dataset is then compared to the observed dataset to see how adequately it fits a specified measure of misfit. If the measure of misfit is not attained, the inversion adjusts the velocity distribution in the mesh until the predicted data and observed data match within the specified measure of uncertainty and the objective function is minimized (Mosher, 2009). The objective function is a measure of how well the observations are reproduced (data misfit) and of the model complexity (Farquharson, 2008).

The objective function which minimum-structure inversion tries to minimize is:

$$\Phi = \Phi_d + \beta\Phi_m. \tag{3}$$

The data misfit term ϕ_d has the general form:

$$\phi_d = \sum_{i=1}^{N}\left(\frac{F[\mathbf{m}]_i - d_i}{\sigma_i}\right)^2, \tag{4}$$

The data misfit measures the difference between measured data, $d_{i,}$ and the data generated from the inversion, F[m], where F stands for the forward modeling operator and the model vector, m, contains the physical property values in each cell. The data difference is normalized by the estimated uncertainties, σ_i, which helps to specify how well particular data values should be fit relative to others (Lelièvre et al., 2012).

The regularization term, ϕ_m, is the measure of the amount of structure in the model and it has the form

$$\phi_m = \alpha_s||\mathbf{W}_s(\mathbf{m} - \mathbf{m}_{ref})||^2 + \alpha_m||\mathbf{W}_m\mathbf{m}||^2, \tag{5}$$

The first term controls the closeness of the recovered model, **m**, to the reference model $\boldsymbol{m}_{ref}$, and $\mathbf{W}_s$ contains the square-root of cell volumes along its diagonal. The second term encourages smoothness in the recovered model where $\mathbf{W}_m$ calculates model differences between the cells. α_s and α_m are constants, while β is a trade-off parameter (Lelièvre et al., 2011b).

In minimizing the objective function (equation 3), an appropriate value for the constant β that will provide a model which fits the observed data, to a desired degree, and contains some acceptable structural features is sought. A trade-off exists when trying to select a value for β because decreasing the value for β creates models that fit the data better but contain more structure. If the β value is too low it can lead to noise being fit into the data and this can produce artefacts and random structures to be included in the recovered model (Lelièvre et al., 2012).

The approach used for determining a suitable β value in this study was to specify a target misfit (chifact) and search for a value of β that provides a misfit value close to the specified target after the objective function is minimized. In searching for an appropriate value of β, the inversion starts with a large value of β then performs a few model perturbations; it then reduces the specified β value, then performs more model perturbations, repeating the same steps until the specified target misfit is reached and the objective function has been minimized. An appropriate target misfit value should be a number close to the number of data, N (Lelièvre et al., 2012).

2.6 Inversion Procedure

This section describes procedures used to generate the tomograms from the picked travel-times (Refer to appendix D for more detailed inverse procedure and input files). An itemized list of the steps followed by a discussion of each step is as follows:

- Create inversion grid
- Decimate data file (optional)
- Split data file into source file, receiver file and travel-times file
- Create forward solver file
- Create inversion file

Creating Inversion Grid

A crude measure of the resolution of a tomogram is determined by the ray density of the cells in a particular grid. The ray density is defined as the number of rays passing through a cell in a discretized subsurface. Cells that have a higher number of rays passing through them are more likely to be better resolved, making a coarser cell size appear to be a better choice. However, the size of objects that can be imaged is dictated by the size of the mesh cells, as smaller cell sizes can resolve smaller objects. Therefore, there is a trade-off between resolution based on ray density and resolution based on the size of the object that can be imaged.

In this project, most of the inversions were performed using structured rectilinear meshes and other inversions were performed using unstructured triangular meshes. For the rectilinear mesh, a cell size of 20m by 20m was used for the inversions done in this thesis.

Decimating Data

The speed of the inversion depends on the number of travel-times used in the inversion; hence, the fewer the number of traces used the faster the inversion runs. Several tests were done to determine if decimating data resulted in poorer results for the inversion. Results showed that decimating the data by a factor of two generally had the same result as using the full dataset. Therefore, all of the data used for this thesis were decimated to make the inversions run faster.

Splitting the Data File

The travel-time data file consists of travel-time values with their corresponding source and receiver coordinates. Splitting the data file into a source location file, receiver location file and travel-times file was a pre-requisite for creating the forward solver and inversion files. These new files were used as an input for the forward solver and inversion files.

Creating Forward Solver File

The forward solver file is an input file that specifies all the parameters that the inversion will use for forward modeling the data. In this file, the inversion mesh used was specified; the sources and receiver files were specified as well as the travel-time information file. The type of trace mode used for forward modeling the data can be a choice of ray tracing methods such as the straight ray method or a non-ray tracing method such as fast marching.

When ray-tracing methods are used to perform inversions, the results generated typically exhibit ray-like artefacts that have locations and directions connected to the ray traces. However, the fast marching approach, which is a non-ray tracing method, reduces the presence of such artefacts in the result considerably without reducing the resolution of the inversion (Lelièvre et al., 2011b). The fast marching approach was the preferred choice of trace mode used for this thesis because an improved interpretation of the results can be achieved with a reduction of artefacts.

Creating Inversion File

The forward modeling file is one of many input parameters required for creating the inversion file. The forward modeling file contains the travel-time data that will be used during the inversion. The Versatile INVersion (VINV) program provided by Dr. Peter Lelièvre is the program that was used for all the inversions in this project. The VINV program enables users to be flexible with inversion parameters to achieve better results by being able to set parameters such as slowness bounds or by being able to change the normalized target misfit of the result. If prior information about the data being inverted is known, it can be included into the inversion as a reference model that contains structural and physical properties that help constrain the result of the inversion.

Chapter 3 : Results

3.0: Introduction

The surface-to-borehole travel-time tomography method has been a relatively unused method in mineral exploration despite some of the potential advantages offered by this configuration. This thesis assesses the capabilities of travel-time tomography using surface-to-borehole orientation. To gain an initial understanding of the capabilities of surface-to-borehole tomography, some non-geological models and several checkerboard pattern models are designed, forward modeled and inverted. The results of these models provide an initial evaluation of the capabilities of the geometry for tomography. After the checkerboard tests, some geological models are used to perform a further assessments on the inversion geometry.

In evaluating the model results, the accuracy of the results is determined based on: how well the inversion reproduces the slowness structures in the subsurface; and how well the inversion reproduces the observed travel-time data used to perform the inversion. Evaluation of how accurately the slowness structures in the subsurface are reproduced is done by comparing the tomograms to the known geological models; while evaluation of how accurately the observed travel-times are reproduced is done by analysing the normalized residual travel-time plots of the models. The residual travel-time is the difference between the predicted travel-times and the observed travel-times, while the normalized residual travel-time is simply the residual travel-time divided by the value of the standard deviation used for the inversion. A combination of the tomogram and the residual travel-times plot forms the basis of analysing inversion results in this chapter.

In tomograms, resolution of the slowness in a region depends on the number of rays and range of angles at which the rays pass through the region (Rogers et al., 1987). Therefore, the areas in the subsurface with the best chance of resolution are the regions that are sampled by as many rays and at as many angles as possible. Assuming straight ray coverage in a uniform velocity subsurface, figure 3.1 shows a ray density (number of rays per cell) plot of a 20 units wide by 20 units deep subsurface. The plot uses 40 surface sources and 40 borehole receivers, both spaced at 0.5 units, while the grid is divided into 400 square cells that are 1 square-unit each. Based on the straight ray density plot, the areas with the best chance of resolution are the areas closest to the borehole and the surface, while the areas with no ray coverage lie beyond the straight ray joining the last receiver to the first and last shots. Areas with no ray coverage cannot be resolved in the subsurface since there is no information about those regions in the data. By using the straight ray, uniform velocity subsurface diagram as a guide, the interpretation of the tomograms will be limited only to regions with ray coverage. However, if a velocity variation exists in the subsurface, the ray coverage region will vary and can include more or less area than the straight ray approximation, depending on the size of the variation and whether the ray goes from a fast velocity to slow velocity and vice versa.

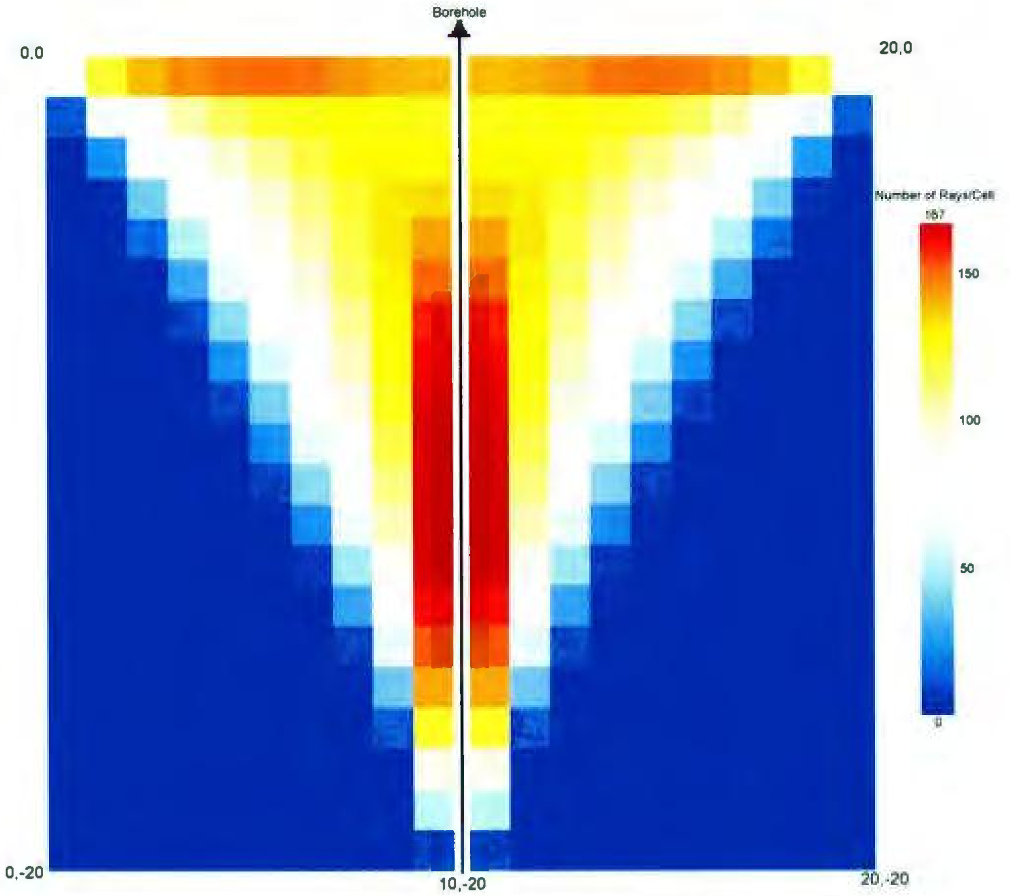

Figure 3.1: Ray density plot of 40 equally spaced surface sources and 40 equally spaced borehole receivers in a 20unit wide by 20unit deep subsurface area. Subsurface cells are discretized into 1x1 unit cells. (Code Modified from Deng)

In the regions with ray coverage, the influence which any velocity variation present has on the tomogram result will be analysed. As mentioned in chapter 2, for first arrival travel-time tomography, velocity contrasts greater than 30% between a host and ore produces highly deformed tomography results, velocity contrasts of 15% - 30% produce acceptable results and contrasts <15% produce good results (Chen et al., 2006). The presence of velocity variation causes refraction of incident waves at rock boundaries.

Figure 3.2 indicates the basic concept of Snell's law that dictates how incident waves respond when they interact with velocity variation boundaries.

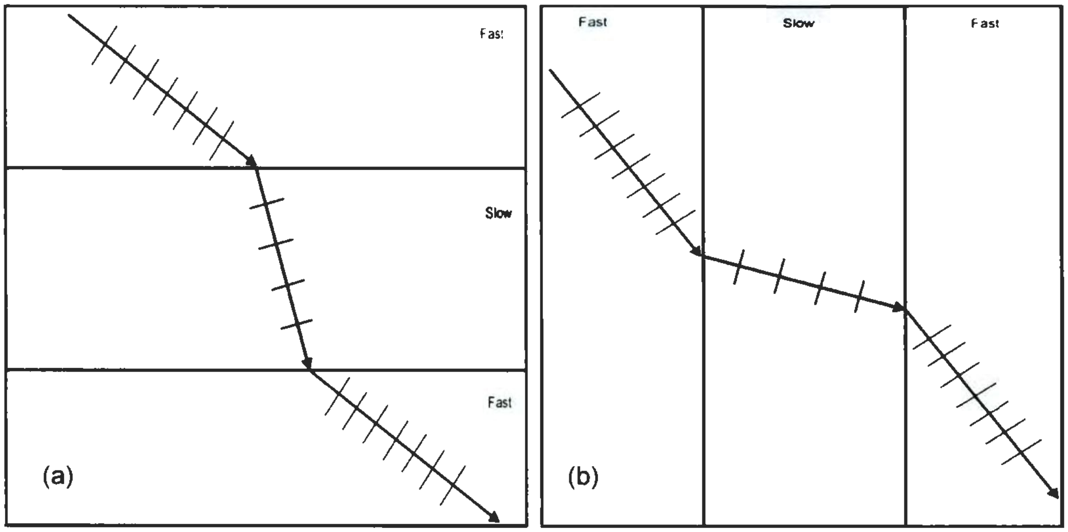

Figure 3.2: Refraction of incident rays from a fast body to a slow body and back to a fast body at (a) horizontal boundaries and (b) vertical boundaries (Modified from Reynolds, 1997).

Following the analysis of the tomograms, evaluation of the normalized residual travel-times for each model is carried out. As previously stated, the residual travel-time is the difference between the predicted travel-time and the observed travel-time. The predicted travel-time of a source-receiver pair is a function of the velocities in the tomogram and the path taken by the ray to go from the source to the receiver; while the observed travel-time of the same source-receiver pair is a function of the velocities of the known geological model and the path taken for the ray to go from the source to the receiver. A positive residual indicates that the predicted travel-time is higher than the observed travel-time for a particular source-receiver pair. Conversely, if the residual travel-time is negative then the predicted travel-time is smaller than the observed travel-time.

The differences between predicted and observed travel-times can be attributed to a variety of factors such as a difference in velocity distribution between the tomogram and the true model; variations in raypaths between the tomogram and the true model; or the difference in the forward modeling and inversion code method of calculating travel-times. One or more of these factors cause residuals to be positive or negative. Due to the difficulty in figuring out the exact ray paths or velocities used in calculating predicted travel-times, interpretation of the residuals in the plots will focus less on individual residual times and more on trends of a group of travel-times. An ideal residual travel-time plot should have randomly distributed signs and values of residual travel-times on the plot, but if a trend of negative or positive residual travel-time exists on the plot then the cause of the anomaly is discussed.

3.1: Non-Geological Model Examples

Resolution in travel-time tomography is a function of the acquisition geometry, the source frequency, angular coverage, size of velocity contrast, and the inversion grids. Based on these variables, the goal of this section is to develop an understanding of the resolution that can be accomplished using the surface-to-borehole tomography technique. To achieve this goal, a series of synthetic models is used. The first series of models is a subsurface represented by 2 homogenous rock units with different slowness values juxtaposed side by side. The models are further broken down into checkerboard patterns, with the dimensions of the squares in each checkerboard progressively decreasing. The checkerboard design is a technique that has been used in the past to examine the resolution of a new technique (Leveque et al., 1993) and thus a similar approach was used here. Slowness values for the models created are selected to be consistent with typical values associated with massive sulphide ore bodies and their host rocks at the Voisey's Bay mine (Duff, 2007).

Following the creation of the seismic data, random noise taken from a Gaussian distribution was added to the first arrival travel-times that were picked. The travel-times with added noise were then used to perform the inversion. For comparison, the tomogram results for each model are presented with a super-imposed outline of the true model. The inversion residual travel-time plots and acquisition and inversion parameters for each model are also presented (Refer to appendix B for detailed forward and inverse parameters used).

3.1.1: Model 1

The first example, shown in figure 3.3, was developed to test the approximate depth resolvable in a constant slowness area based on the parameters used. As seen here, the slowness values for the two blocks present are 0.222s/km and 0.166s/km (Duff, 2007). The survey area is 1000m wide and 1000m deep. A 1000m borehole, located at x=500m, containing 499 receivers at 2m intervals was used for recording 50shots at 20m intervals. For each shot, a peak frequency of 50Hz (Wardell, 1970) was used for the acquisition. At 50Hz, the 0.222s/km and 0.166s/km rocks are sampled at a dominant wavelength of 90m and 120m respectively.

For the inversion process, random Gaussian noise with a mean of zero and a standard deviation of 2ms was added to the picked travel-times. To perform the inversion, the recorded travel-times for every shot were decimated by using every second travel-time. Despite using half of the travel-times, the resulting tomogram resembled the one generated for the case in which all travel-times were used. Therefore, preference was given to the decimated inversion because it was faster and achieved the same result an inversion performed with the full data.

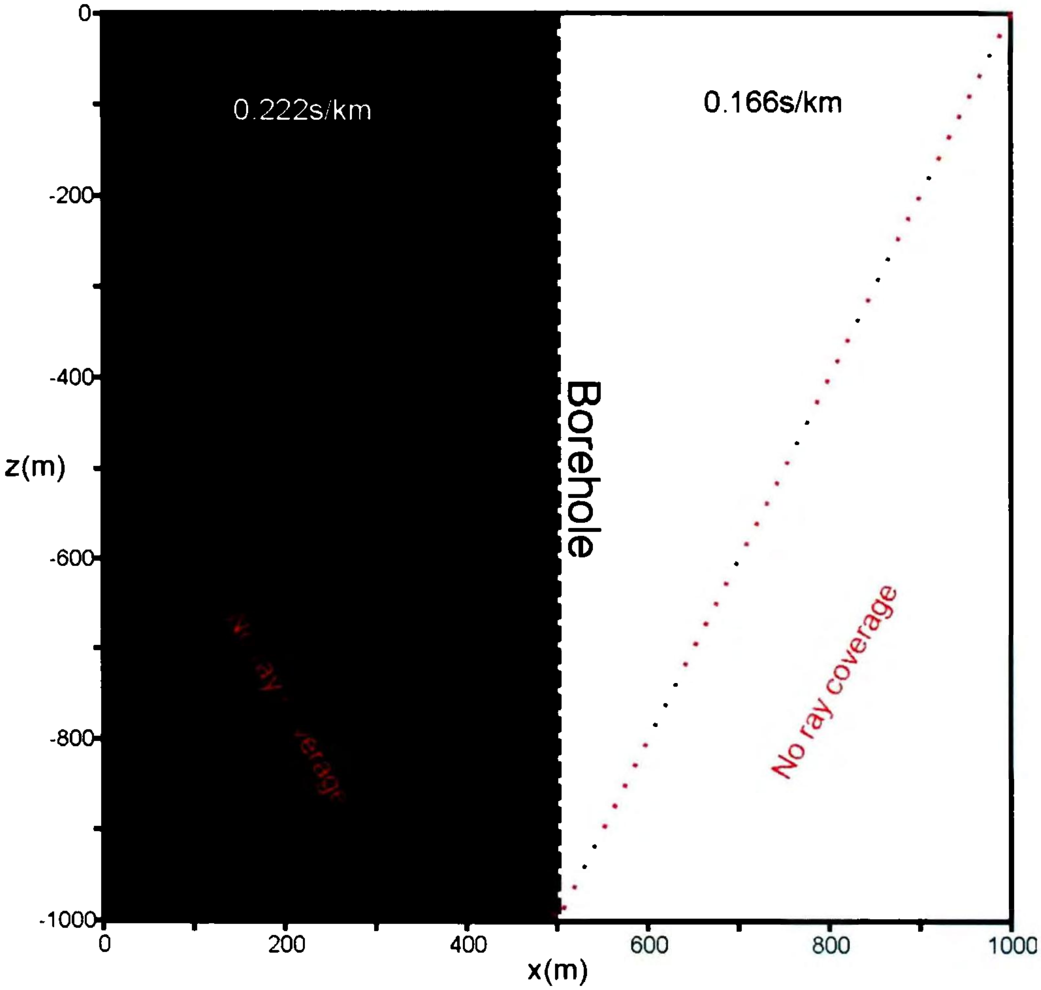

Figure 3.3: True model for model 1. The dotted red lines show the approximate limit of ray coverage.

The inversion result for model 1 is shown in figure 3.4. From this result, it was observed that the vertical boundary was well resolved and properly localized. In addition, the resolution of each rock unit was very good and well maintained up to a depth of 800m. Based on the survey grid and ray coverage in the model, the depth expected to be resolved in both slowness regions was approximately 800m because the rays travel through uniform regions and experience no refraction due to slowness contrast.

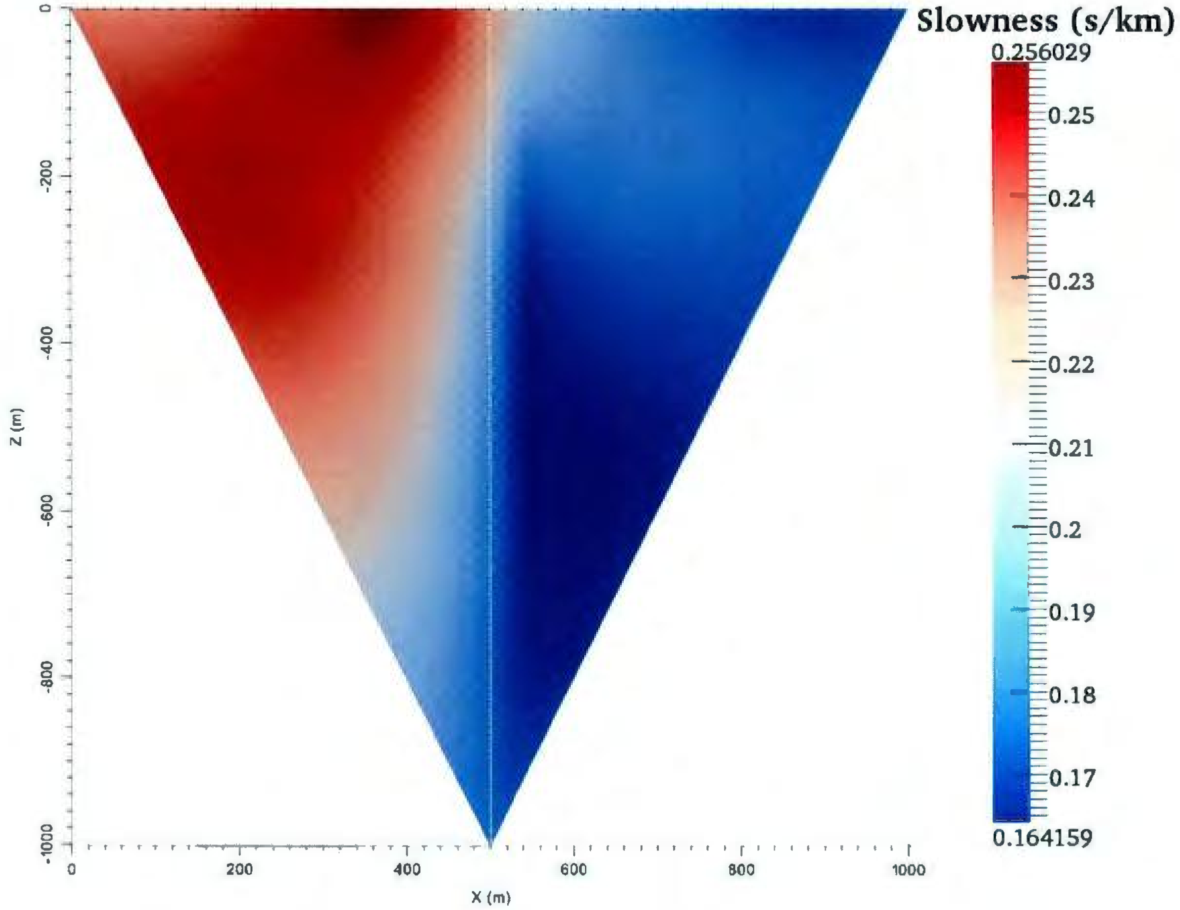

Figure 3.4: Inversion result for model 1. The vertical bar on the right shows the slowness scale for the tomogram.

The residual travel-time plot for model 1 is shown in figure 3.5a. In the residual plot, a pattern of high negative residual (circle 1) is observed for travel-times of sources close to the borehole and receivers close to the surface. The negative residual seen here indicates that the predicted travel-times are smaller than the observed travel-times. The discrepancy in travel-times is interpreted as the result of the different approaches to calculate travel-times at the receivers closest to the sources by the two forward solvers used (finite difference and fast-marching). In order to test this interpretation, the fast-marching method was used to provide forward model travel-times for model 1. The travel-times generated were then inverted and the predicted travel-times were also calculated with the fast-marching method. The residual travel-time plot generated when the fast-marching method was used to calculate both observed and predicted travel-times is shown in figure 3.5b. Comparison of figure 3.5a and 3.5b demonstrates that the residuals in figure 3.5b do not exhibit the same high negative residuals that are observed in figure 3.5a. Therefore, the anomaly, labeled 1, in figure 3.5a is likely as a result of the difference in travel-time calculation between the finite-difference forward modeling and fast-marching solver for receivers close to the source point.

In figure 3.5a, a region of high positive residual was also observed on the travel-times that have shot points close to the vertical interface between the two rock units. The high positive residual anomaly is caused by the smeared out interface generated in the tomogram by the minimum structure inversion. Due to the fuzzy boundary in the tomogram, the average slowness of the faster rock at the boundary (0.200s/km) is slower than it is in the true geologic model (0.166s/km), which causes the predicted travel-time to be higher than the observed travel-time.

Generally, for the example shown above, resolution is good for a depth range of 0m-800m. Also, the residual travel-times appear to be generally random, except in the regions near the interface and the region of near-offset source-receiver pairs.

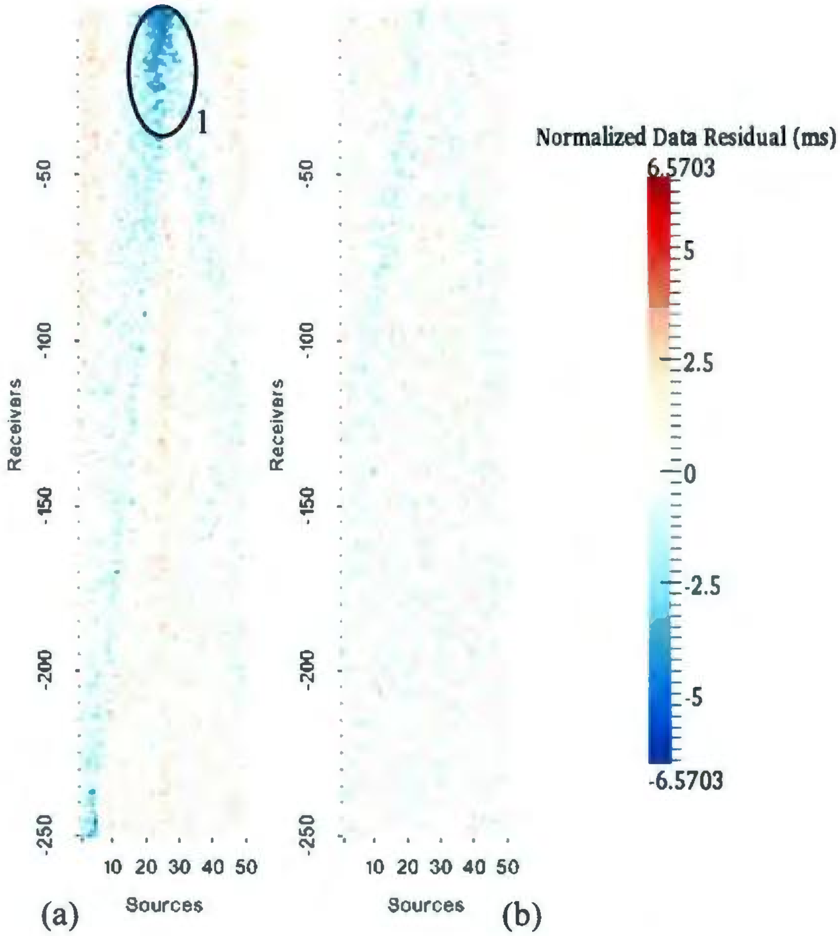

Figure 3.5: Normalized residual travel-time plot for model 1. (a) Residual travel-time plot for model 1 using finite-difference for forward modeling and fast-marching in inversion. (b) Residual travel-time plot for model 1 using fast-marching technique for forward modeling and inversion.

3.1.2: Model 2

For this example, shown in figure 3.6, the aim was to determine how accurately the inversion will locate the vertical boundary between the two rock units. As seen here, the two slowness values present in the model are 0.222s/km and 0.166s/km (Duff, 2007).The survey area is 1000m wide and deep while the 2 blocks in the model are 500m wide. 499 receivers at 2m intervals are placed in a 1000m deep borehole located at x=300m. 50 surface shots with a peak frequency of 50Hz (Wardell, 1970) were recorded at 20m intervals along the surface.

To perform the inversion, the recorded travel-times for every shot were decimated by using only every second travel-time. Thus, 250 travel-times per shot were used to perform the inversion. Random Gaussian noise with a mean of zero and a standard deviation of 2ms was added.

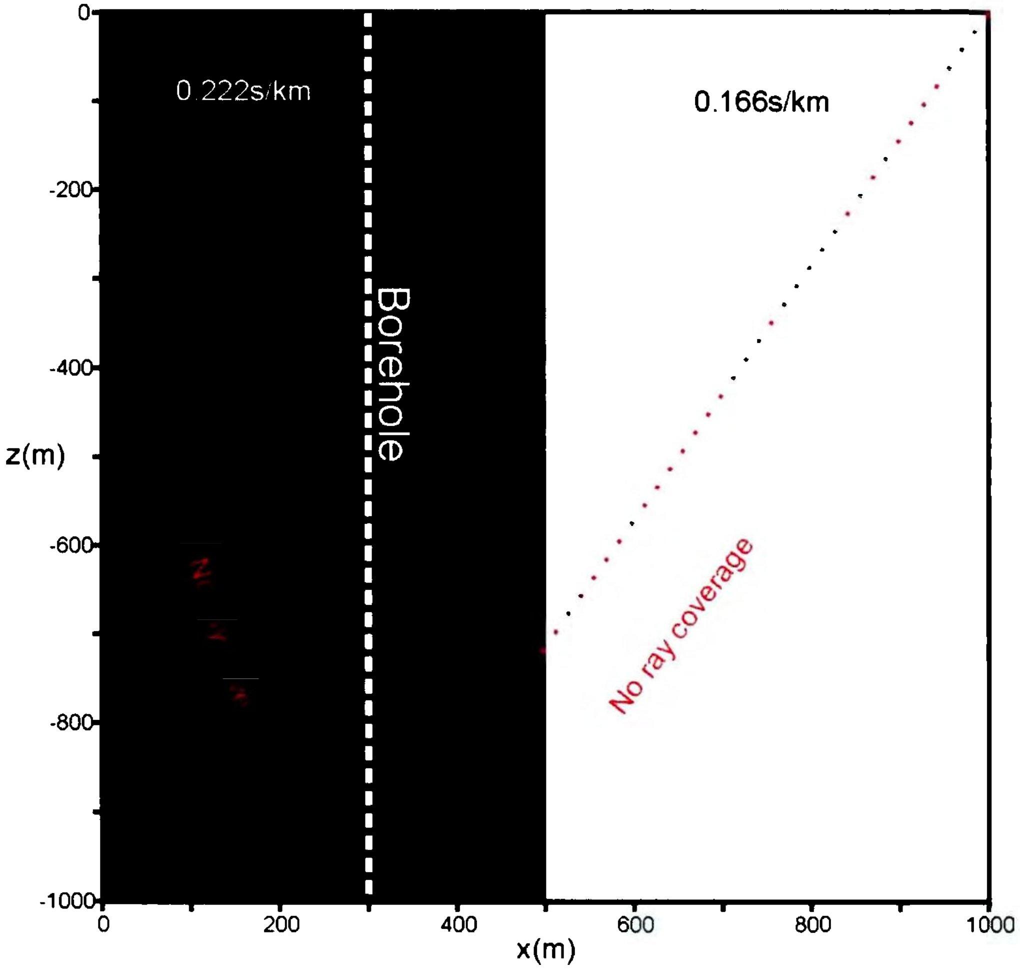

Figure 3.6: True model for model 2. The dotted red lines show the approximate limit of ray coverage.

The inversion result for model 2 is shown in figure 3.7. In the tomogram, it was observed that the vertical interface of the 2 rock units was well localized and resolved up to a depth of 400m. At depths greater than 400m, the vertical interface of the two rock units was skewed gradually towards the borehole in the direction in which the rays traveled. Deviation of the boundary at depths greater than 400m is likely because of the refraction of the rays at the boundary. Rays traveling from the medium with a lower slowness of 0.166s/km into the adjacent medium with a relatively higher slowness of 0.222s/km experience refraction, which causes the emerging rays to travel in a more horizontal direction than they were traveling prior to crossing the boundary. In addition, at depths greater than 400m the rays traveling in a near-vertical direction in the slower medium around the boundary are not being recorded in the borehole. These are the rays that could have provided the boundary with the horizontal constraints needed to resolve the boundary better at depth.

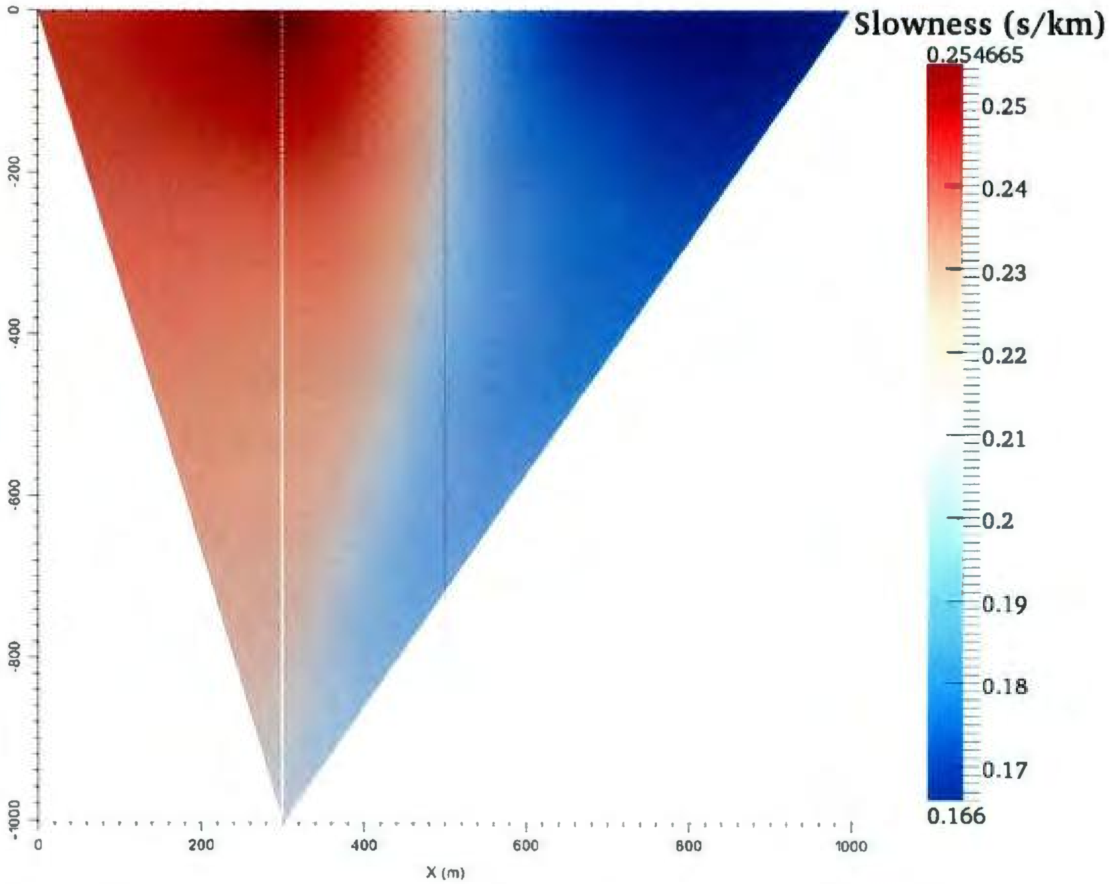

Figure 3.7: Inversion result for model 2. The vertical bar on the right shows the slowness scale for the tomogram.

Analysis of the results of this model includes analyzing the residual travel-times. However, the travel-time plot for model 2 does not contain any new trends that are different from the trends observed from the residuals of model 1. Therefore the residual for model 2 is located in the appendix A.

Overall, despite the 33% slowness contrast at the boundary of model 2, the vertical boundary was resolved up to a depth of about 400m. Below the 400m depth, the boundary starts to get skewed in the direction in which the rays travel across it.

3.1.3: Model 3

For this example, shown in figure 3.8, the model was designed to assess how accurately the inversion will locate the vertical boundary between the two rock units in a region of low ray coverage. As seen in the figure, the two slowness values present in the model are 0.222s/km and 0.166s/km (Duff, 2007), and the survey area used is 1000m wide and 1000m deep. 499 receivers at 2m intervals are placed in a 1000m deep vertical borehole located at x=500m; 50 surface shots with a peak frequency of 50Hz (Wardell, 1970) were recorded at 20m intervals along the surface.

The recorded travel-times for every shot were decimated by using every second travel-time to perform the inversion. Thus, 250 travel-times per shot were used to perform the inversion. Random Gaussian noise with a mean of zero and a standard deviation of 2ms was added.

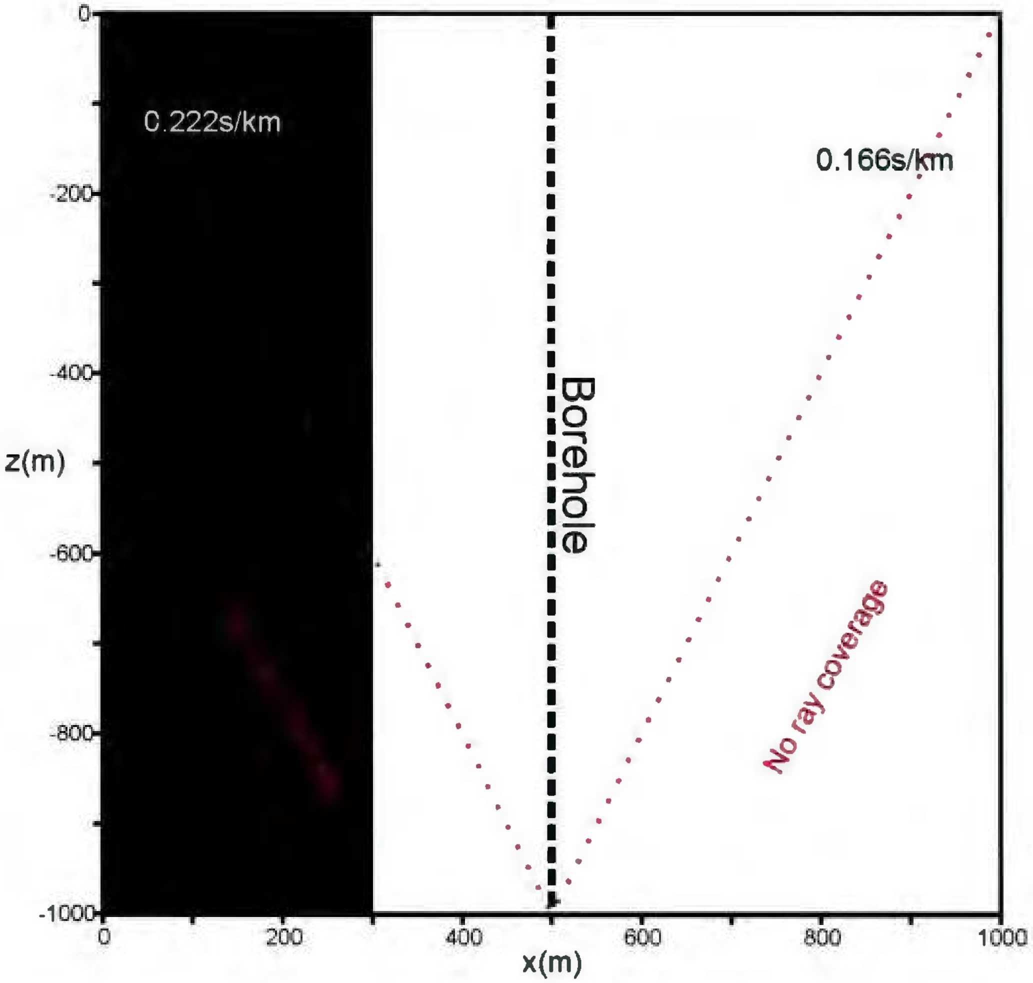

Figure 3.8: True model for model 3. The dotted red lines show the approximate limit of ray coverage.

The slowness tomogram for model 3 is shown in figure 3.9. In the tomogram, it is observed that the top 400m of the interface, which has a fair amount of ray coverage, was well resolved. Below this depth, ray coverage is minimal; hence, the rest of the boundary was not well resolved.

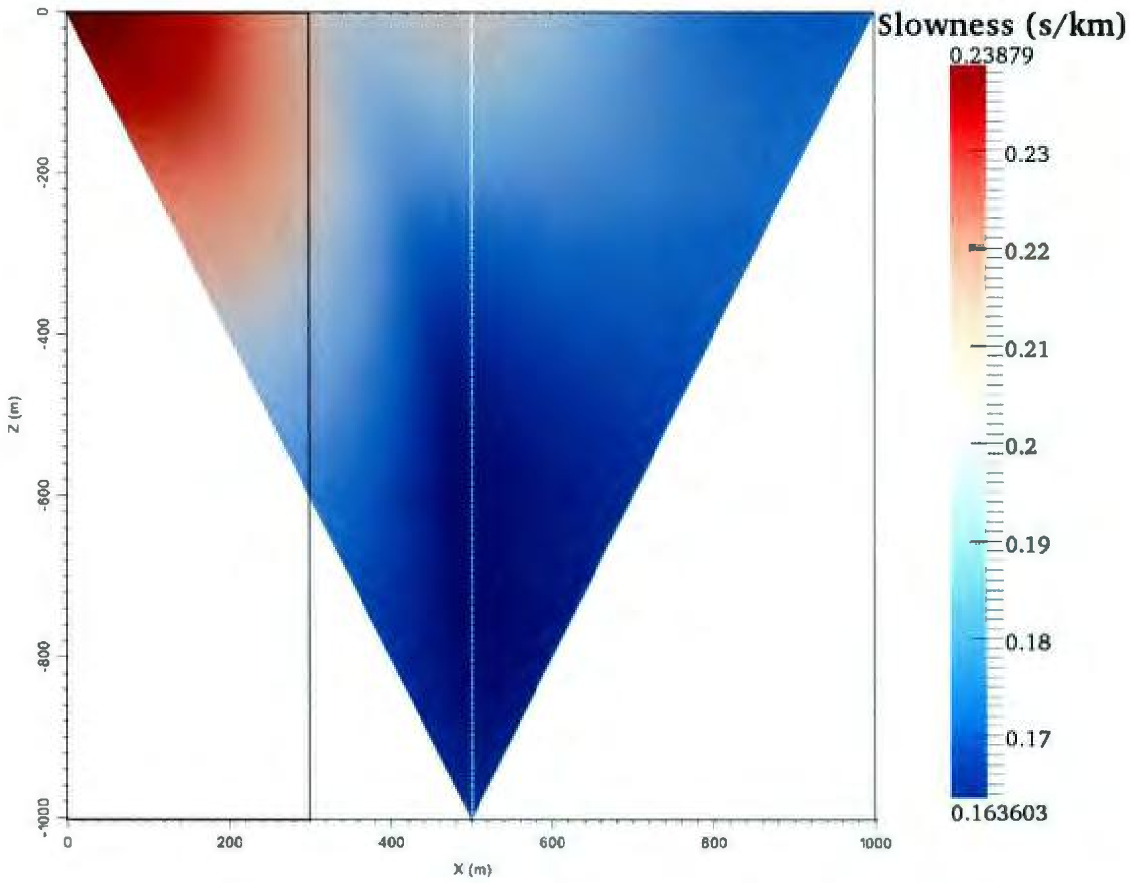

Figure 3.9: Inversion tomogram for model 3. The vertical bar on the right shows the slowness scale for the tomogram.

Following the analysis of the tomogram, analysis of the residual travel-times, shown in figure 3.10, was done. The residual plot for model 3 shows a pattern of high negative residual between travel-times that have sources near the borehole and receivers near the surface. This trend is directly related to the region of higher slowness around several source-receiver pairs around the top of borehole. As mentioned in model 1, this anomaly is caused by the variation in the methods of travel-time calculation of receivers close to the sources in the two different forward solvers used.

In addition to the near-offset source-receiver anomalies, a high positive residual travel-time pattern can also be observed for travel-times that have sources adjacent to the rock unit interface. This pattern is also identical to the pattern of residuals from model 1 (figure 3.5) and, as was previously noted, is likely as a result of the fuzzy boundary in the tomogram created by the minimum structure inversion method.

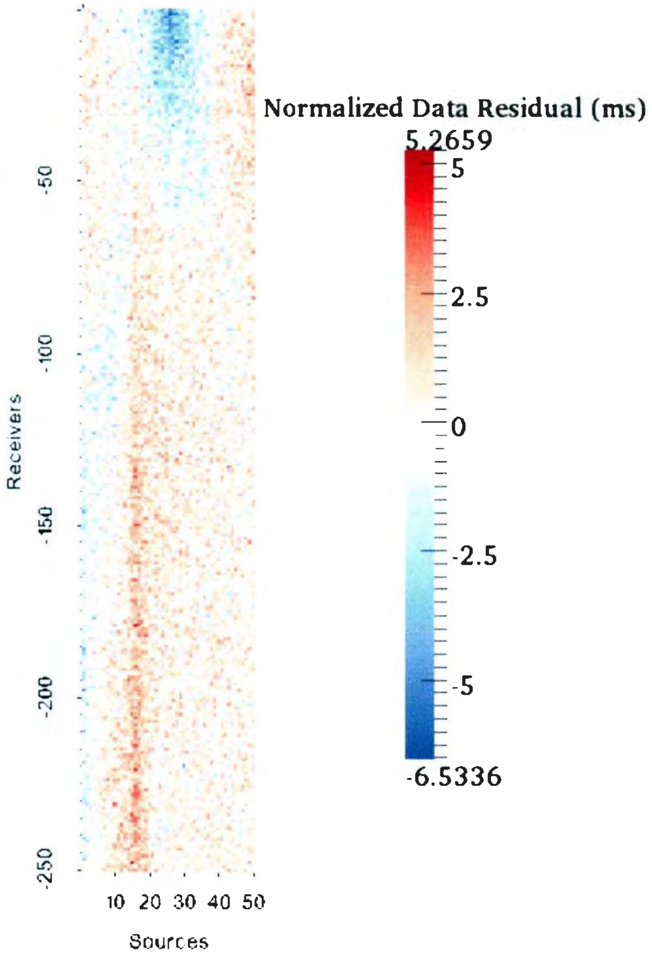

Figure 3.10: Residual travel-time plot for model 3

3.1.4: Model 4

The model, shown in figure 3.11, was developed to test the ability to resolve vertical and horizontal boundaries at depth. The slowness values, forward modeling parameters and inversion parameters used here are identical to those used in the previous examples.

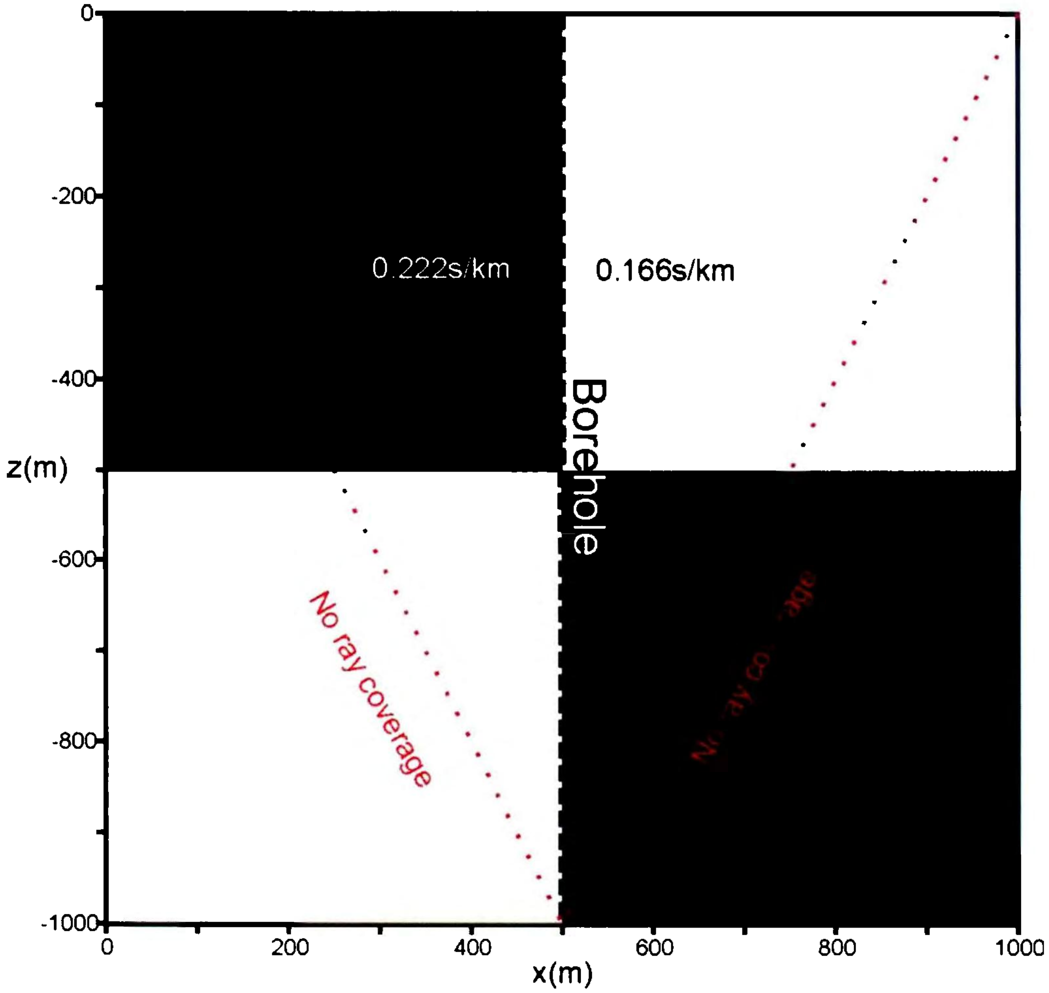

Figure 3.11: True model for model 4. The dotted red lines show the approximate limit of ray coverage.

After acquisition and inversion, the slowness tomogram for model 4 is shown in figure 3.12. In the tomogram, it was observed that the top 500m of the model was quite well resolved. Also, the vertical and horizontal boundaries in the model were well resolved and localized. At depths greater than 500m, only a small portion of the two blocks can potentially be resolved based on the ray coverage in that region. As shown here, the deeper faster block on the left (0.166s/km) was better resolved relative to the deeper slower block on the right (0.222s/km). The reason for the difference in resolution can be attributed to the direction in which emerging rays travel below the 500m boundary. In the model shown, for a ray traveling downwards from slow to fast medium, the emerging ray will travel more horizontally in the fast medium. Conversely, for a ray traveling downwards from the fast to slow medium, it will emerge traveling more vertically in the slow medium. The effect of these refractions means that for the left side of the model, the zone of ray coverage extends beyond the straight ray assumption used as a guide for describing ray coverage zones. This effect will be reversed on the right side of the borehole, because the zone of ray coverage will be reduced due to the refraction at the boundary. This means a smaller region of the body on the right of the model is sampled. As a result, the left side of the model is better resolved than the right, as seen in figure 3.12. The effects of refraction also accounts for why the bottom 500m of the model is better resolved on the left side of the tomogram.

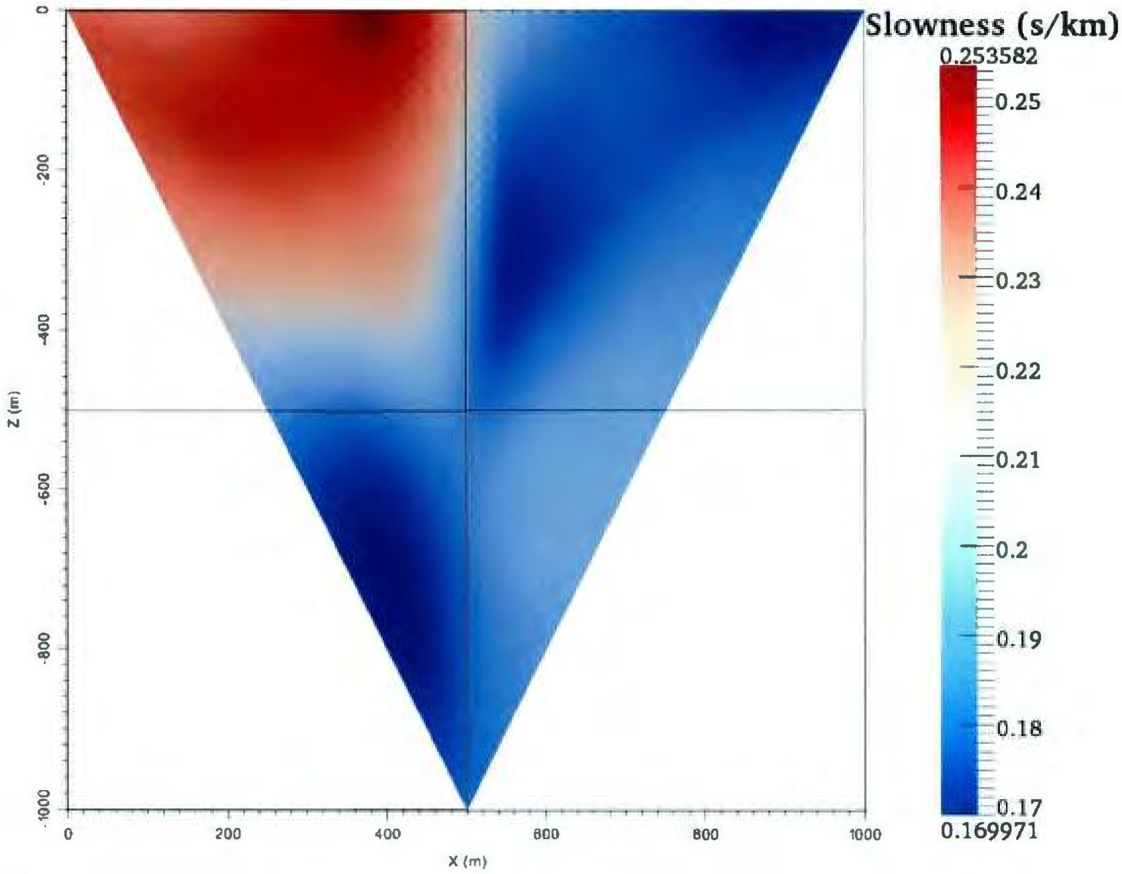

Figure 3.12: Inversion tomogram for model 4. The vertical bar on the right shows the slowness scale for the tomogram.

Analysis of the results of model 4 included the residual travel-times. However, the travel-time plot for model 4 does not contain new trends that are different from the trends observed from the residuals of previous models. Therefore, the residual for model 4 is located in the appendix A.

3.1.5: Model 5

The model, shown in figure 3.13, was designed to test the ability to resolve relatively small scale fluctuations in the subsurface. As with the previous model examples, the slowness values, forward model parameters and inversion parameters remain unchanged.

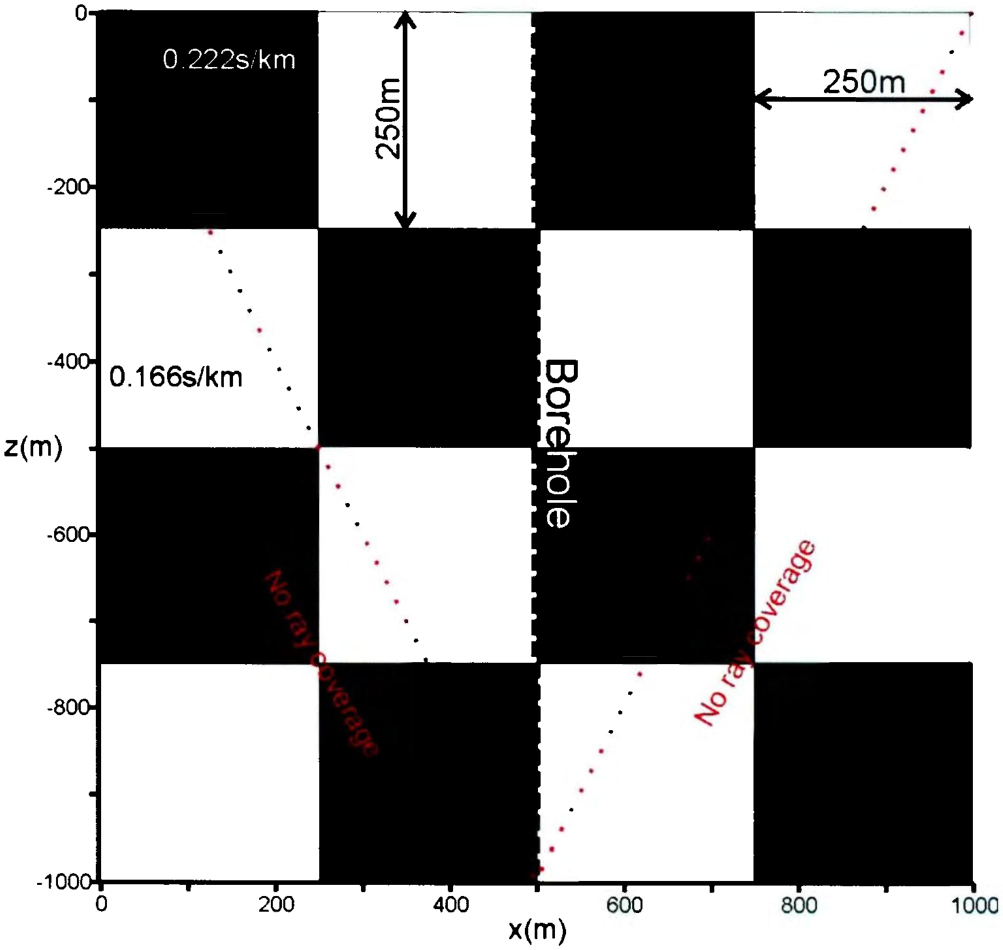

Figure 3.13: True model for model 5. The dotted red lines show the approximate limit of ray coverage.

In the inversion result shown in figure 3.14, it is observed that targets as small as 250m in the subsurface can be resolved by using surface-to-borehole tomography. A comparison of the two top squares on either side of the borehole shows that, despite both squares being in a region of similar ray coverage, the relatively slower square was better resolved than the faster square. The reason is likely due to the refraction of rays from surrounding blocks. In the case of the top square located to the direct left of the borehole (between x=250m and x=500m, and z=0m and z=250m), a ray that comes in from the relatively slower block to the left of it gets refracted and travels predominantly vertically. As can be seen from the tomogram, the slowness from every block the ray travels through averages out over the length of the raypath. In comparison to the top block directly to the right of the borehole (between x=500m and x=750m, and z=0m and z=250m), when a ray comes in from the relatively faster block on the right side, the ray gets refracted and travels in a predominantly horizontal direction, increasing the total area of the block sampled by the ray.

As observed in the tomogram, figure 3.14, resolution in the rest of the model occurs mainly along the directions in which the rays travel. Corner boundaries across the various squares are resolved parallel to the raypaths rather than in the checkerboard patterns expected. This can be attributed to the fact that rays travel mainly at one slowness rate from the source to the receiver along the diagonals of the squares in the model.

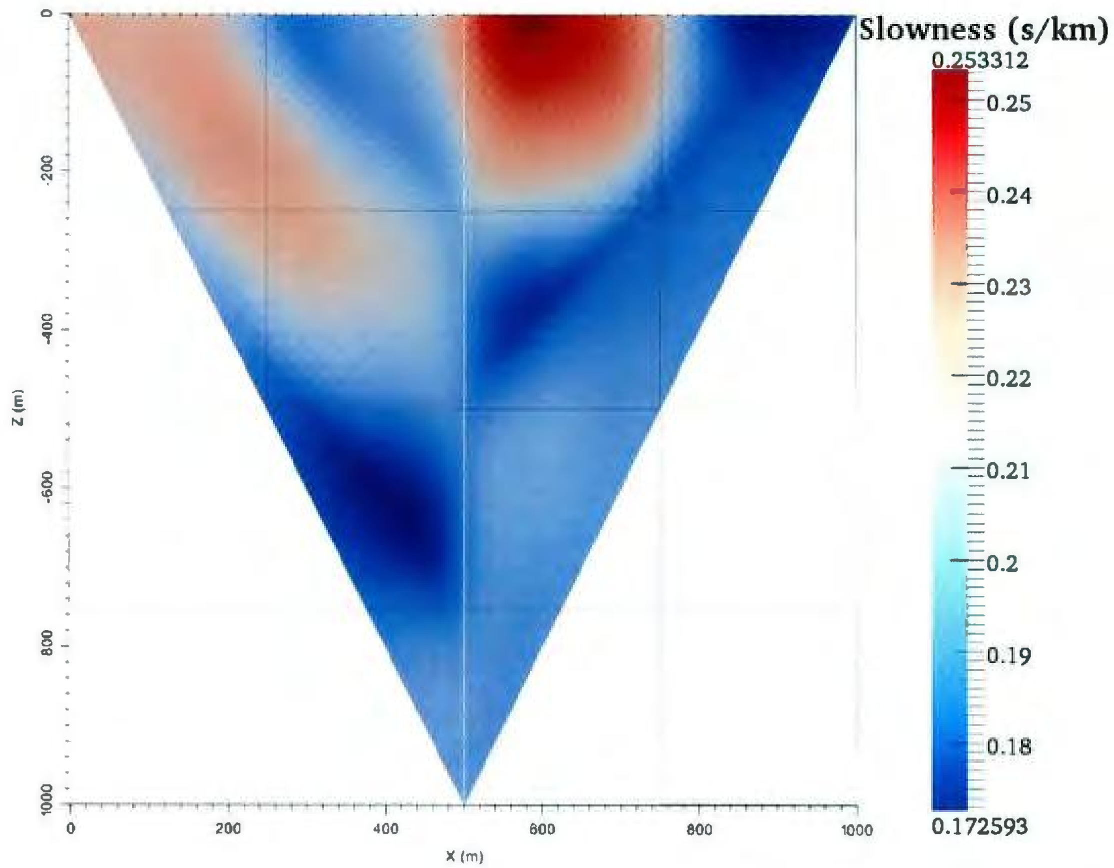

Figure 3.14: Inversion tomogram for model 5. The vertical bar on the right shows the slowness scale for the tomogram.

The residual plot did not contain any new trends that have not been observed in previous model residuals. Hence, the residual travel-time plot for this model can be found in the appendix A.

3.1.6: Model 6

For example 6, shown in figure 3.15, the model was designed to test the ability to resolve relatively small scale features in the subsurface. The dimension of each checkerboard square in this model is 100m by 100m. Forward modeling and inversion parameters used for the example here remain unchanged from those used in the previous models. Based on the slowness values and dominant frequency, the 100m squares are sampled by approximately one full wavelength (90m and 120m).

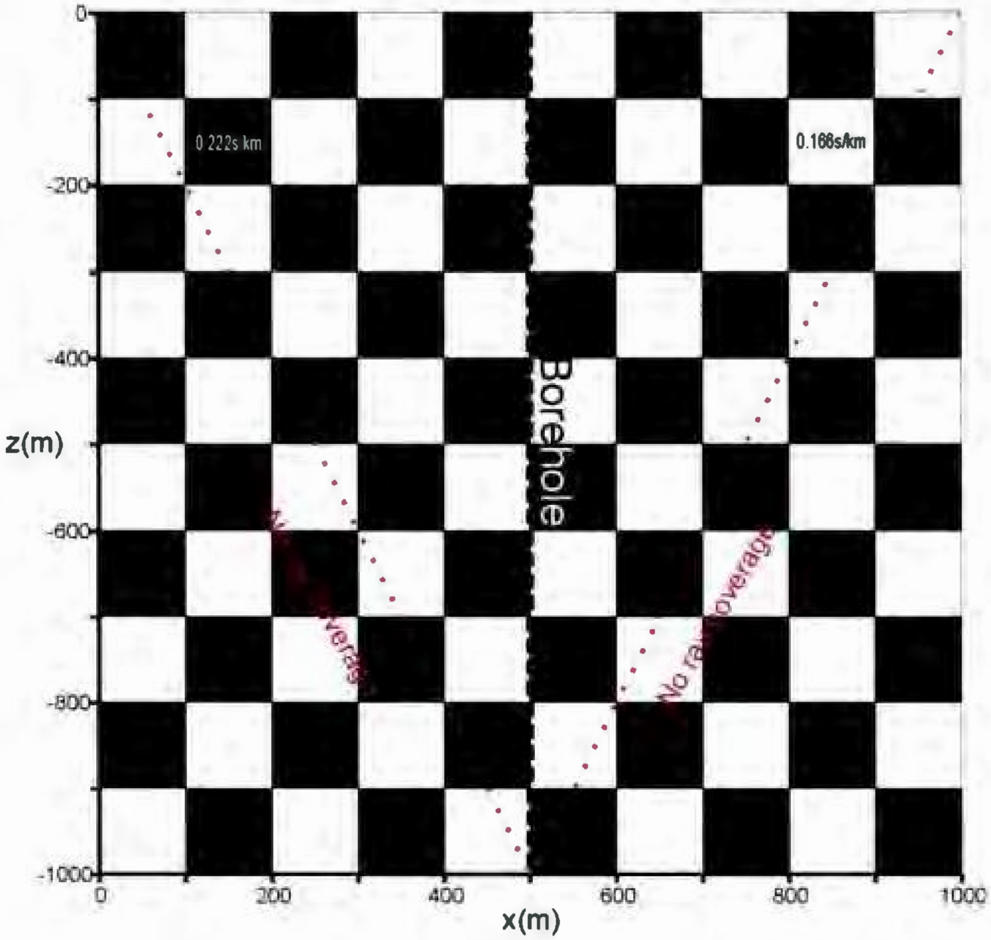

Figure 3.15: True model for model 6. The dotted red lines show the approximate limit of ray coverage.

In the tomogram shown in figure 3.16, it can be observed that the top slow block adjacent to the borehole was the only square fully resolved in the subsurface. This trend is similar to the 500m and 250m checkerboard examples. Another trend in the 100m checkerboard result that is similar to the 250m checkerboard tomogram is the resolution along the diagonal of the checkerboard; this can be attributed to rays traveling primarily at one slowness value along alternating diagonals (indicated by the arrows in figure 3.16) of the checkerboard. Resolution in the model is limited at depths beyond 400m because wave propagation gets increasingly complex with depth in the 100m checkerboard model.

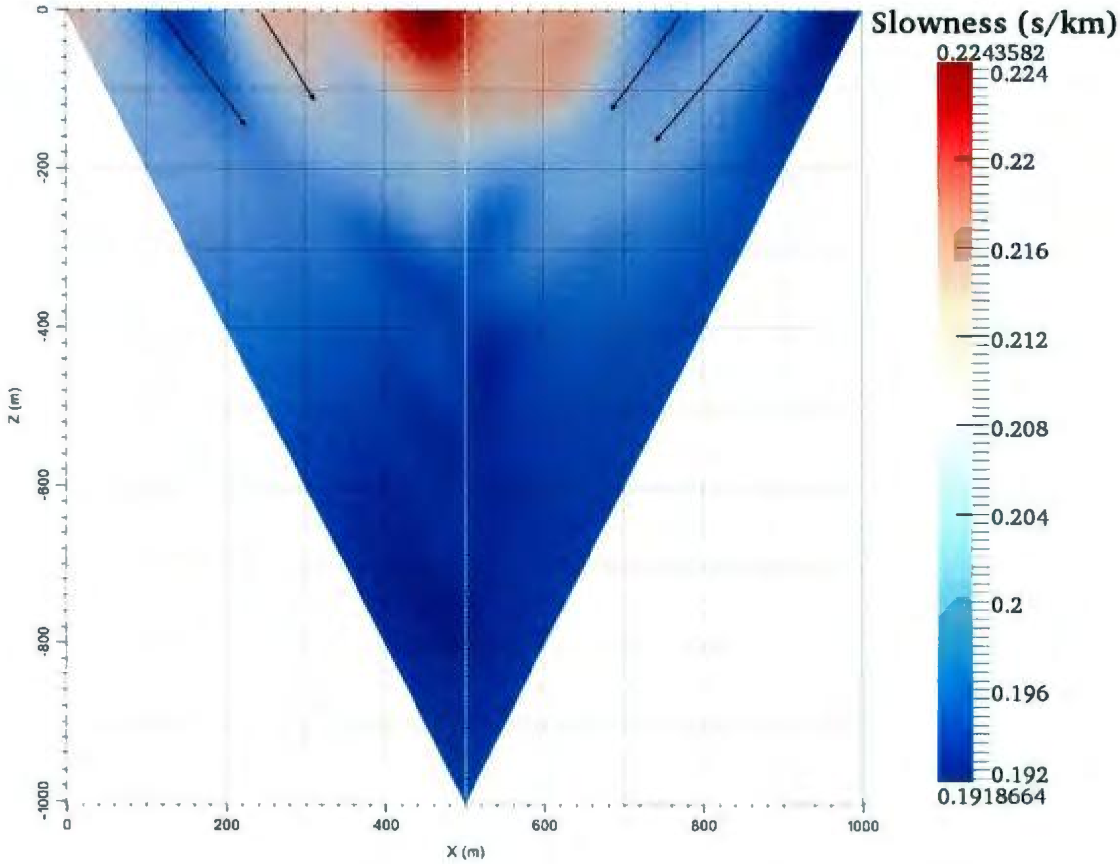

Figure 3.16: Slowness tomogram for model 6. The vertical bar on the right shows the slowness scale for the tomogram.

Further analysis of the result for the 100m checkerboard model included analyses of the residual travel-time plot shown in figure 3.17. In the residual plot, a trend of high negative residuals is observed between travel-times of sources close to the borehole and receivers close to the surface. Alternating bands of positive and negative residuals along the diagonals resolved is also observed. These bands are as a result of slowness values along the diagonals being resolved to be higher or lower than the true slowness values.

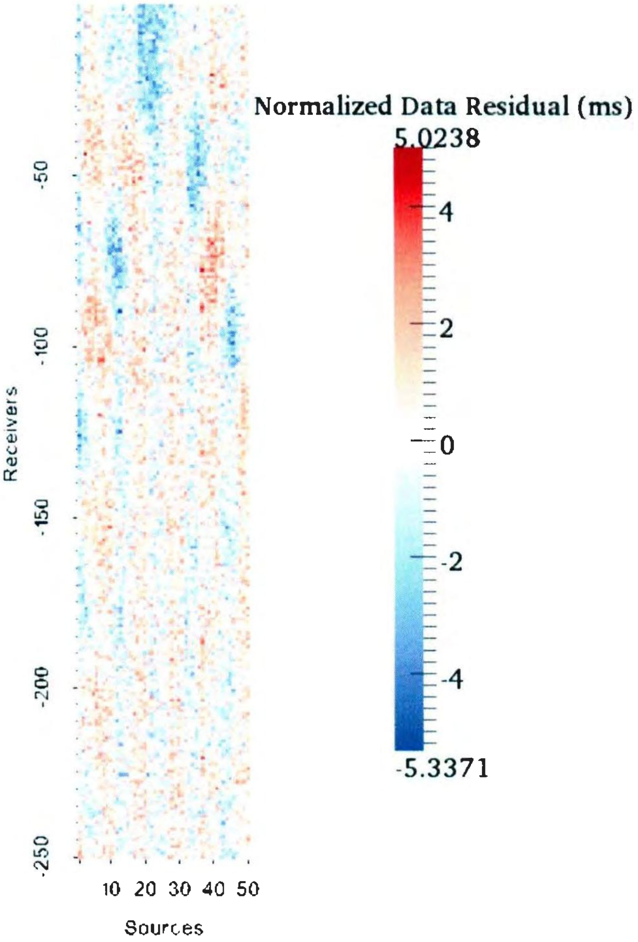

Figure 3.17: Residual travel-time plot for model 6.

3.1.7: Summary

For the test models presented, it is noted that, based on the acquisition geometry used, slowness contrast, and source frequency, the approximate depth for which a rock unit is resolvable is 50-60% the borehole depth. The 100 m checkerboard test also shows that targets as small as 100 m can be resolved in very shallow depths and very close proximity to the borehole. In addition, the tomograms of the 100 m and 250 m checkerboard tests show that slowness resolution is poor in the direction in which the recording rays travel. Slowness resolution in the ray direction is as a result of a significant proportion of the rays traveling from the source to receivers propagating primarily in one velocity zone along the diagonals.

Besides the effects of the acquisition geometry on the tomogram resolution, the refraction of rays affected the resolution of squares in the model. Rays going from faster to relatively slower squares refract at the boundary and travel in directions closer to the normal of the boundary. The refracted rays were therefore able to sample a larger area in the slower squares, hence increasing the ray coverage and chance of resolution in the squares. On the other hand, rays going from a slow to relatively fast square sampled less area in the faster square because the refracted rays travel in a direction father away from the normal of the boundary. Overall, resolution in the models presented is better in slower blocks next to the borehole than faster blocks next to the borehole.

Analysis of the residual travel-time plot shows that, in each example, anomalous residual travel-time patterns exist in travel-times between sources close to the borehole and receivers close to the surface. The cause of the pattern is a result of the varying forward solver methods used. The residual travel-time plots also exhibit anomalous residual travel-time values at the interface between slowness regions. The anomalous residual at rock interfaces is a result of the transition boundaries produced by minimum structure inversions.

3.2: Synthetic Geological Model Examples

The following model examples will further test the capabilities of the surface-to-borehole inversion geometry developed from earlier examples. The checkerboard tests indicated that resolution is poor in the direction parallel to the raypaths; that refraction of rays at slowness boundaries had an impact on the quality of object resolution; and that an object as small as 100m can be resolved if sampled correctly and if it is in a favourable proximity to the borehole. In addition to these lessons, the effect of angular coverage on inversion results is tested in this section.

The models used here were designed to be similar to geologic structures and slowness values present at the Voisey's Bay deposits in Labrador. The deposits in Voisey's Bay are contained in a troctolite-gabbro intrusion and dike complex that intrude into quartz-feldspar-biotite gneiss as well as garnetiferous paragneiss (Evans-Lamswood et al., 2000). The Reid Brook zone and the Eastern Deeps zone deposits are the areas that were selected to be modeled. The selected zones are ideal for testing because the geologic structures present are oriented at suitable angles and located at favourable depths for assessing the surface-to-borehole geometry. In addition, the slowness values of rocks in these regions present various contrasts (5%-30%) that can be tested to further understand how velocity contrasts affect resolution in a tomogram.

The interpretation of the results here follows a similar approach to the interpretation of the non-geological model tests; it includes interpreting the tomogram and comparing it to the known geologic model, followed by an analysis of the residual travel-time plots.

3.2.1: Model 7

The geometry of the geological model presented here (see figure 3.18) is similar to the Reid Brook zone deposit. The troctolite and massive sulphide in the area are hosted by a garnetiferous paragneiss (Evans-Lamswood et al., 2000). The gneiss host rock in the area has a slowness of 0.175s/km while the troctolite and massive sulphides have respective slowness values of 0.166s/km and 0.212s/km (Duff, 2007). The slowness contrast between the gneiss and the troctolite is 5%, and the contrast between the sulphide and the gneiss is 21%.

The set-up of the experiment includes 51 shots with a peak frequency of 60Hz (Wardell, 1970) taken at 20m spacing for a total coverage from 0m to 1000m. Acquisition was done with two 1000m deep vertical boreholes. The boreholes are located at x=201m and x=801m, and each borehole contains 500 receivers spaced at 2m intervals. Inversions were done using travel-times from borehole 1 only and borehole 2 only. A third inversion was done using a combination of travel-times from both boreholes 1 and 2.

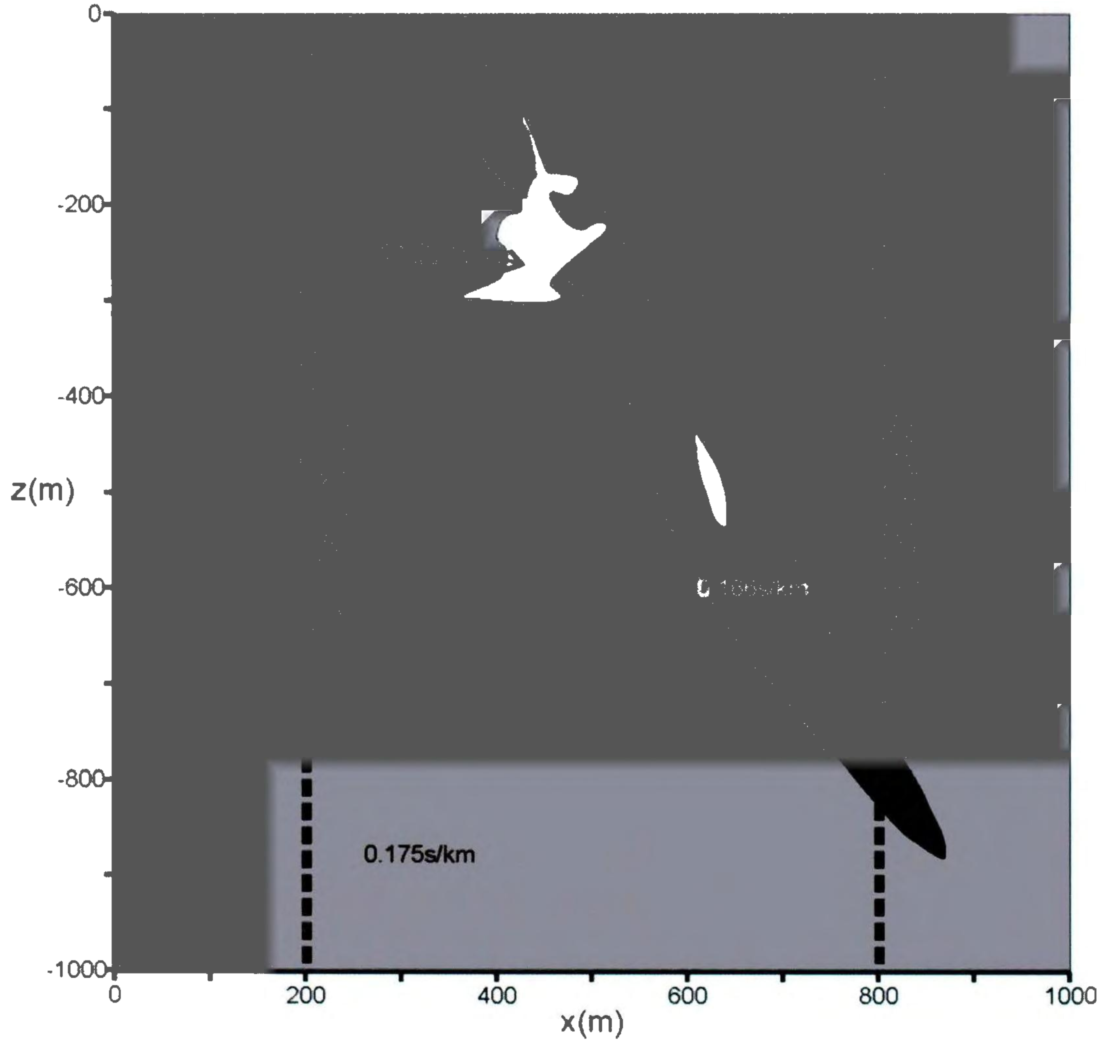

Figure 3.18: True model for model 7 with locations of boreholes used for acquisition.

For the first inversion performed, travel-times recorded in borehole 1 only were used to perform the inversion. The recorded travel-times containing information about the troctolite and sulphide traveled in a direction predominantly perpendicular to the orientation of the troctolite and sulphide. In contrast, for the second inversion, the travel-times recorded for borehole 2 only had rays that traveled predominantly in a direction parallel to the sulphide and troctolite. The third inversion uses a combination of rays that are parallel and perpendicular to the geology in the model. The first two inversions examine inversion results with respect to the orientation of the rays and orientation of the geology, while the third inversion examines the effects of varied angular coverage on inversion results.

To perform the first two inversions, the travel-times for every shot recorded in borehole 1 and 2 were decimated by using every second travel-time. Therefore, each inversion used 250 travel-times per shot to perform the inverse process. Also, random Gaussian noise with a mean of zero and a standard deviation of 2ms was added to the travel-times.

The slowness tomogram for the first inversion can be seen in figure 3.19. As observed from the tomogram, the inversion was able to resolve the location and relative size of the massive sulphide from the gneissic background. Due to the large velocity contrast between the sulphide and the gneiss (21%), the travel-times recorded by rays traveling through the sulphide and gneiss are significantly different from the travel-times of rays traveling through the troctolite and gneiss only. The distinct travel-times improve the chances of distinguishing the sulphide from the background rock. However, as can be observed from the tomogram, the portion of the troctolite located in the region of ray coverage was not distinguished from the background gneiss. The inability to resolve the troctolite is likely because all the travel-times that contained information about the troctolite also contained information about the gneiss. Therefore, it is probable that the inversion is unable to distinguish the presence of more than one slowness body and preferably distributes an average of both slowness values along the raypath. Also, as observed in the tomogram, the high slowness region indicated by the arrow is as a result of the use of varying forward and inverse solvers to calculate travel-times.

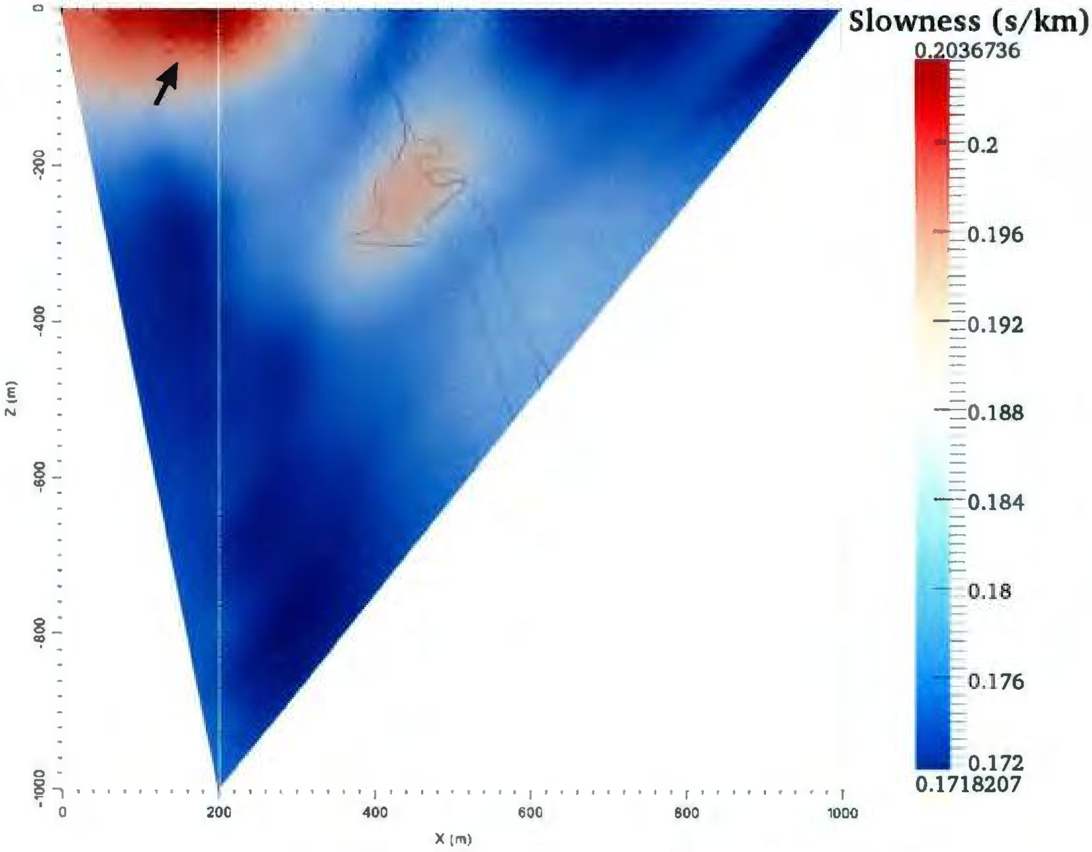

Figure 3.19: Slowness tomogram for model 7 using borehole 1 only. The vertical bar on the right shows the slowness scale for the tomogram.

The inversion result for the second inversion is shown figure 3.20. As is seen in the figure, the sulphide can be distinguished from the gneiss host rock. However, the sulphide is heavily smeared out along the direction of the raypaths. In the tomogram it is noticed as well that the troctolite is also distinguished from the gneiss, but only at depths of 600m-800m. The smearing out of the sulphide slowness likely prevents the inversion from resolving the troctolite until a depth of about 600m. The troctolite at depths from 600m to 800m was likely resolved because travel-time information from sources between 500m to 700m was able to constrain the troctolite slowness at that depth. Another feature observed in the tomogram is the region of high slowness indicated by the arrow. The cause of this high slowness feature can be attributed to the use of varying forward solvers in calculation forward modeling and inversion travel-times.

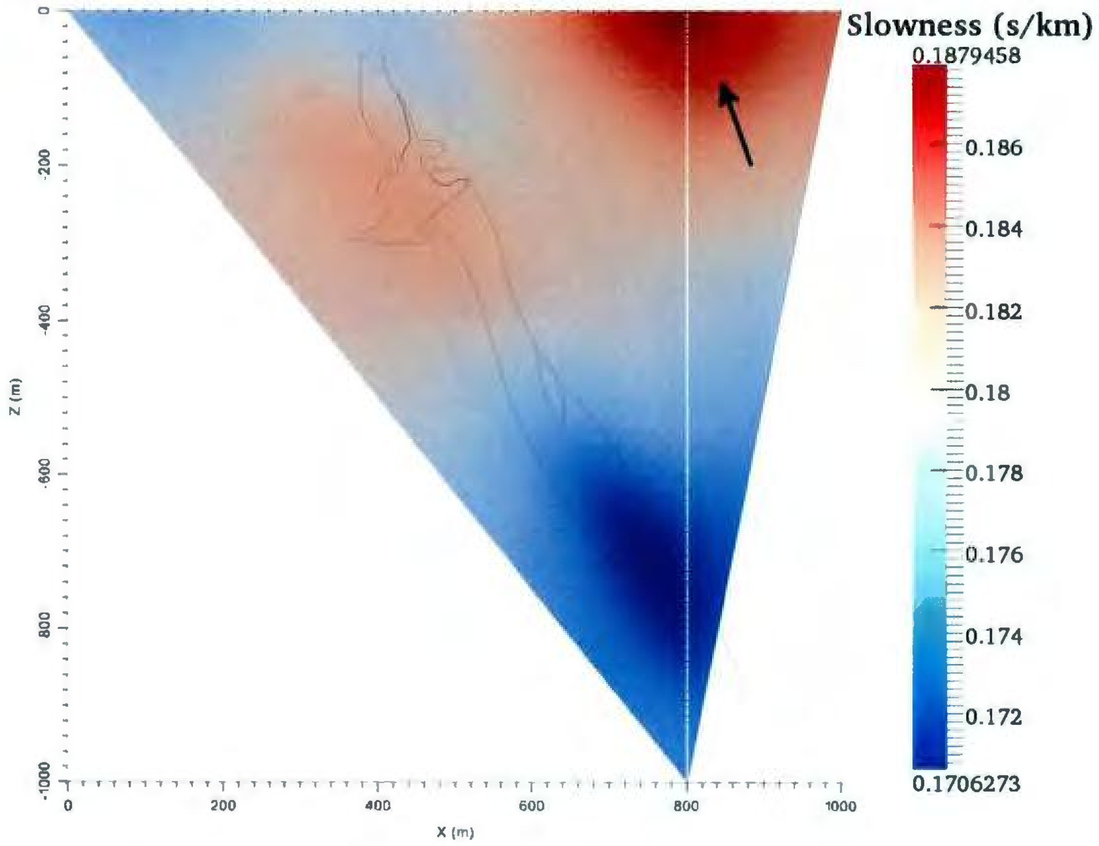

Figure 3.20: Slowness tomogram for model 7 using borehole 2 only. The vertical bar on the right shows the slowness scale for the tomogram.

For the third inversion, the recorded travel-times for every shot recorded in borehole 1 and 2 were decimated by selecting every fourth travel-time in each borehole. Hence, 125 receivers per borehole and a total of 250 travel-times per shot were used to perform the inversion. Random Gaussian noise with a mean of zero and a standard deviation of 2ms was also added.

Shown in figure 3.21 is the tomogram for the third inversion. The tomogram here shows that the massive sulphide and troctolite deposits are distinguished from the background gneiss. The increased angular coverage here was sufficient to improve the resolution of the various rock units in the subsurface. By using both boreholes, the number of rays and, more importantly, the variety of angular sampling of the region between the boreholes are increased. Based on the direction of ray propagation, the travel-times from one borehole serve as a form of constraint for the travel-times from the other borehole. In the tomogram, 2 regions of high slowness values in the shallow subsurface surround the boreholes as indicated by the arrows in the figure. These high slowness regions are similar to the high slowness regions observed in figure 3.19 and 3.20, and the cause of the anomalies is attributed to the use of varying solvers to calculate travel-times in the forward and inverse procedure. When the same solver (fast-marching) was used to perform the forward modeling and inversion of model 7, the very high slowness anomalies in the near surface were absent (refer to appendix A).

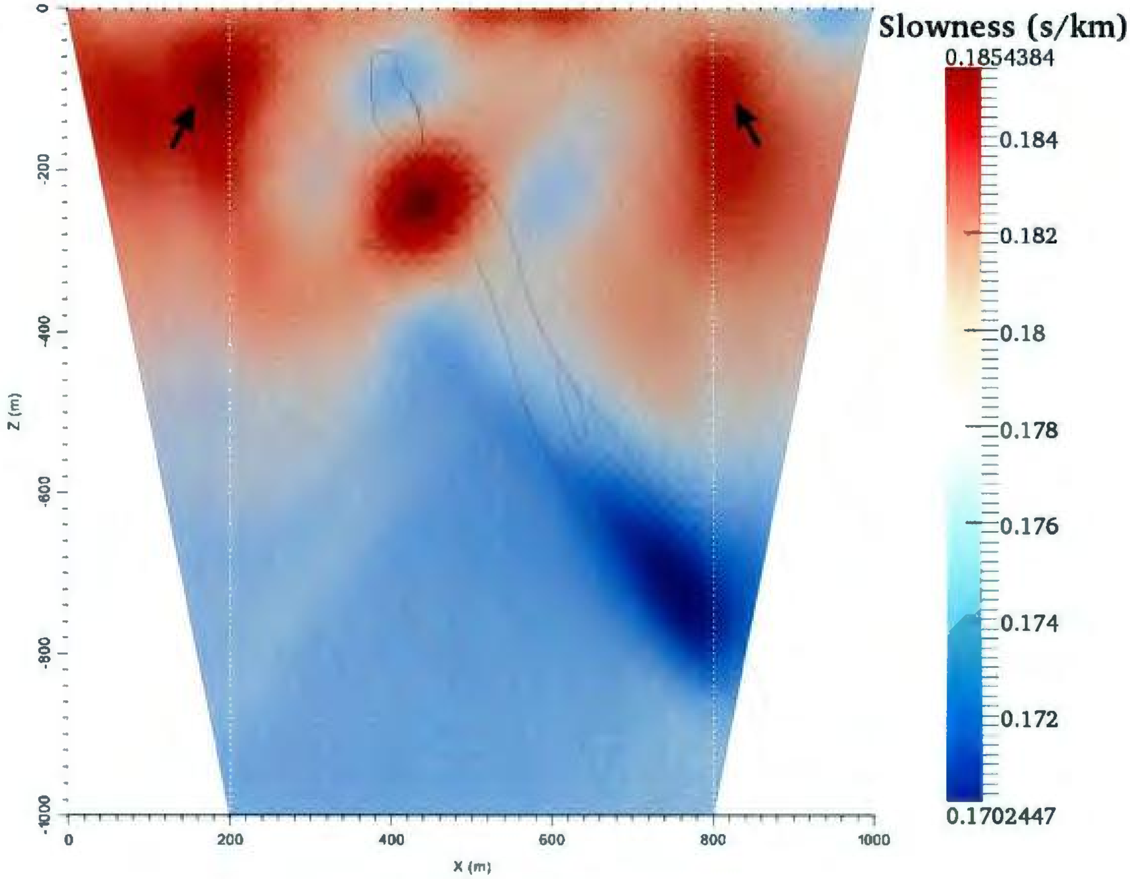

Figure 3.21: Slowness tomogram for model 7 using both borehole 1 and 2. The vertical bar on the right shows the slowness scale for the tomogram.

After analyzing the tomograms, the residual travel-times were analysed. A similar anomaly as seen in the previous models was observed. The anomalous trend detected is located around the travel-times of sources close to the boreholes and receivers close to the surface. As described earlier, this anomalous trend is a result of the different forward solvers used. Therefore, the residual travel-time plots for this model can be found in the appendix A.

3.2.2: Model 8

The model used for the example presented here is a geological representation of the Eastern Deeps zone of the Voisey's Bay deposit. As shown in figure 3.22, the Eastern Deeps zone consists of troctolite and massive sulphide rocks that are contained in a gneiss host rock. The slowness values assigned to each rock unit are 0.222s/km for the sulphide, 0.161s/km for the troctolite and 0.171s/km for the gneiss (Duff, 2007). The slowness contrast between the troctolite and sulphide is 30%, while the contrast between the troctolite and gneiss is 6%.

For the Eastern Deeps example, the goal of the model is to assess the capability of the method used to resolve the gneiss, troctolite and the sulphide at depth. The survey area, as seen in figure 3.22, is 2000m wide and 1000m deep. 51 shots each with a peak frequency of 60Hz (Wardell, 1970) were taken at 40m intervals. 4 boreholes located at x-locations of 301m, 601m, 1001m and 1701m were used to record travel-times. Each borehole used contained 500 receivers at spaced 2m intervals.

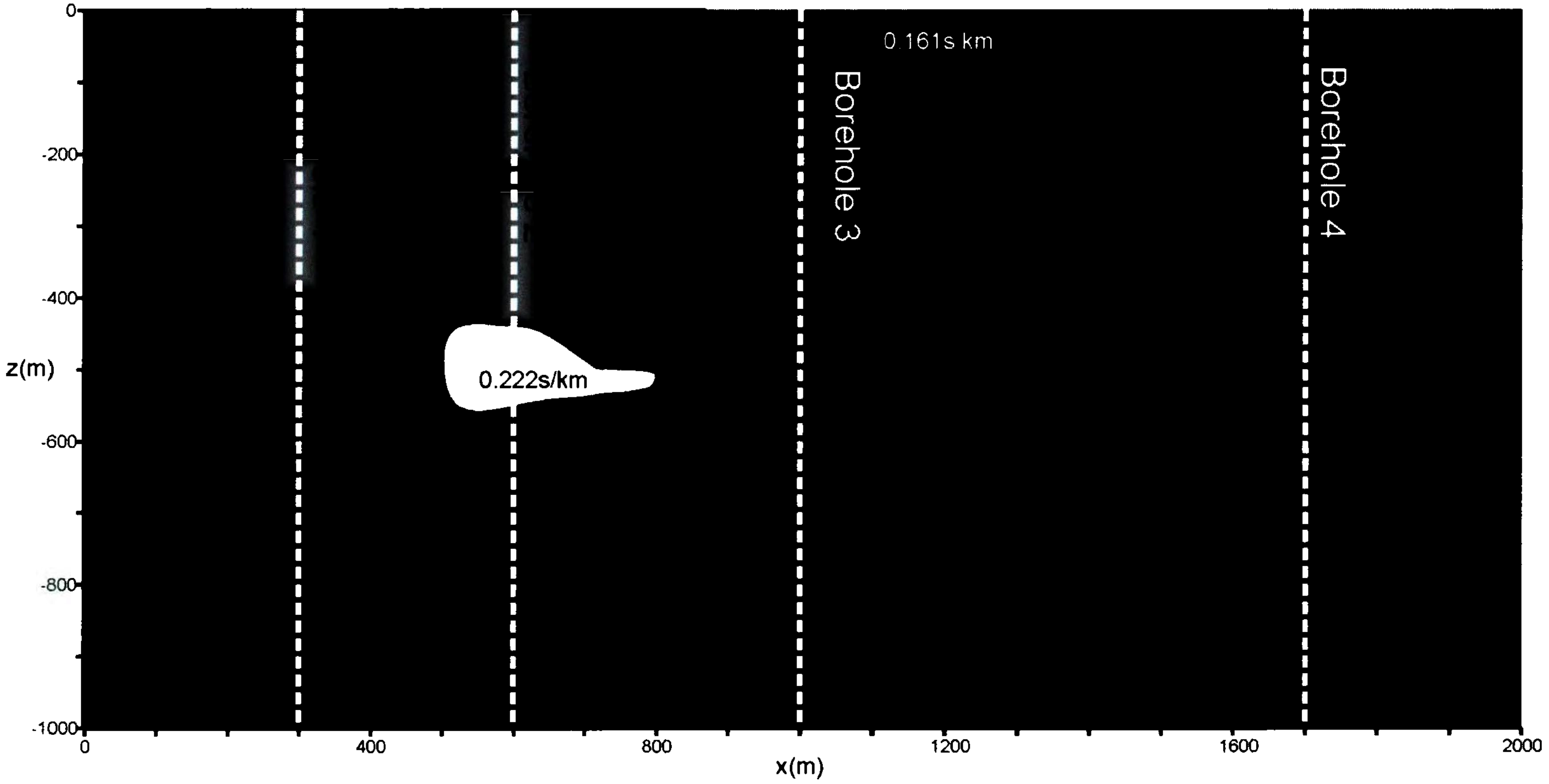

Figure 3.22: True model used for model 8. Locations of boreholes used for acquisition and inversion are indicated.

For the initial approach, the data from boreholes 1, 3 and 4 are used to perform the inversion. Boreholes 1, 3 and 4 were selected because the travel-times recorded in these boreholes cover a significant area in the subsurface, thereby improving the chance of characterizing a large portion of the survey area. In particular, data from boreholes 1 and 3 can potentially characterize the sulphide as was the case in the Reid Brook model example.

To perform the inversion using the three boreholes, the recorded travel-times for every shot in each borehole were decimated by selecting every fourth travel-time. Thus, 125 travel-times per borehole and 375 travel-times per shot were used to perform the inversion. Random Gaussian noise with a mean of zero and a standard deviation of 2ms was also added.

The slowness tomogram for the inversion run using boreholes 1, 3 and 4 can be seen in figure 3.23. As can be observed in the figure, the travel-times from the 3 boreholes were successful at distinguishing the troctolite unit from the gneiss rock unit; however, the sulphide was not successfully resolved. Upon further analysis of the result, it was determined that the sulphide was unresolved because the first arrival travel-times recorded avoided the low velocity sulphide by traveling around it in order to get to the receivers more quickly. One of the properties of first arrival travel-times is that they tend to avoid low velocity anomalies and preferentially sample high velocity anomalies (Rawlinson et al., 2010). Therefore, with the sulphide having a much higher slowness (30%) than its surrounding rocks, the rays that travel around the slower sulphide body get to the receivers faster than rays that travel through the sulphide. Hence, the first arrival travel-times will carry little or no information about the sulphide. In addition, the depth of the sulphide target may have had an effect on the ability to resolve the sulphide body. The dimensions and rock properties of the Eastern Deeps sulphide and its host are similar to the dimensions and rock properties of the Reid Brook sulphide body. However, the depths of both sulphides vary considerably with the Reid Brook sulphide being shallower (~250m) compared to the Eastern Deeps sulphide located at an approximate depth of 500m. The Reid Brook sulphide was well resolved but the body was much shallower, and perhaps this made it more readily resolved.

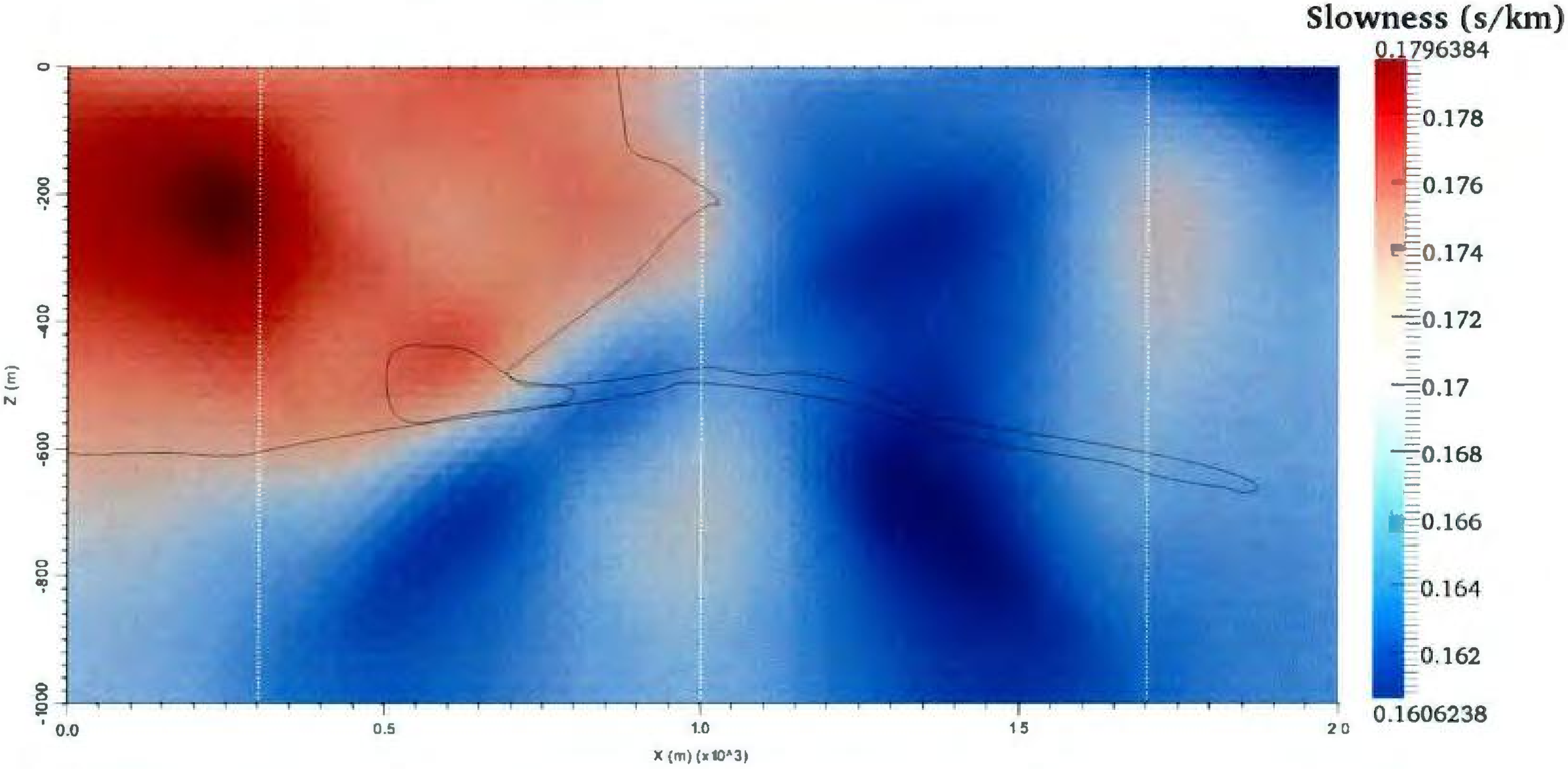

Figure 3.23: Slowness tomogram for model 8 using borehole 1, 3 and 4 only. The vertical bar on the right shows the slowness scale for the tomogram.

In order to resolve the sulphide, the inversion was performed using data from borehole 2 in addition to data from boreholes 1, 3 and 4. The recorded travel-times for every shot in each borehole were also decimated by selecting every fourth travel-time. Thus, 125 travel-times per borehole and 500 travel-times per shot were used to perform the inversion. Random Gaussian noise with a mean of zero and a standard deviation of 2ms was also added.

The result of the inversion from using data from all 4 boreholes can be seen in figure 3.24. As can be seen in the tomogram, using data from borehole 2 helped to resolve the sulphide, in addition to the troctolite and gneiss. The location of borehole 2 improves the sampling of the sulphide because it enables the rays that pass through the sulphide to be recorded as first arrival times, rather than later arrival at boreholes 1 and 3.

After analysing the tomogram, the residual travel-times for both inversions were analysed. The residual plots for the inversion using data from boreholes 1, 3 and 4 is shown in figure 3.25, while the residual plot for data from boreholes 1, 2, 3 and 4 is shown in figure 3.26. In the residual plots for both inversion runs, a circular pattern of high negative residual travel-time in the bottom right quadrant of the plot can be observed. The reason for the negative pattern is unknown, but it can be noted that the travel-times are associated with rays in the vicinity of the sulphide. Furthermore, in figure 3.26, for the residual plot in borehole 2, a horizontal trend of high negative can be noticed at depths of approximately 500-600m in the borehole. The reason is likely due to the lower sulphide slowness in the tomogram (figure 3.24) than the true geologic model. Therefore, the predicted travel-times will arrive earlier than the observed travel-times.

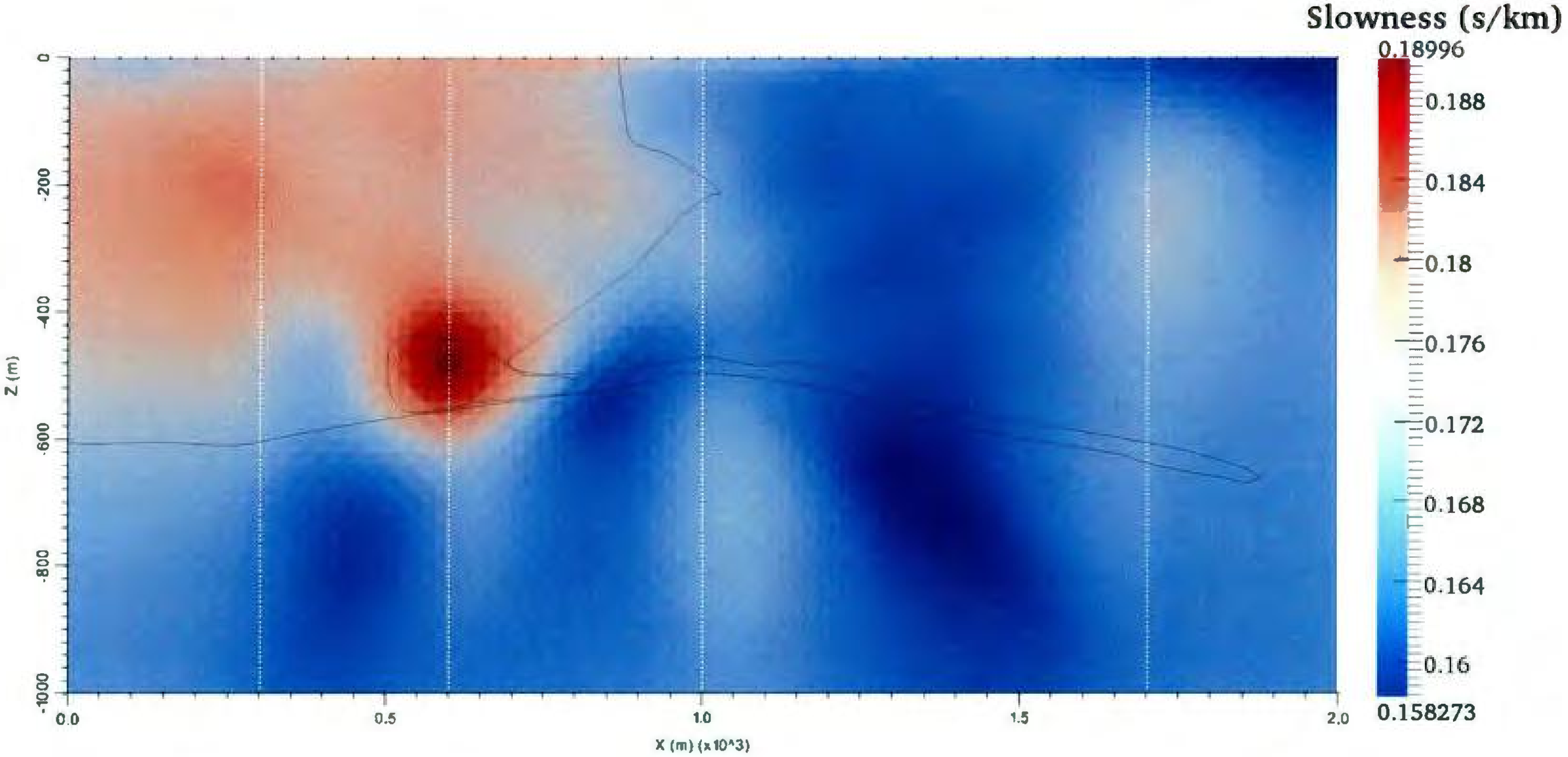

Figure 3.24: Slowness tomogram for model 8 using borehole 1, 2, 3 and 4. The vertical bar on the right shows the slowness scale for the tomogram.

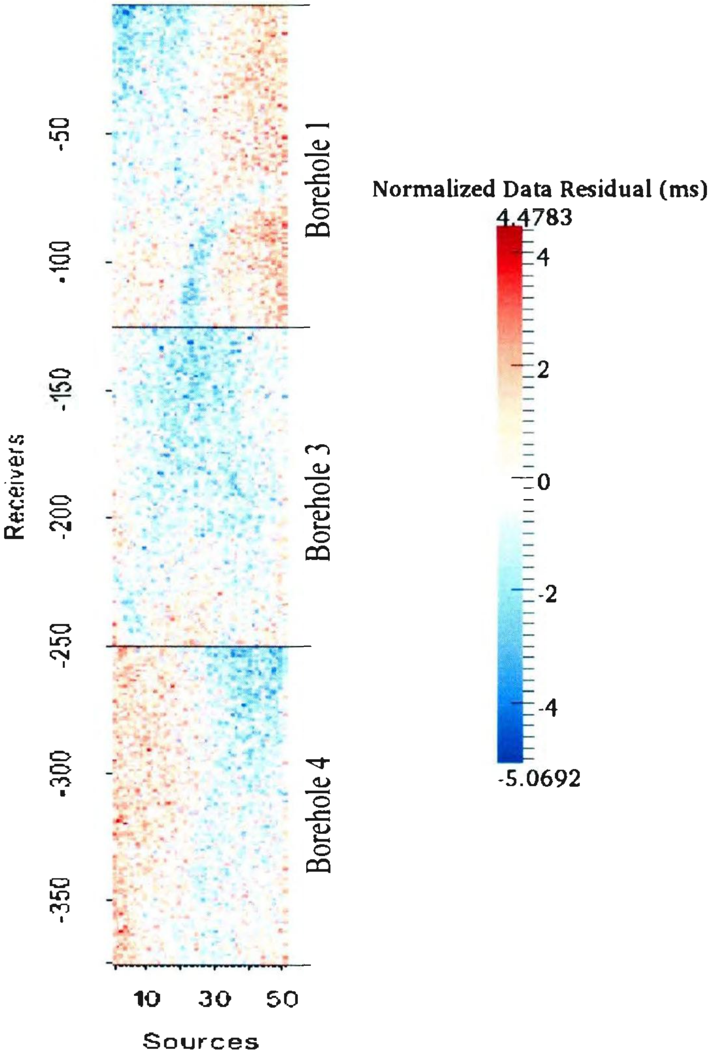

Figure 3.25: Residual travel-time plot for model 8 inversion using boreholes 1, 3 and 4 only.

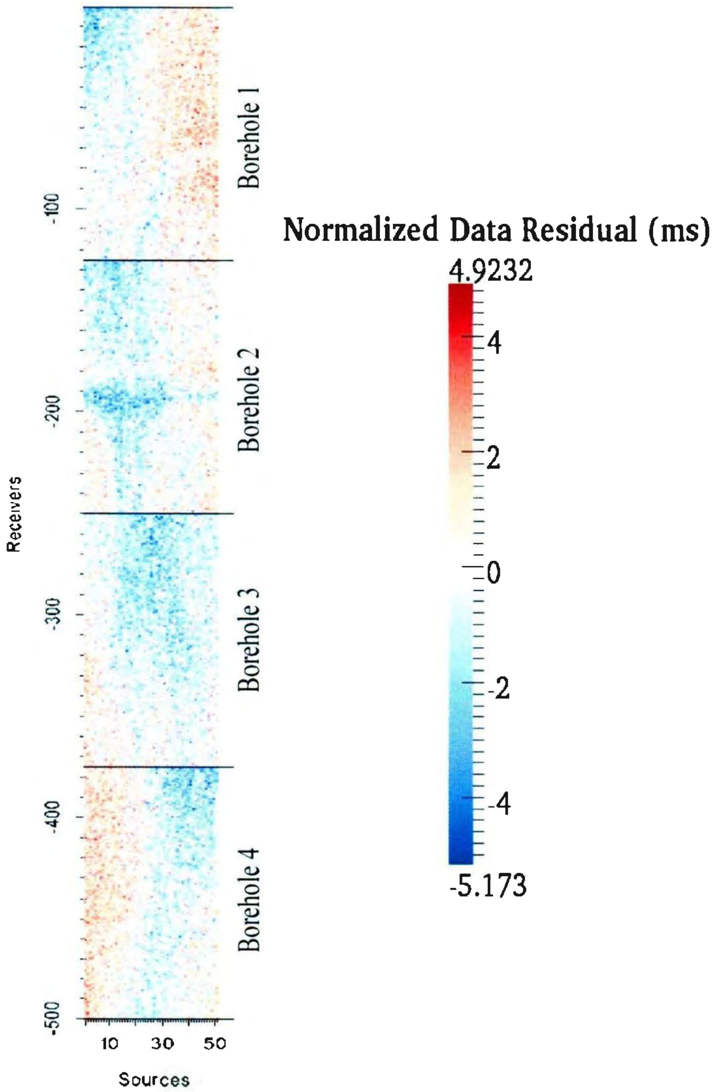

Figure 3.26: Residual travel-time plot for model 8 inversion using boreholes 1, 2, 3 and 4.

3.2.3: Summary

In model 7 (Reid Brook zone), it was observed that when a single borehole was used to invert geology perpendicular to the direction of recording raypaths, the result obtained was unable to localize the object along the raypaths. However, using multiple boreholes on either side of the geology of interest helped localize the geology. The reason for this is that rays recorded in one borehole act as constraints along the raypaths of the other borehole, thereby improving the potential of localizing geology. In addition, recording in multiple boreholes improves the angular ray coverage of the subsurface. The model results obtained in model 7 demonstrate that increased sampling of a region by multiple rays in a variety of angles increases the chance of resolution of that region. Increased angular coverage improves the resolution of the subsurface as suggested by authors such as Kanli et al. (2008) and Leblanc et al. (2004).

In model 8 (Eastern Deeps zone), three boreholes were initially used to try and resolve the geology in the subsurface. Inversion using the three boreholes was able to distinguish the gneiss and the troctolite but the sulphide was unresolved. The sulphide was unresolved because the first arrival travel-times recorded in the three boreholes traveled around the slow sulphide in order to get to the boreholes faster. When travel-times from the borehole intersecting the sulphide were added to the inversion, it helped to record the travel-times that passed through the sulphide as first-arrival times. Thus, when the inversion was done using all four boreholes, the sulphide was resolved. Slowness information about the sulphide was provided by the travel-times recorded in the borehole which intersects the sulphide. The presence of such slowness information helped in resolving the sulphide.

3.3: Geological models with near-surface weathering layer.

Based on the results from the previous section, the use of multiple boreholes to perform surface-to-borehole tomography increased the angular ray coverage of the subsurface. Increasing the range of angles in which rays sample a region is important because increased angular ray coverage improves the ability to resolve the subsurface (Kanli et al., 2008). Here, an analysis of the effects related to the presence of a near-surface weathering layer is performed. The near-surface weathering layer is usually the portion of the subsurface where air rather than water fills the pore spaces of rocks and unconsolidated earth (Sheriff and Geldart, 1995). This near-surface weathering layer, often known as a low-velocity layer or overburden, is characterized by low seismic velocity within the layer and a sharp increase in velocity at the base of the layer (Sheriff and Geldart, 1995). Due to the large variation in velocity between the near-surface weathering layer and the bedrock, it is important to investigate how much the inversion smears out the slowness of the low-velocity layer into the geology below it, and what effect this will have on the resolution of the geology.

For the study of overburden effects on inversion resolution, three different inversions are done for each model example. The first inversion is performed on the model designed without an overburden present. The purpose of the first inversion is to get an initial evaluation of how well the model can be resolved. The second inversion is done on the model with an overburden present. The third inversion is also done on the model with an overburden present. However, the inversion mesh that is used to perform the third inversion is a constrained inversion mesh. The constrained mesh is used here because it enables constraints such as slowness constraints to be added to the inversion, with the hope of achieving a better resolution in the subsurface.

3.3.1a: Model 9.0

Model 9, shown in figure 3.27, was adapted from a geological model of the Sossego copper mine located in the southeast of Para State, Brazil (Tammerik et al., 2009). The model here was selected because of the uncomplicated geology, favorable depth of the target rock, and a moderate velocity contrast of 20% between the ore and host rock. The geology of the host rock is mainly granite, and the orebody is a breccia consisting of a variety of minerals such as quartz, actinolite, sulphide, carbonates and oxide minerals (Tammerik et al., 2009). The host rock was assigned a seismic slowness value of 0.179s/km, and based on the minerals constituents of the ore, it was assigned a slowness of 0.143s/km (Sheriff and Geldart, 1995). The survey area is 1000m wide and 1000m deep. 51 shots with a peak frequency of 60Hz (Wardell, 1970) were taken at 20m intervals from 0-1000m. While 1000 receivers spaced at 1m intervals were used to record travel-time information in a borehole located at x=451m.

To perform the travel-time inversion, the data was decimated by selecting every fourth travel-time. Thus, a receiver spacing 4m and a total of 250 travel-times per shot were used to perform the inversion. Random Gaussian noise with a mean of zero and a standard deviation of 2ms was also added.

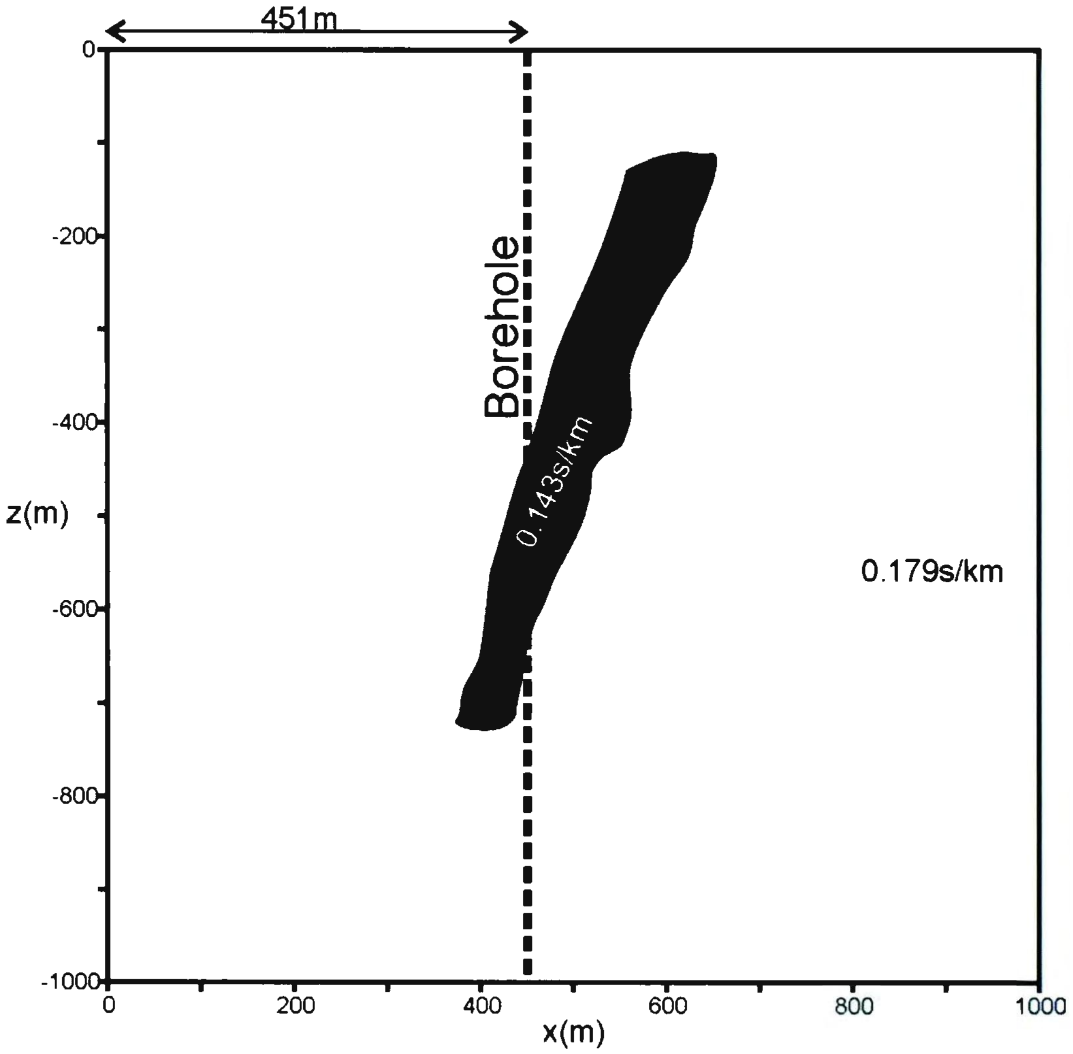

Figure 3.27: True model for model 9 without an overburden.

The inversion result shown in figure 3.28 is for the inversion of model 9 without an overburden present. As can be seen from the result, the orebody was well resolved and localized in the subsurface.

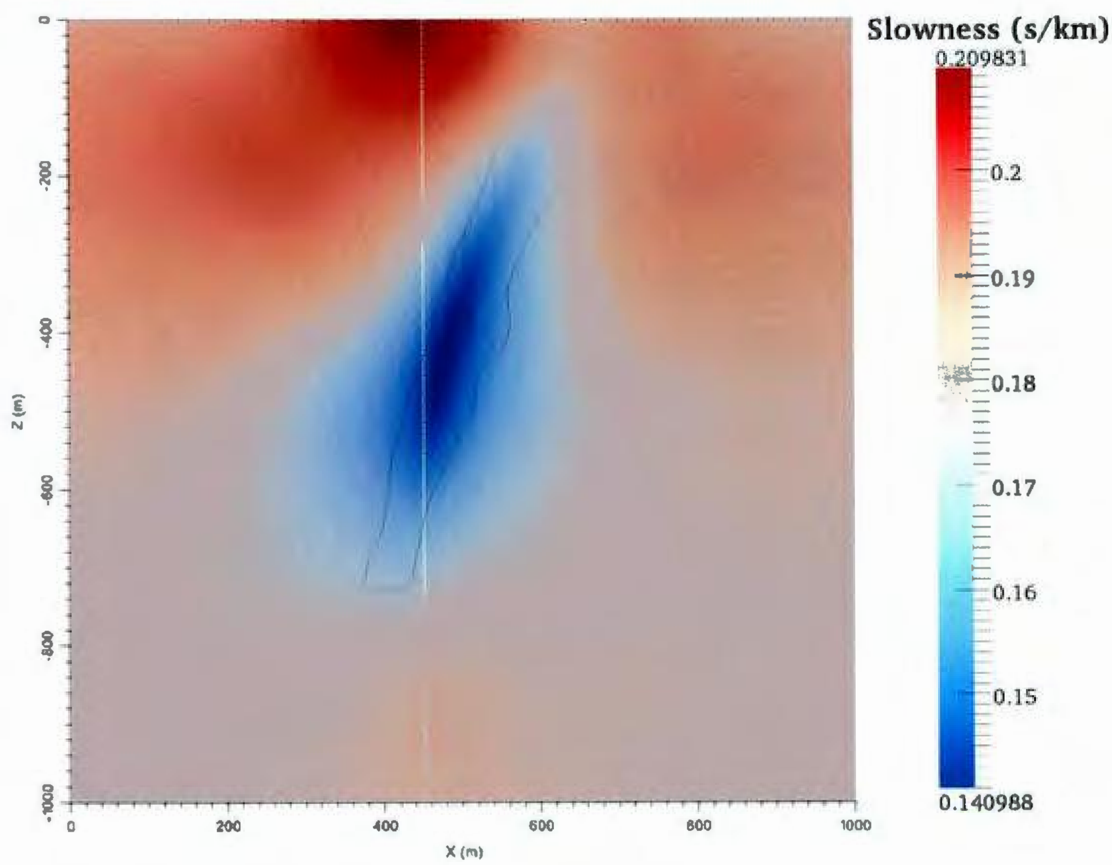

Figure 3.28: Slowness tomogram for model 9 inversion with no overburden. The vertical bar on the right shows the slowness scale for the tomogram.

3.3.1b: Model 9.1

Figure 3.29 is a model of the Sossego mine area (Tammerik et al., 2009) with a low-velocity layer present. The low-velocity layer was assigned a slowness of 0.5s/km, while the host rock and ore have a slowness of 0.179km and 0.143s/km (Sheriff and Geldart, 1995), respectively. Based on the slowness values, a 64% contrast exists between the overburden and host rock boundary. The thickness of the overburden increases gradually from 30m at x=0m to 96m at x=1000m. The acquisition parameters used for the test include 51 shots with a peak frequency of 60Hz (Wardell, 1970) taken at 20m intervals; and 1000 receivers spaced at 1m intervals in a borehole located at x=451m.

To perform the travel-time inversion, the data was decimated by using every fourth travel-time recorded. Thus, a receiver spacing 4m and a total of 250 travel-times per shot were used to perform the inversion. Random Gaussian noise with a mean of zero and a standard deviation of 2ms was also added.

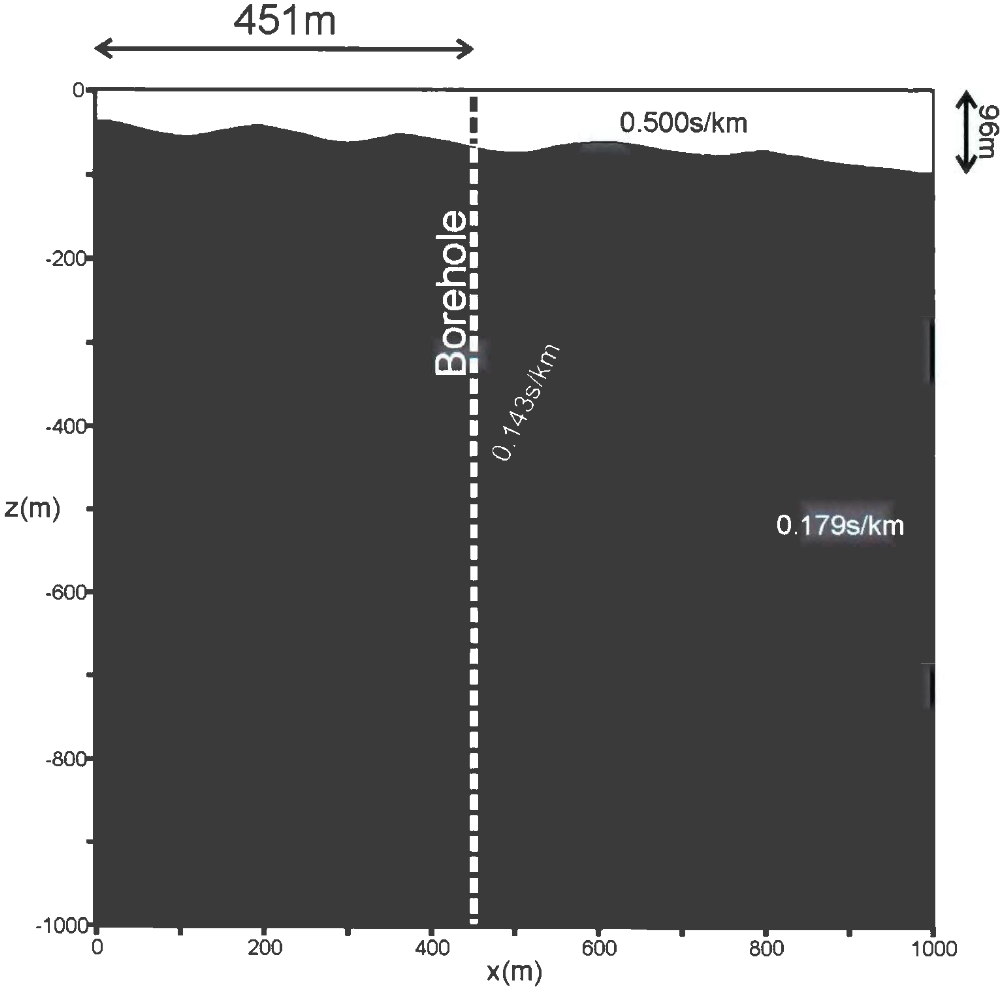

Figure 3.29: True model for model 9.1. The same model as model 9.0 but a near-surface low-velocity layer is included.

The result of an unconstrained inversion of the model is shown in figure 3.30. As can be seen from the tomogram, the overburden was well resolved and vertically constrained up to about 200m on either side of the borehole. However, at distances greater than 200m away from the borehole the overburden and the host rock cannot be distinguished. In the tomogram, it is observed that the ore can be distinguished from the surrounding host rock. The orebody is resolved because it is located in the region directly below the well localized section of the overburden. Therefore, due to the absence of the smeared out slowness from the overburden above, the proper slowness distribution can be achieved in the ore.

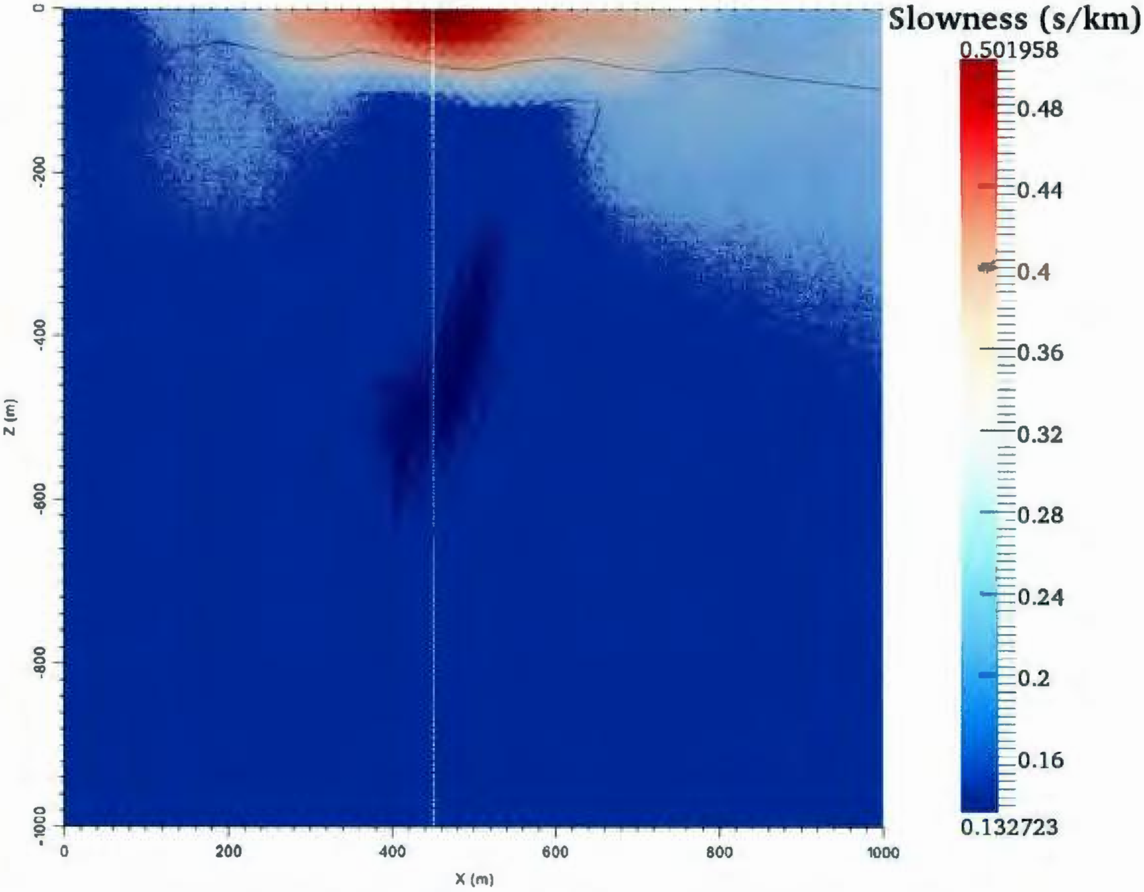

Figure 3.30: slowness tomogram for model 9.1. The vertical bar on the right shows the slowness scale for the tomogram.

After analyzing the tomogram, the residual travel-time plot for the unconstrained inversion of model 9 with an overburden is shown in figure 3.31. For far offset sources in the model, the plot displays a horizontal trend of high positive residual travel-times at approximate receiver depths of 50-100m. The high positive residual trend can be attributed to the high average slowness in the tomogram between the far-offset sources and the receivers at the 50-100m depth. In the plot, a high negative residual is also observed between sources close to the borehole and receivers near the surface. Here, the slowness values in that region of the tomogram are slower than the true slowness values of the model. This makes the predicted travel-times arrive at the receivers faster than the observed travel-times.

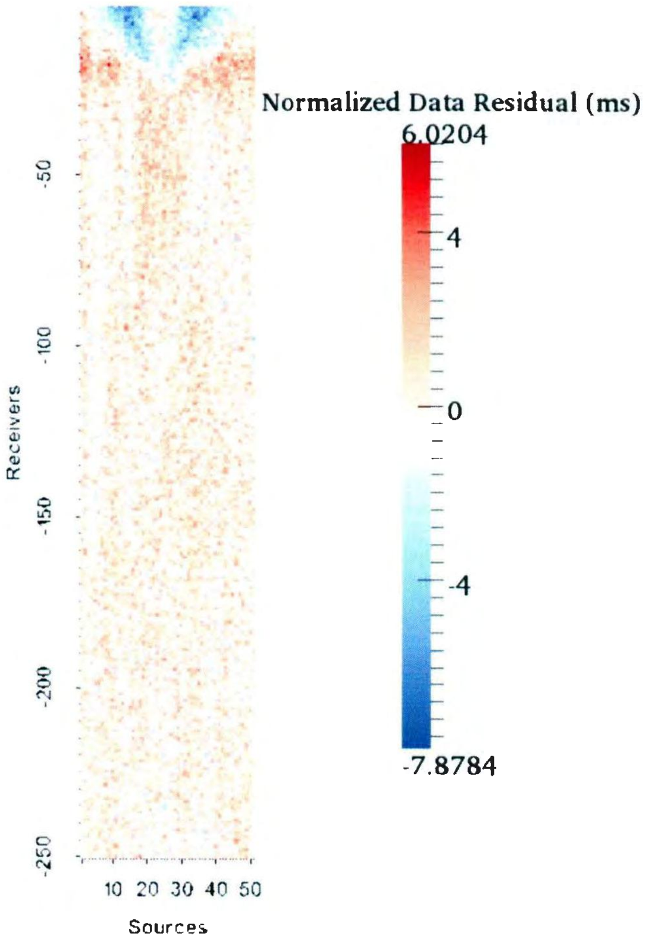

Figure 3.31: Residual travel-time plot for model 9.1 using an unconstrained inversion.

3.3.1c: Model 9.1

To reduce the effects of the near-surface overburden slowness smearing down into the geology below it, the inversion is performed with a constrained inversion mesh. The mesh, shown in figure 3.32, has structural constraints and slowness value constraints applied to it. By using structural constraints, different slowness constraints can be applied to different sections of the mesh. Values and bounds for the slowness constraints applied can be derived from prior information about the survey area (Lelièvre et al., 2011b) or by using guesstimated values and depths based on geologically realistic rock velocities. In order to apply constraints to the mesh, triangular meshes were used because they allow the structure to be included in the mesh.

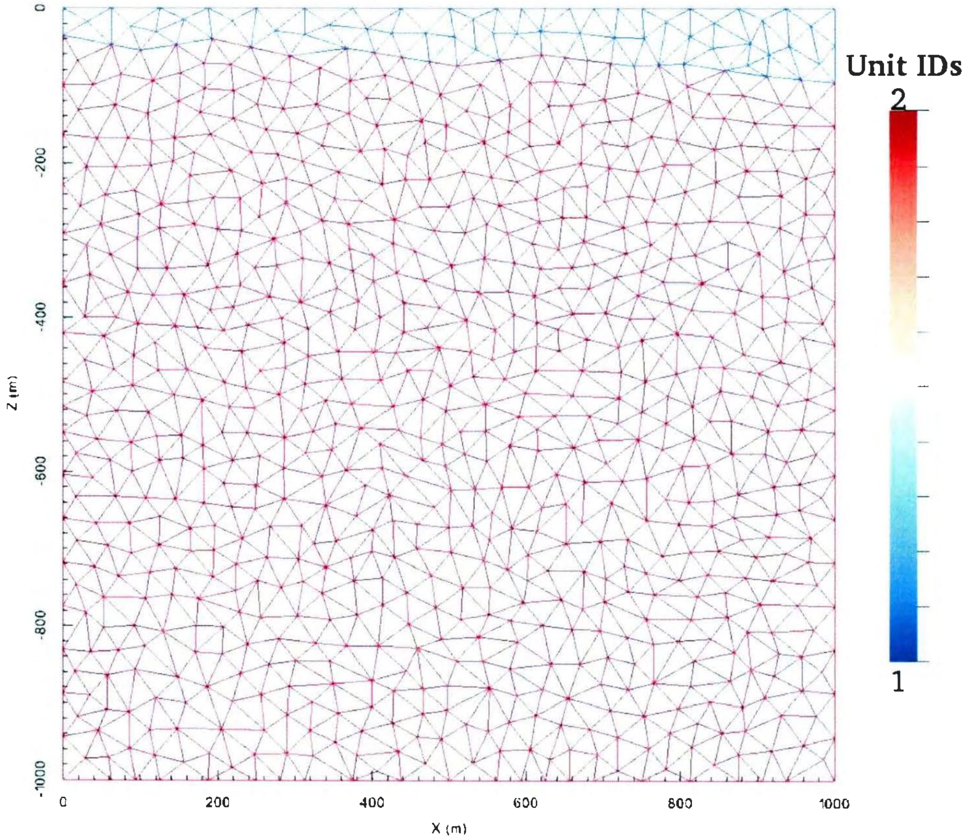

Figure 3.32: Constrained inversion mesh. Assigned slowness range for unit 1 was 0.45-0.55s/km and the assigned slowness range for unit 2 was 0.11-0.25s/km

The new constrained mesh was used as a "reference model" such that the inversion cannot assign the overburden any slowness values outside the range of slowness specified in the reference model. The host rock and orebody were also assigned a slowness range and the inversion cannot resolve the slowness of these units outside the range provided. The constrained inversion result for model 9 with an overburden is shown in figure 3.33. The result shows the overburden is well resolved from x=0m to x=1000m, and it is can be completely distinguished from the geology below it. Also, in comparison to the unconstrained inversion result (figure 3.30), the position of the orebody was better localized in the constrained inversion result.

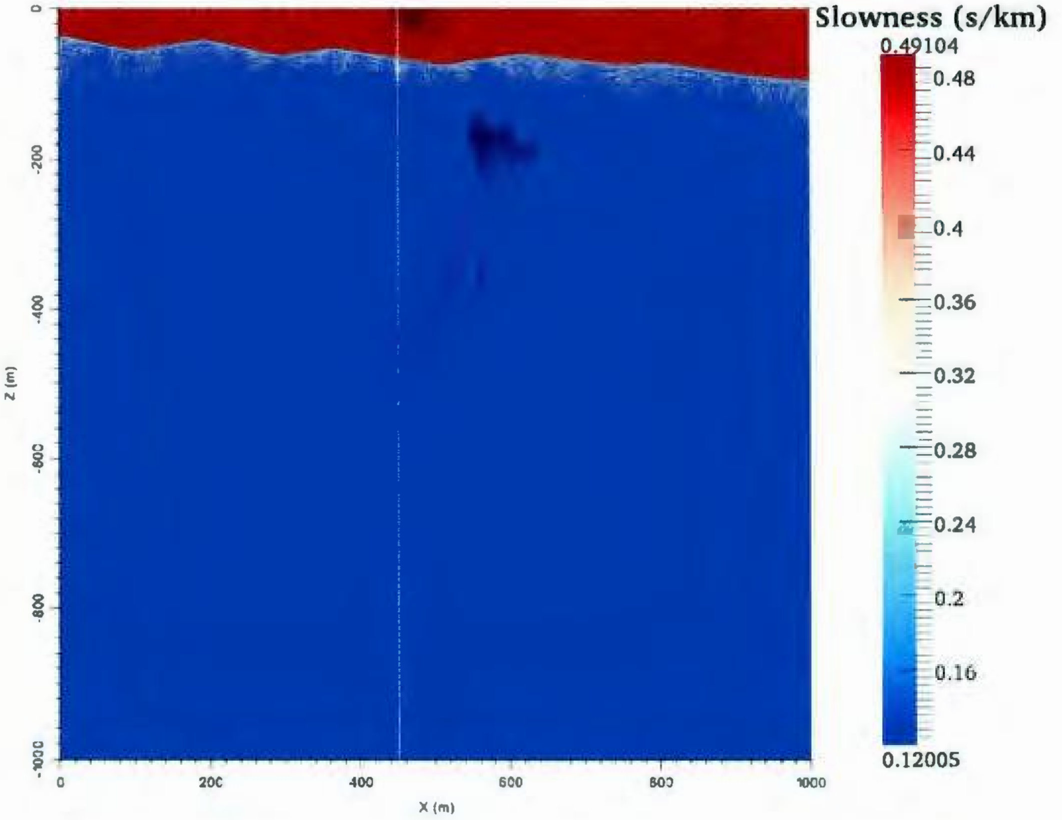

Figure 3.33: Constrained inversion slowness tomogram for model 9.1. The vertical bar on the right shows the slowness scale for the tomogram.

To better see the slowness changes in the region below the overburden layer in the tomograms, the color scale of the results were clipped at 0.136s/km and 0.222s/km. With the adjusted scale, the unconstrained result, seen in figure 3.34, shows that a noticeable amount of slowness from the overburden is distributed into the host rock and some of the orebody. However, when the constrained inversion tomogram is plotted with the adjusted scale (figure 3.35), large smearing out of the overburden slowness is not observed. As seen here, most of the overburden slowness is localized within the overburden. Constraining the overburden slowness improves the slowness resolution of the tomogram in regions below the overburden.

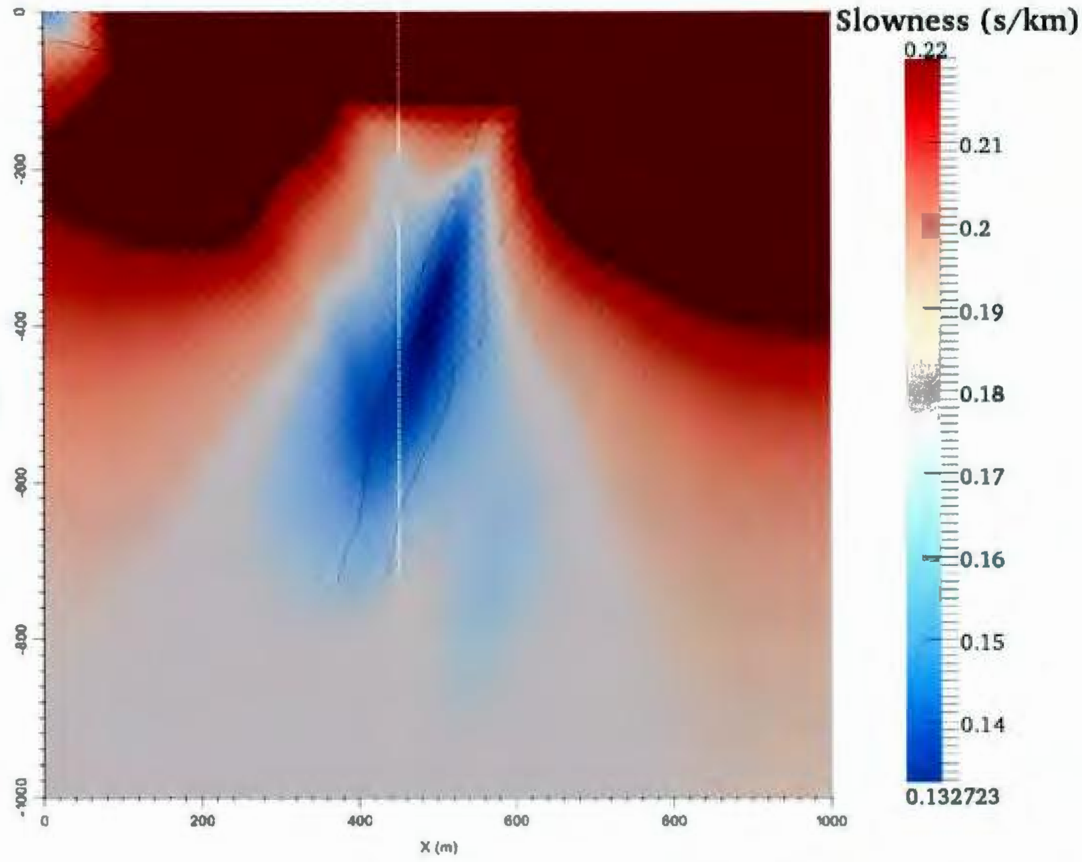

Figure 3.34: Inversion tomogram for model 9.1. Unconstrained inversion result with slowness scale clipped at 0.132s/km and 0.22s/km

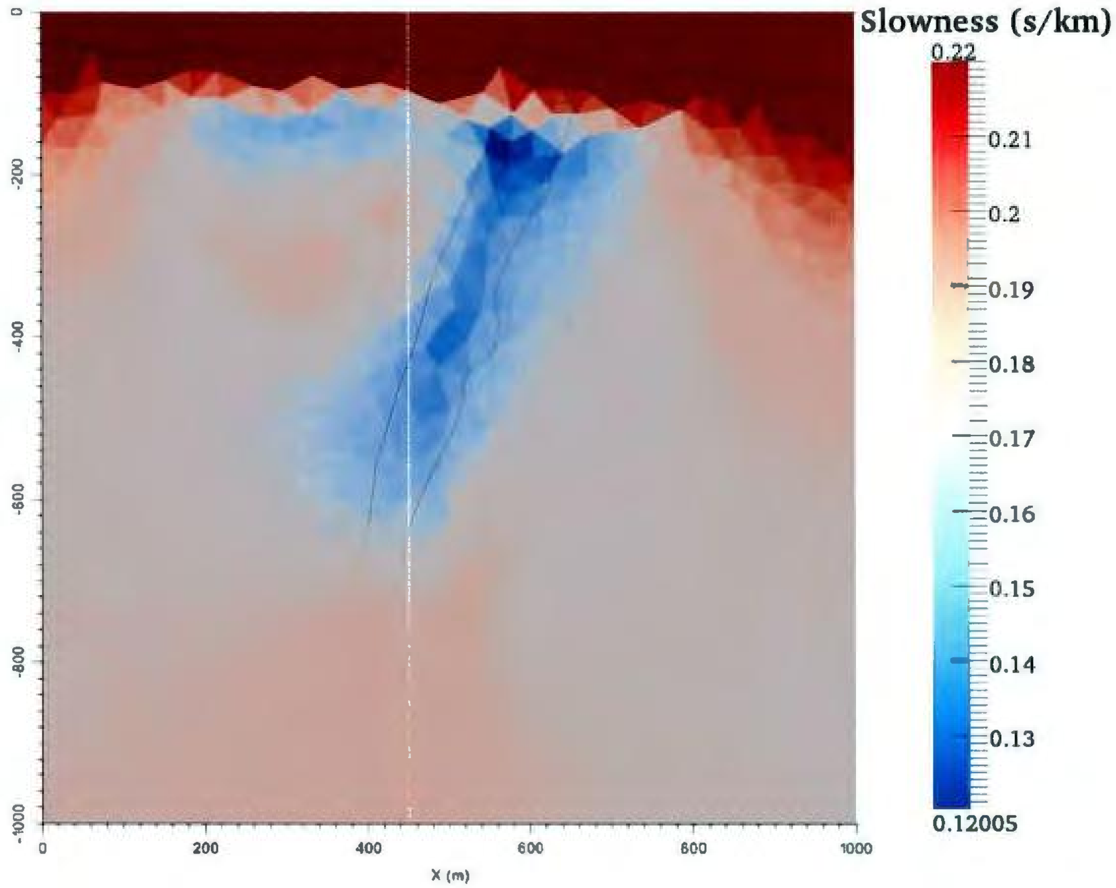

Figure 3.35: Inversion tomogram for model 9.1. Constrained inversion result with slowness scale clipped at 0.132s/km and 0.22s/km

The residual travel-time plot for the constrained inversion, shown in figure 3.36, displays similar trends to the unconstrained inversion residual plot, shown in figure 3.31. A similar trend of high positive residual travel-times at receiver depths of 50-100m for the far-offset shots of the model was observed. These are likely as a result of the smearing of the overburden slowness to cells at those depths. The high slowness values here will make the predicted travel-times at those depths arrive later than the observed travel-times. A similar trend also noticed in the plots is the presence of high negative residual between sources close to the borehole and receivers close to the surface. As seen in the tomogram, the slowness values in the region between sources close to the borehole and receivers close to the surface are slower than the values in the true slowness values. This causes higher predicted than observed travel-times between those source-receiver pairs.

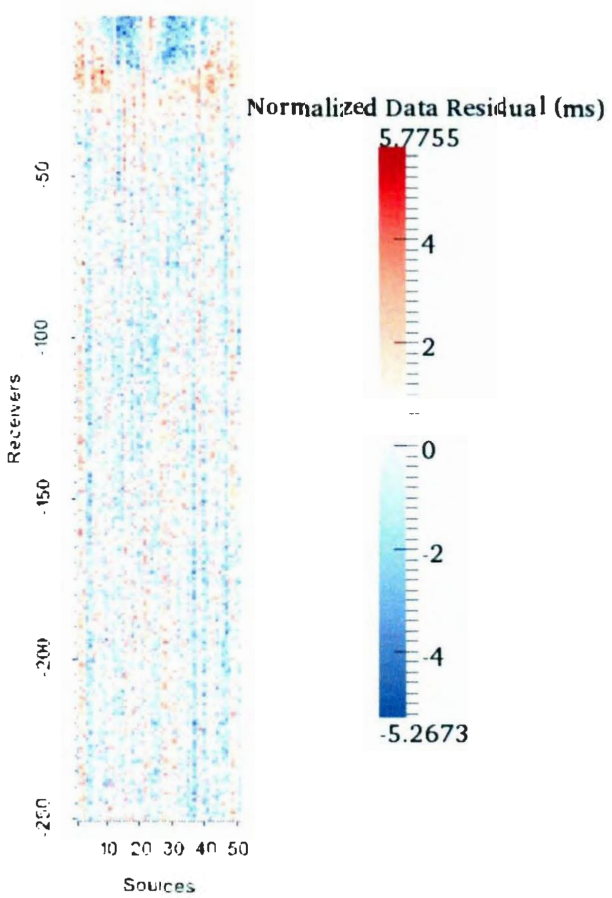

Figure 3.36: Residual travel-time plot for model 9.1 using constrained inversion.

3.3.2a: Model 10.0

The model, shown in figure 3.37, was designed to test the ability to resolve horizontal to sub-horizontal structures in the subsurface. The geology for this model resembles an intrusive sill structure with slowness values of 0.143s/km for the orebody, 0.179s/km for the host rock and 0.500s/km for the overburden (Sheriff and Geldart, 1995). The dimensions of the model are 1000m wide and 1000m deep. 51shots with a peak frequency of 60Hz (Wardell, 1970) were taken at 20m intervals. 1000 receivers at 1m intervals were used to record travel-times in the borehole located at 550m.

To perform the first travel-time inversion, only travel-time data from the borehole at x=550 is used. The data was decimated by using every fourth travel-time picked. Thus, a receiver spacing 4m and a total of 250 travel-times per shot were used to perform the inversion. Random Gaussian noise with a mean of zero and a standard deviation of 2ms was also added.

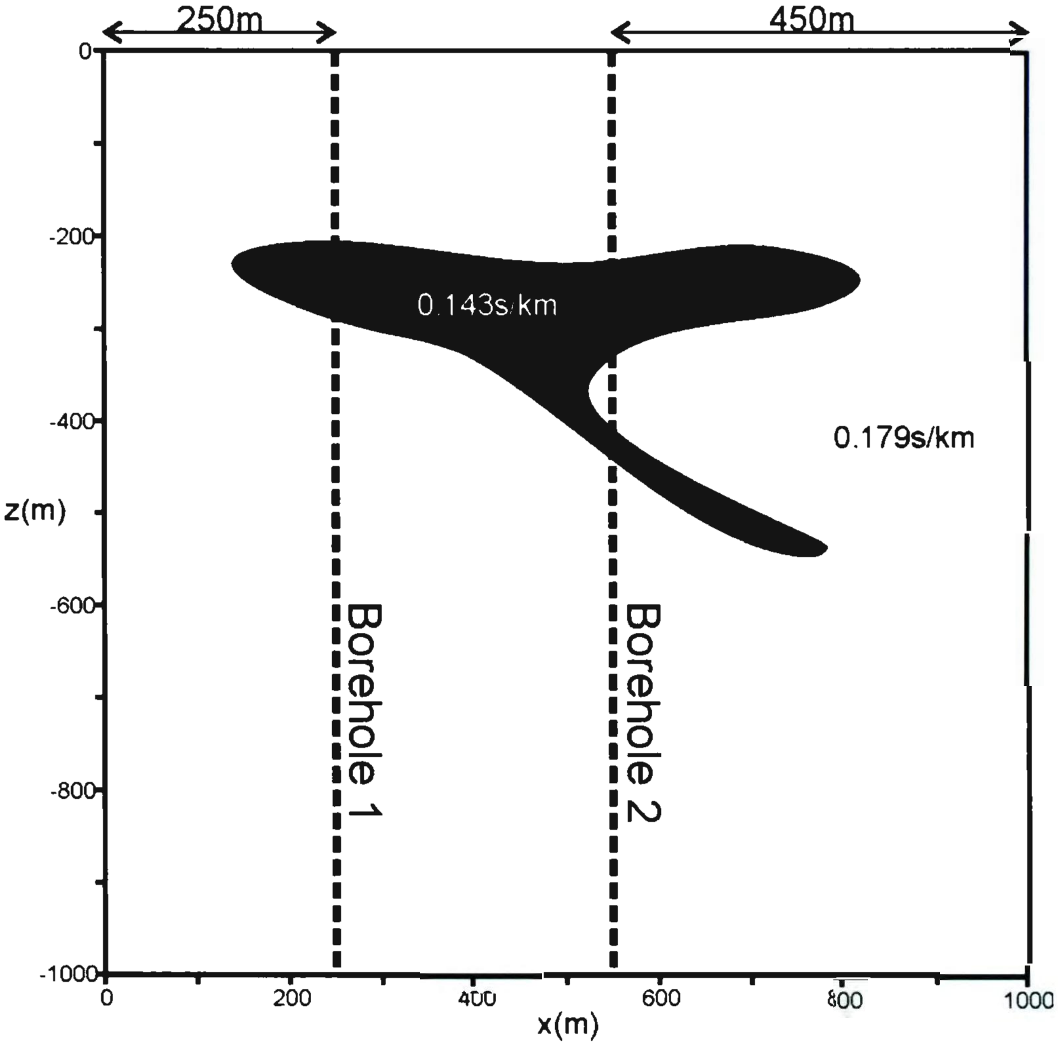

Figure 3.37: True model diagram for model 10.0. The locations of the receiver boreholes are shown.

The inversion tomogram for model 10 with no overburden is shown in figure 3.38. As is seen in the result, the inversion resolved a large portion of the orebody up to about 250m on either side of the borehole. The tips of the orebody were poorly localized by the inversion because they were distorted and skewed in the direction of the predominant ray propagation.

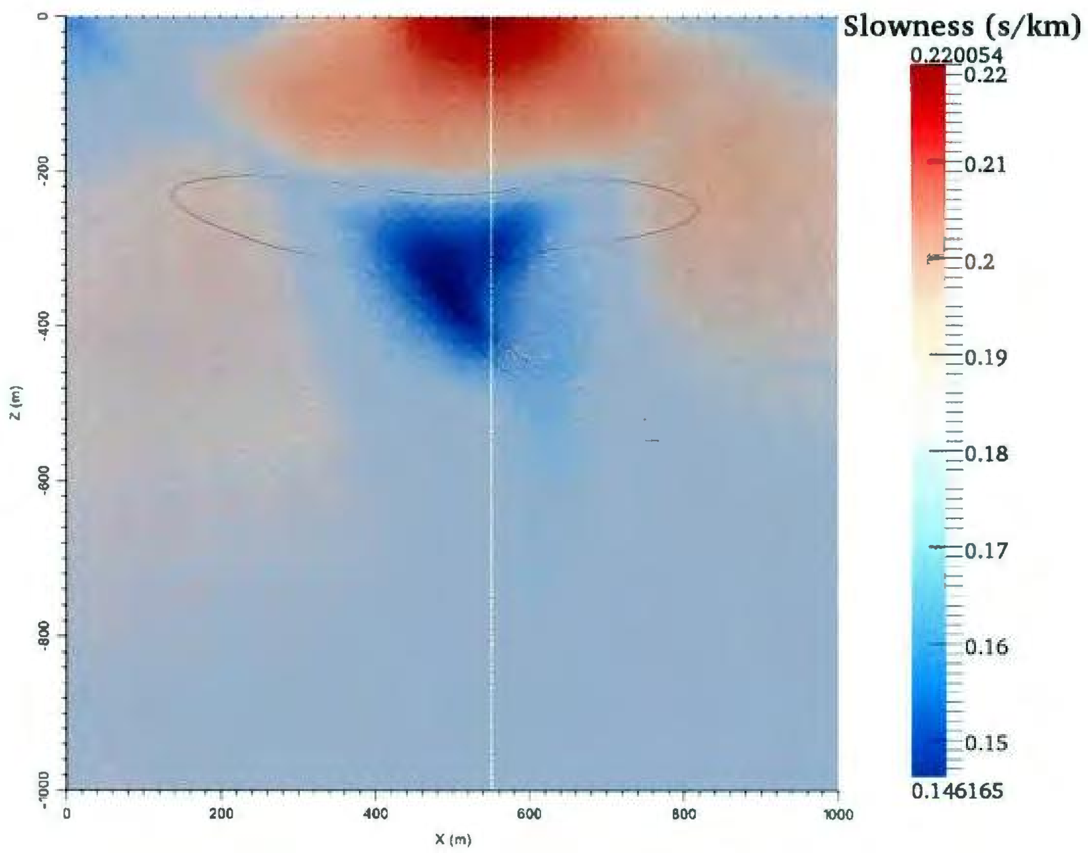

Figure 3.38: Slowness tomogram for model 10.0. The vertical bar on the right shows the slowness scale for the tomogram.

3.3.2b: Model 10.1

Model 10 with an overburden added can be seen in figure 3.39. The model was also designed to test the inversion's ability to resolve sub-horizontal features below an overburden layer. The dimensions of the model are 1000m wide and 1000m deep. 51 shots with a peak frequency of 60Hz (Wardell, 1970) were taken at 20m intervals. 1000 receivers at 1m intervals were used to record travel-times in the 2 boreholes located at 250m and 550m.

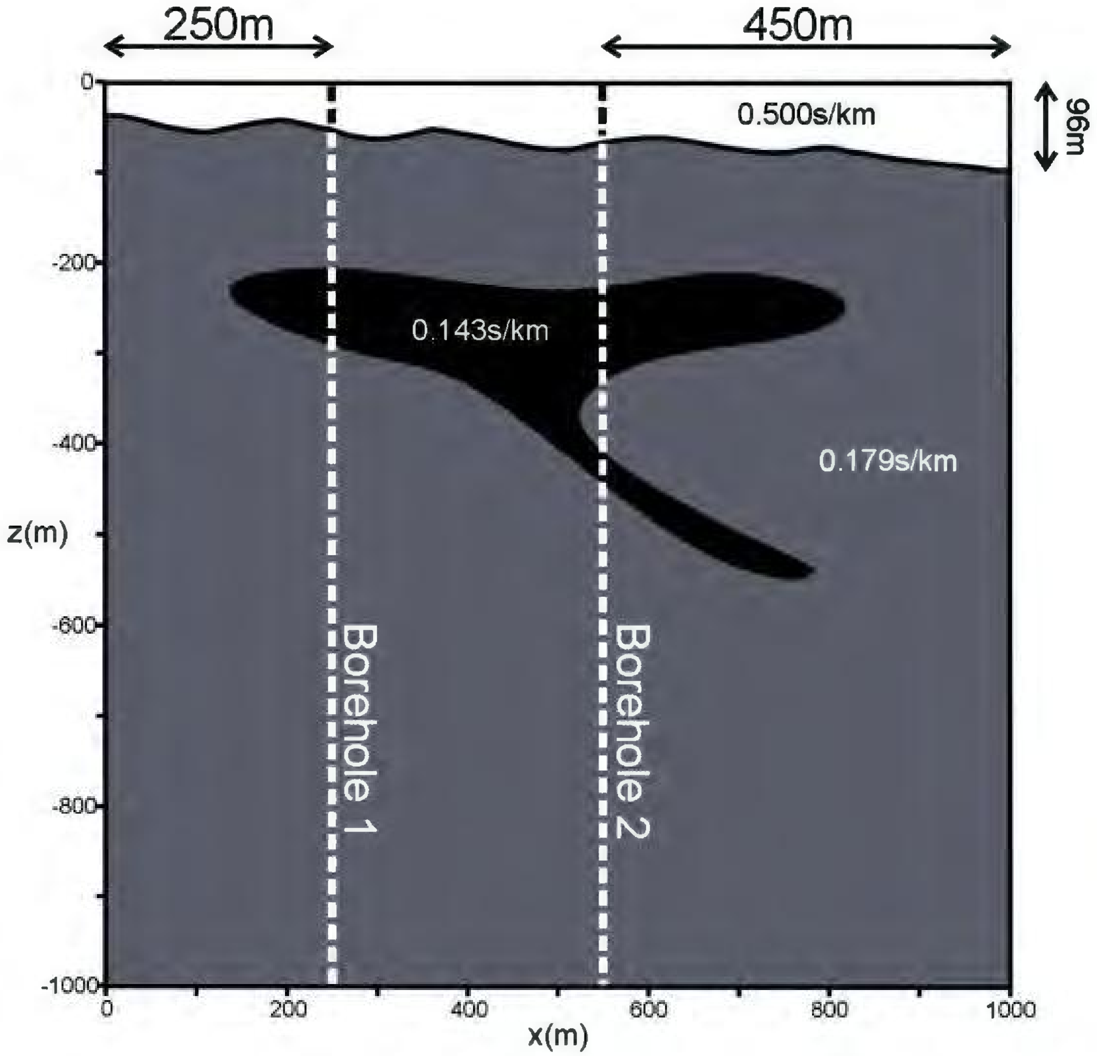

Figure 3.39: True model for model 10.1. The same model as model 10.0 but an overburden is included.

To perform both the unconstrained and constrained inversion on model 10 with an overburden, only travel-time data from the borehole at x=550m is used. The data was decimated by using every fourth travel-time picked. Thus, a receiver spacing 4m and a total of 250 travel-times per shot were used to perform the inversion. Random Gaussian noise with a mean of zero and a standard deviation of 2ms was also added.

The unconstrained inversion result for model 10 with an overburden is shown in figure 3.40, while the constrained inversion result is shown in figure 3.41. In the unconstrained inversion result, it is observed that the overburden is resolved and vertically constrained at about 200m on either side of the borehole. However, at offsets greater than 200m from the borehole, the overburden and the host rock below it cannot be distinguished. In contrast, in the constrained inversion result, the overburden is vertically well localized across the entire survey area.

To better see the slowness changes in the region below the overburden layer in the tomograms, the color scale of the results were clipped at 0.136s/km and 0.222s/km. The rescaled slowness tomograms from unconstrained and constrained inversion are shown in figure 3.42 and 3.43, respectively. In the unconstrained result, it is observed that the orebody is unresolved when it is further than 100m away from either side of the borehole. After the 100m distance from the borehole, the orebody cannot be distinguished from the host rock. The slowness in the region is resolved to be higher than the orebody slowness and this is likely a result of slowness values from the overburden being smeared out into the region. However, in the constrained inversion result, it is observed that most of the orebody was resolved, and it is a significantly improved result compared to the unconstrained inversion. The constraints added to the inversion mesh improve the resolution of the subsurface by limiting the overburden slowness into the overburden layer alone, thereby allowing the inversion to properly resolve and distribute the slowness below the overburden.

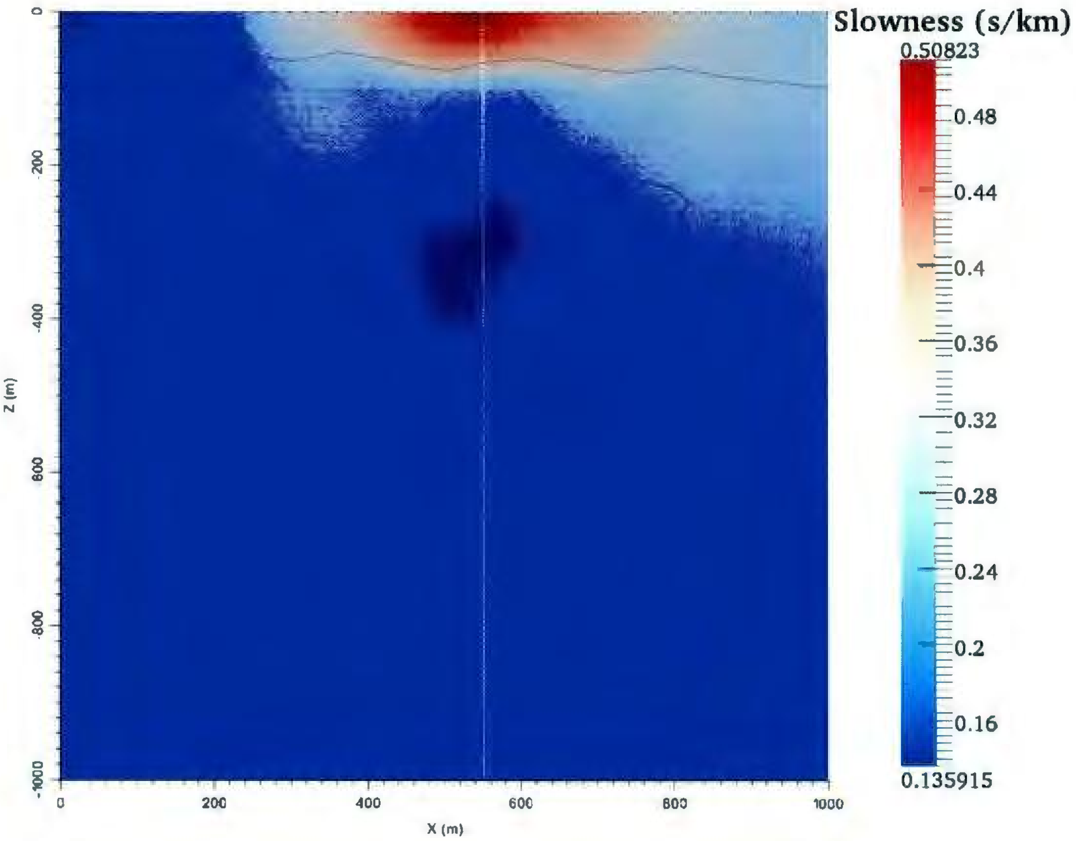

Figure 3.40: Unconstrained inversion slowness tomogram for model 10.1 using only borehole 2. The vertical bar on the right shows the slowness scale for the tomogram.

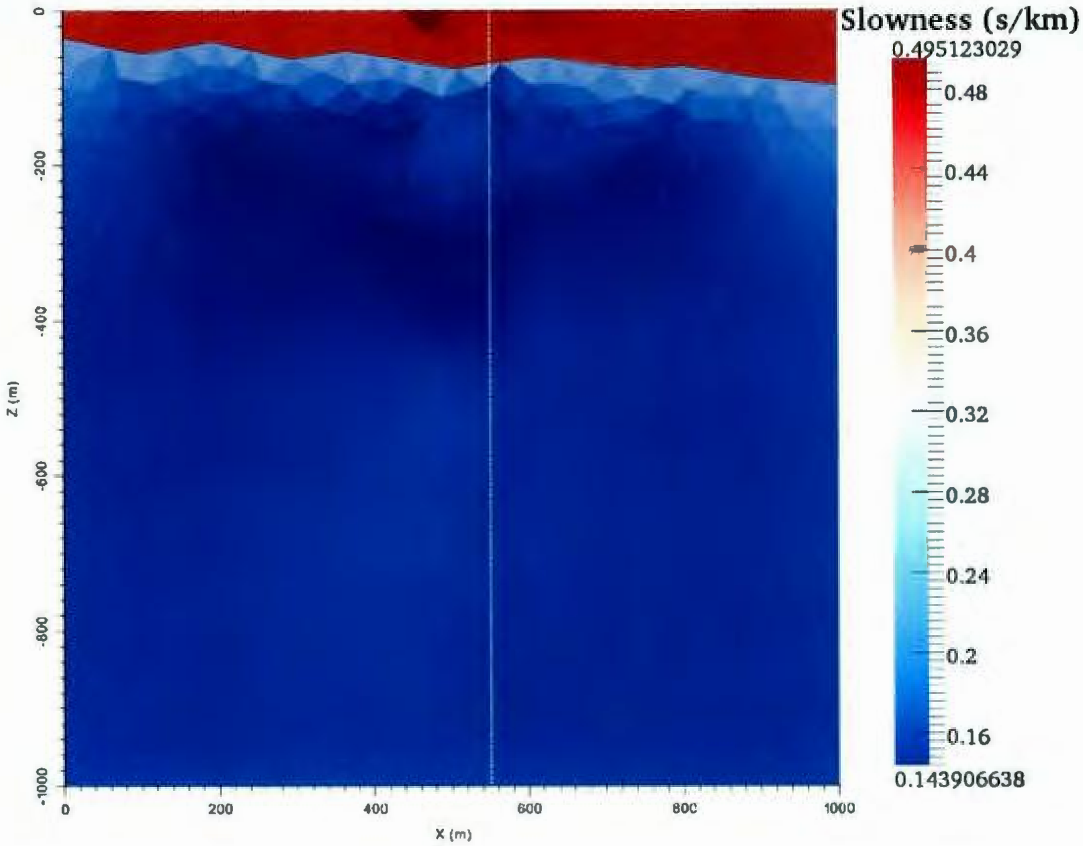

Figure 3.41: Constrained inversion slowness tomogram for model 10.1 using only borehole 2. The vertical bar on the right shows the slowness scale for the tomogram.

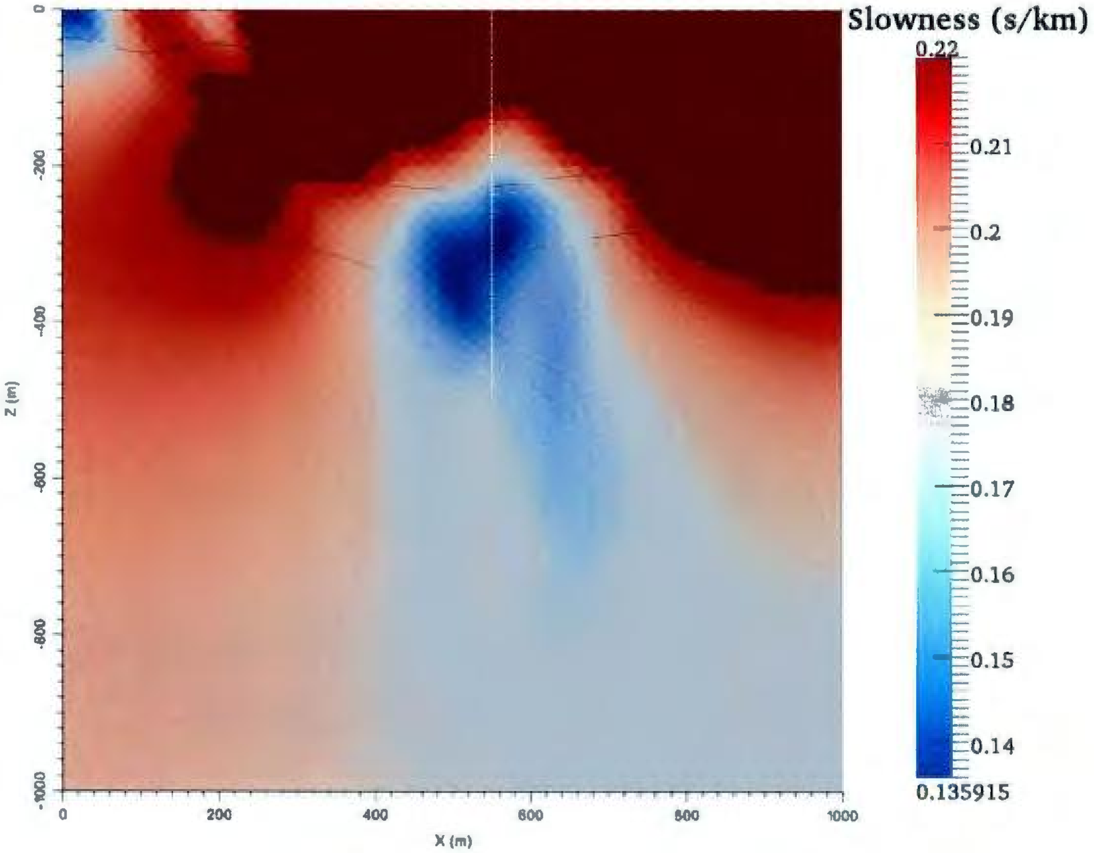

Figure 3.42: Slowness tomogram for model 10.1 using borehole 2 only. Unconstrained inversion result with slowness scale clipped at 0.1359s/km and 0.22s/km.

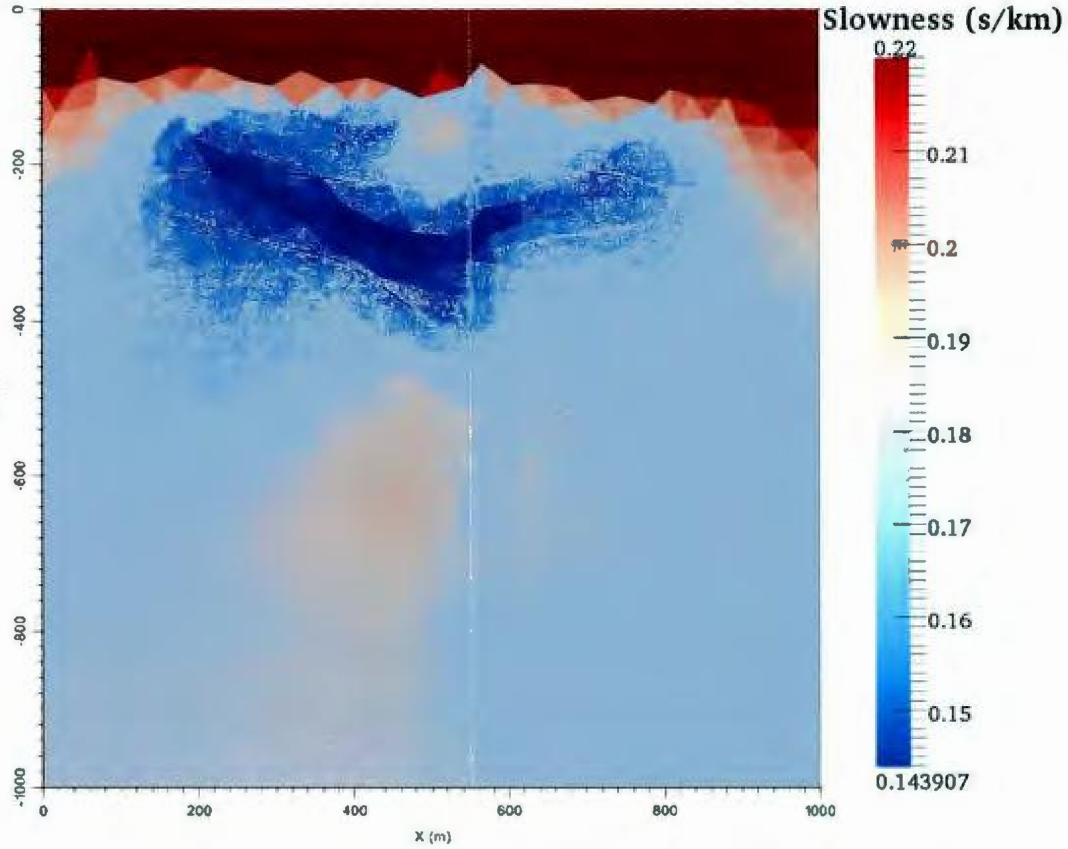

Figure 3.43: Slowness tomogram for model 10.1 using borehole 2 only. Constrained inversion result with slowness scale clipped at 0.1439s/km and 0.22s/km

3.3.2c: Model 10.1

Although the borehole at 550m reproduces the orebody quite well (figure 3.43), the left end of the sub-horizontal orebody, at around x=200m and z=200m, is noticeably slanted at an angle that is more vertical than it is in the true model. To better resolve the orebody in this area, data from the borehole at 250m was added. The use of the two boreholes provides an increase in the variety of ray angle coverage sampling the orebody. The data was decimated by using every eighth travel-time picked in each borehole. Thus, performing the inversion used a receiver spacing 8m, a total of 125 travel-times per borehole and 250 travel-times per shot. Random Gaussian noise with a mean of zero and a standard deviation of 2ms was also added.

Figure 3.44 shows the result of a constrained travel-time inversion of model 10 using both boreholes at 250m and 550m. Based on the result from using the 2 boreholes, the orebody was better resolved and localization was improved on the left side of the orebody.

The residual plot for the inversion done here can be found in the appendix A. The plots did not show any new trend that was not already observed in model 9.

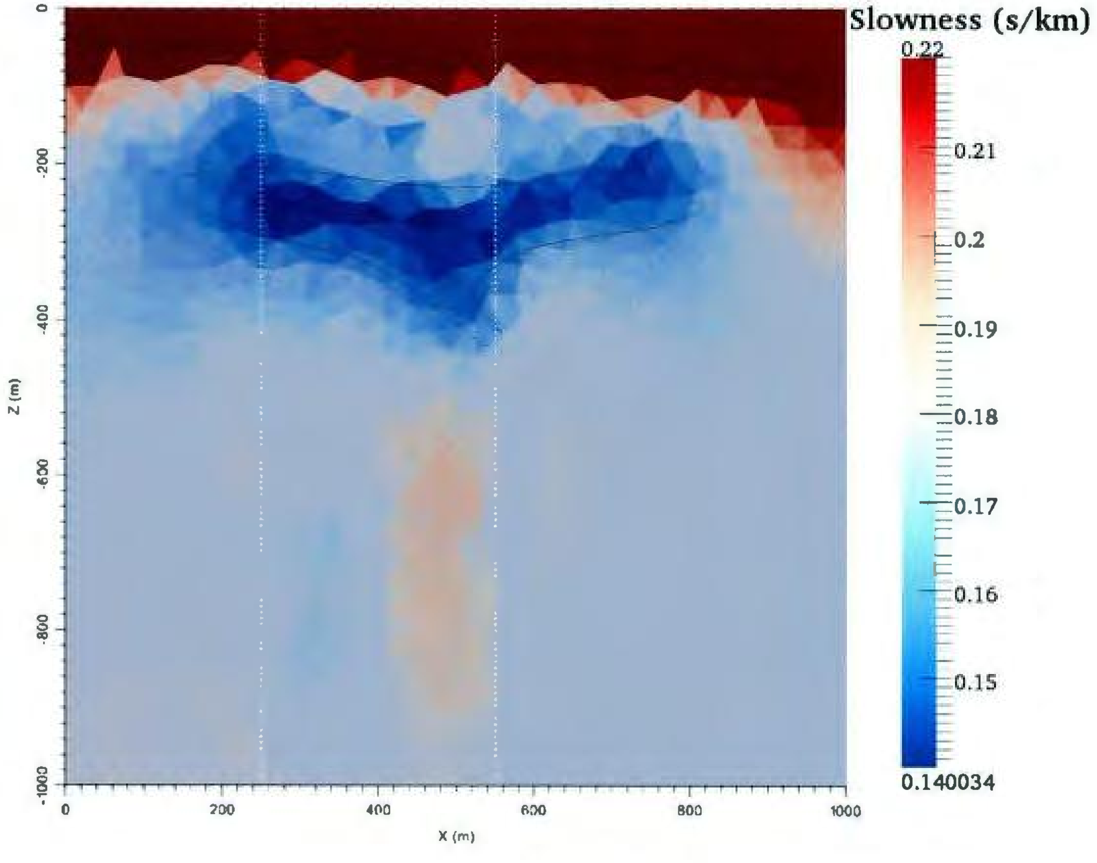

Figure 3.44: Inversion tomogram for model 10.1 using boreholes 1 and 2. Constrained inversion result with upper slowness clipped at 0.1400s/km and 0.22s/km. The vertical bar on the right shows the slowness scale for the tomogram.

3.3.3: Summary

Based on the results from models 9 and 10, the presence of a low-velocity layer significantly reduces the ability of the inversion to resolve geology farther away from the borehole. This is due to significant distribution of the slowness of the low-velocity layer into the geology below it.

The use of a constrained inversion mesh in models 9 and 10 improves the inversion results by limiting the slowness of the overburden to the layer alone, thereby allowing appropriate slowness values to be calculated and distributed in the subsurface.

3.4: Conclusions

Based on the geometry, dominant source frequency and inversion method used, the approximate depth attained for resolution of objects was 40% (or 50-60% if the borehole penetrates the anomalous body) the depth of the borehole used. In addition, the resolution of a model in the subsurface is best in the direction perpendicular to the raypaths and poor in the direction in which the rays travel. Therefore, by sampling the geology in the subsurface at a variety of angles, there is an increased chance of resolution and localization of objects. The resolution of a region in the subsurface depends on independent sampling of that region by many rays from as many different angles as possible (Rogers et al., 1987).

Furthermore, in the unconstrained inversion results for models 9 and 10, the resolution of the subsurface is limited to close proximity of the borehole when a low-velocity layer is present. Therefore, when an unconstrained inversion was performed, only structures around the borehole were resolved. To improve the subsurface resolution when an overburden is present, a constrained mesh was used to perform the inversion. The constrained mesh improved the resolution in the subsurface by limiting most of the slowness of the low-velocity layer to within layer itself. As seen in the constrained inversion results of models 9 and 10, using a constrained mesh allowed the inversion to calculate appropriate slowness values for the layer beneath the overburden.

Chapter 4 : Inversion of Real Data

4.0: Introduction

In fall 2010, surface-to-borehole seismic data was collected in the Reid Brook area of Voisey's Bay (figure 4.1), Labrador. As part of the surface-to-borehole tomography study, the seismic data travel-times collected there were inverted and analysed. The slowness tomogram generated from the inversion of the field data is compared to a 2D seismic reflection profile of the same area.

Figure 4.1: The location of Voisey's Bay, Labrador, Canada.

The use of tomography is a suitable method of imaging the Reid Brook zone, because a potential for strong velocity contrast exists between the rocks in the area.

Although strong velocity contrasts are present, there is no previous knowledge as to whether such contrast exists in the section of the subsurface where data were collected.

4.1: Rock properties and geology of the Reid Brook Area.

The Voisey's Bay nickel-copper-cobalt deposit is located in Eastern Labrador. The deposits occur within troctolites and olivine gabbros of the 1.34 Ga Voisey's Bay intrusion. The deposit consists of four mineralized zones (Discovery Hill, Ovoid, Eastern Deeps and Reid Brook) which contain dipping bodies within a feeder dyke (Kerr, 2008).

The Reid Brook zone consists of disseminated to semi-massive sulphides in a south-dipping segment of the Ovoid conduit. The massive sulphides in this zone occur as 200-400m wide lenses, which crosscut the disseminated sulphides within the conduit (Evans-Lamswood, 2000). The rock lithologies in the zone comprise of massive sulphide, gneiss, troctolite, and to a lesser degree breccia and granites. The gneiss, termed the Tasiuyak gneiss, is the host rock in the area. Troctolite rocks present in the Reid Brook zone are the chamber rocks which host the deposits in the area. The massive sulphide deposit in the area consists of minerals such as pyrite, pyrrhotite and chalcopyrite. The average values of rock velocities in the region are 5.60+/-0.28 km/s (0.179s/km) for the gneiss, 6.0+/-0.29 km/s (0.167s/km) for the troctolite and 4.70+/-0.33 (0.213s/km) for the massive sulphide (Duff, 2007).

4.2: Data Collection and Processing

Using a swept impact seismic source, a total of 20 shots at 20m spacing were taken for this experiment. A geophone placed next to the source was used to record the source signal generated and the phase of the source produced was determined to be a mixed phase signal. Each shot was recorded at 240 locations (272m-750m depth) in the subsurface, with the receivers in the borehole spaced at 2m intervals. The data was recorded using a 60m long hydrophone cable that consisted of 30 channels spaced at 2m. Each shot was repeated multiple times with the receiver array at different depths to assemble 240-channel composite shot gathers. The geometry of the survey is shown in figure 4.2. As seen in the figure, the shot locations do not fall in a straight line. However, for the ease of interpretation in this thesis, the survey line is approximated to be straight and hence a 2D survey is assumed. The first shot location for this survey was approximately 48m away from the borehole while the last shot was located 370m from the borehole.

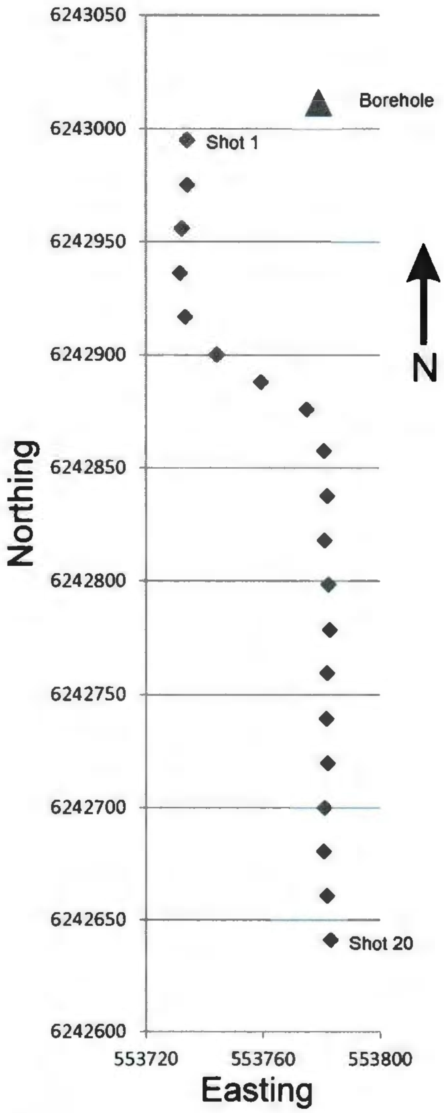

Figure 4.2: Location of survey borehole and shot points.

In the recorded seismic shot records, strong high amplitude tube waves traveling through the borehole column were present in the data. Therefore, before travel-time picks were made, data processing had to be performed to reduce the presence of the tube waves.

After geometry had been assigned to the data, a zero-phase Ormsby bandpass filter with gate 40-45-100-150Hz was applied to the data. The filter reduced any low frequency noise that makes picking inaccurate. A 5-trace median mixing was also applied on the data. The trace mix reduces the fluctuations of travel-time onset from one trace to another; it also suppresses incoherent events such as random noise.

Figure 4.3 shows a seismic record of shot 13 after processing had been done. As is seen in the figure, complete elimination of the tube waves was difficult despite the data processing. Therefore, in areas where tube waves slightly interfered with the direct p-wave arrivals, travel-times were picked as accurately as possible. In other sections of the data where there is complete tube wave interference, the first arrival times were not picked. This precaution was taken to avoid inverting wrong travel-times along with accurate travel-time data.

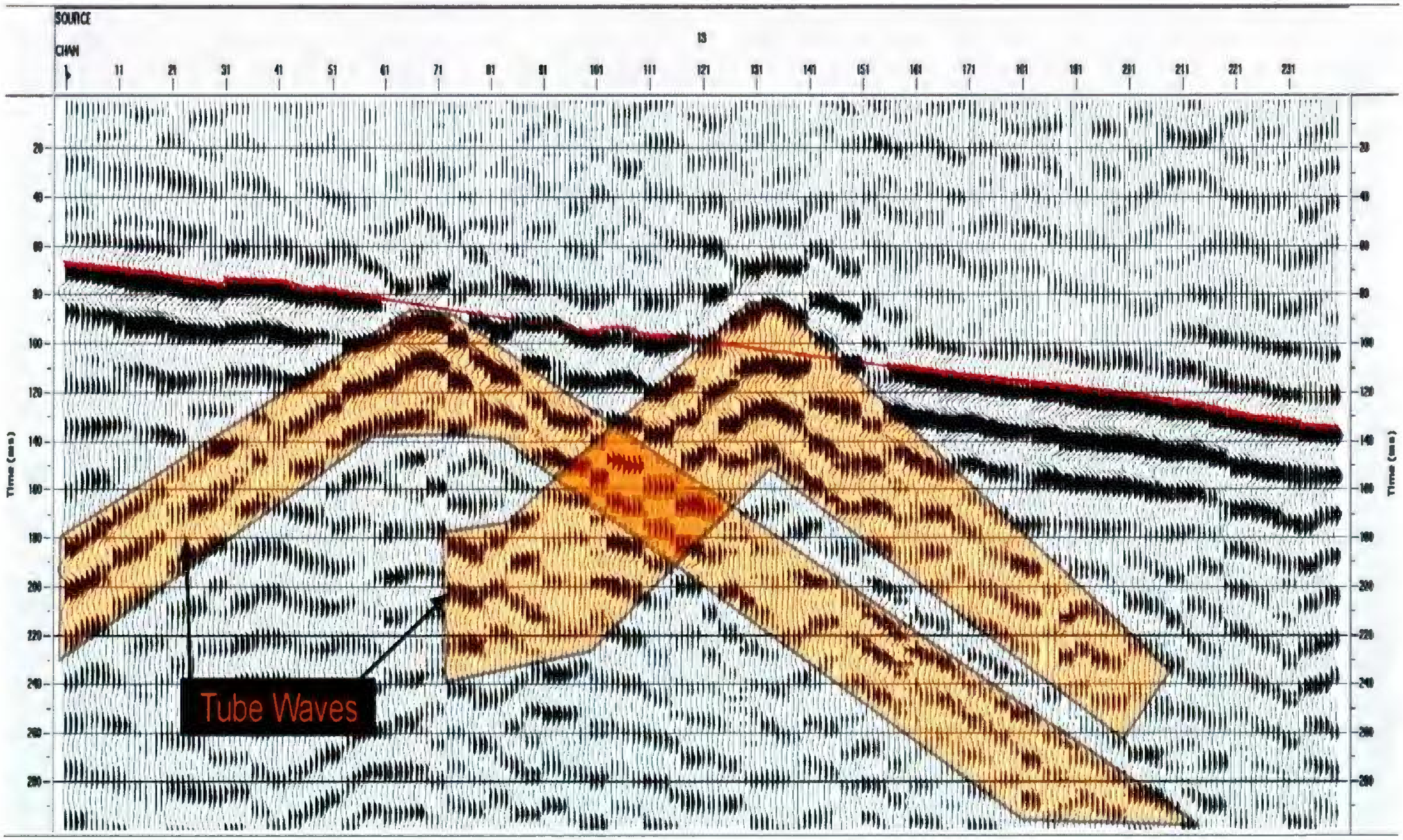

Figure 4.3: Field data shot record of shot #13. Small red crosses shows the first-arrival travel-time picks, red line indicates no picks were made and the orange polygons emphasize the tube waves which interfere with some first arrival picks.

4.3: Inversion of field data and inversion of test experiment

4.3.1: Synthetic data inversion

In the synthetic model inversions performed in Chapter 3, the depth of the first receiver used to perform the inversion was at 0m (or 2m). However, in the field study, the depth location of the first recorded travel-time was at 272m. Thus, an understanding of any effects that lack of receivers in the top 271m has on the inversion result had to be developed. To examine the issue, model 9, shown in figure 4.4, was inverted again. The survey parameters include 51shots taken at 20m intervals from x=0m to x=1000m; the receiver borehole is located at x=451m and 1000 receivers was used to record in the borehole. However, receivers between depths of 0m and 300m were removed from the data and only travel-times recorded in the receivers from z=301m to z=1000m are used to perform the inversion. The inversion was performed using a mesh that constrained the structure and slowness of the overburden layer. The mesh and other inversion parameters used here are identical to that used to perform the inversion of model 9 in chapter 3.

The constrained inversion result for model 9 using only travel-times from 301-1000m depth is shown in figure 4.5a. As seen in the figure, despite the use of a constrained inversion mesh, the lack of travel-time information from the top of the borehole reduced the ability of the inversion to properly localize slowness in the tomogram. When compared to the inversion result with travel-times recorded from 0-1000m in the borehole (figure 4.5b), it is observed that the high slowness region below the overburden is larger in figure 4.5a. Sub-horizontal traveling rays provide inversions with vertical resolution (McMechan, 1983). Therefore, the lack of recorded horizontal rays in the inversion likely explains why the slowness of the overburden was distributed into the region just below it. In figure 4.5a, the orebody is also poorly resolved when compared to the inversion result in figure 4.5b. The poor distribution of slowness in the near-surface directly affects distribution of slowness deeper in the subsurface. Due to the large distribution of the high slowness values in the immediate region below the overburden, the inversion had to assign deeper sections of the subsurface lower slowness values than normal, in order to distribute slowness values that add up to the proper travel-time values.

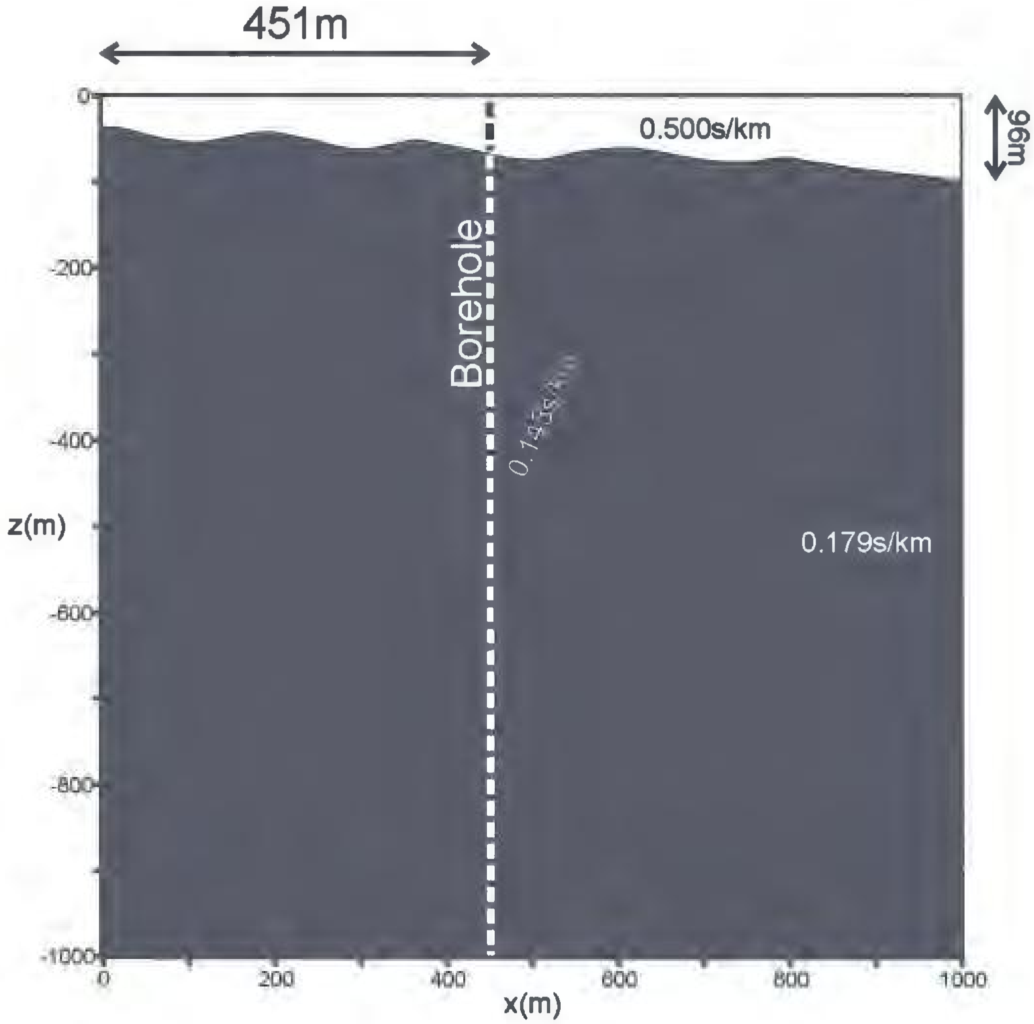

Figure 4.4: True geologic model for model 9

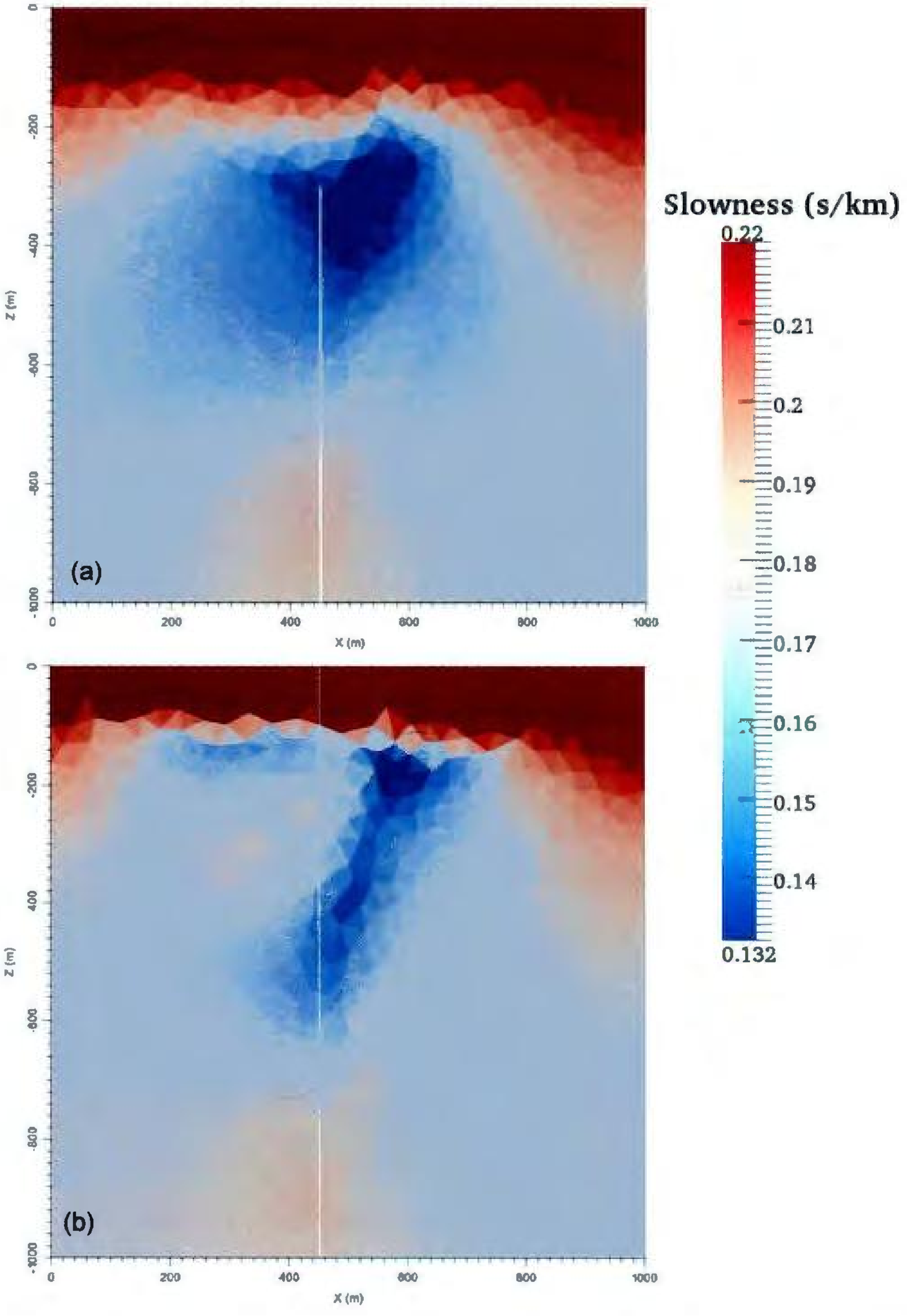

Figure 4.5: Inversion of model 9. (a) first receiver location at a depth of 301m and (b)first receiver location at 0m depth. Receiver range is indicated by the white borehole.

4.3.2: Field data inversion

Based on the synthetic model result above, it was discovered that due to the lack of recorded travel-times in the top 300m of the subsurface, the data lacked sub-horizontal traveling rays that would have helped in better localization of the slowness of the low-velocity zone to the layer itself. As a result, the region below the overburden was poorly resolved and the rest of the subsurface was poorly resolved as well. With this knowledge, it is unlikely that the constrained inversion result of the field data will produce a well resolved tomogram because of the lack of recorded travel-times in the top 271m.

For inversion purposes, the field data travel-times were inverted with added noised based on a mean of 0ms and a standard deviation of 3ms. The constrained inversion mesh shown in figure 4.6 was used to perform the inversion. In the mesh, the constrained overburden layer thickens gradually away from the receiver borehole. Based on information from an available refraction survey, the cells in the overburden were assigned slowness value bounds of 0.40s/km minimum and a maximum slowness of 0.66s/km. The overburden depths used for the mesh were derived from 2 boreholes located at the beginning and end of the survey line; while the depths between the 2 boreholes were interpolated as a gradual slope between the 2 boreholes.

Below the overburden, a borehole sonic log which measured the slowness (minimum 0.134s/km and maximum 0.232s/km) of in-situ rocks around the borehole was available. By using slowness information derived from the sonic log as a guide, the slowness bounds for the cells below the overburden was set to a minimum of 0.130s/km and a maximum of 0.25s/km.

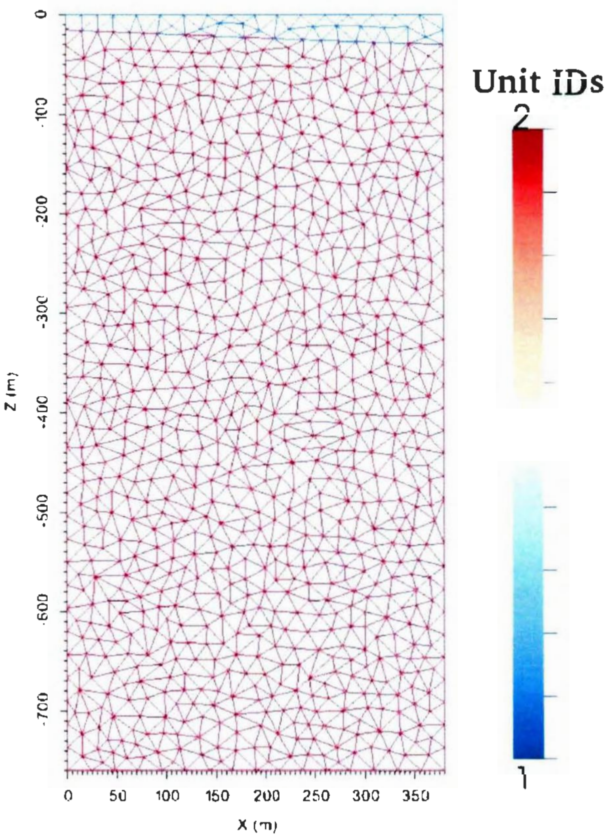

Figure 4.6: Constrained inversion mesh used for inverting the field data. Unit 1 (overburden) slowness scale was restricted between 0.40s/km and 0.66s/km, unit 2 had slowness values restricted between 0.13s/km and 0.25s/km

The field data slowness tomogram is shown in figure 4.7. As is seen in the result, there are fluctuations in the slowness values around the borehole. Cells at depths from 100m to 350m show low slowness values of approximately 0.13s/km, cells at depths of 400m to 750m show slowness values of about 0.18-0.19s/km values interrupted by a region of lower slowness of about 0.14s/km between 600m and 700m. Away from the borehole, the slowness fluctuations are resolved perpendicular to the direction in which rays travel from source to receiver.

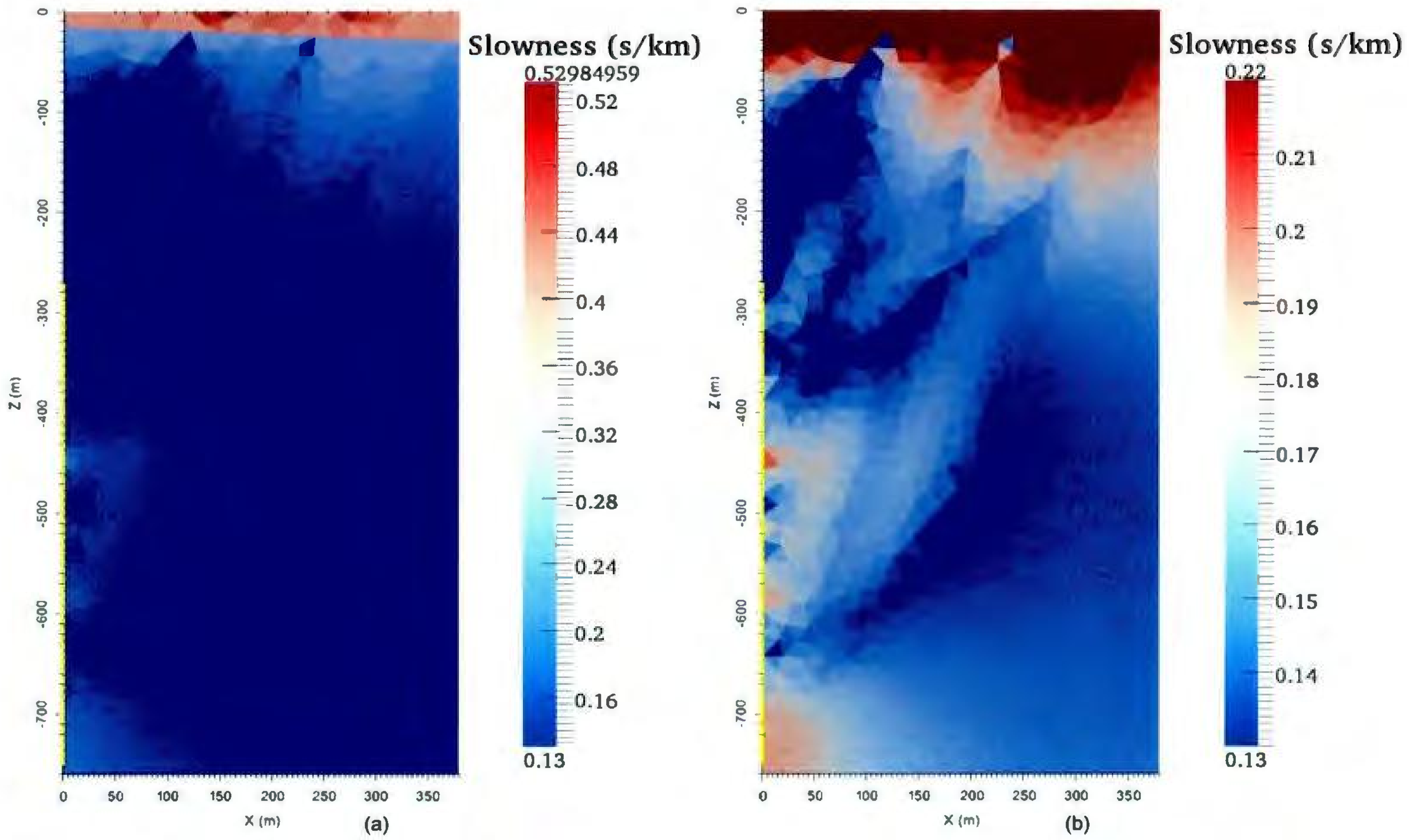

Figure 4.7: Slowness tomogram for Reid Brook area field data. Image on the right is the same tomogram as the image on the left but the slowness scale is clipped at 0.22s/km to emphasize the slowness values/structures below the overburden. General location of receivers indicated by dashed yellow line.

4.4: Comparison of inversion result with 2-D seismic line and borehole log

Conformities between datasets increase the confidence level of a result, therefore the field data inversion result was compared with a 2-D reflection seismogram of the same area, and a sonic (slowness) log of the receiver borehole was placed adjacent to the image.

Figure 4.8 shows the comparison of the tomogram result, 2D seismogram and the log plot. As seen in the figure, there is no obvious correlation between the borehole log and the tomogram but there appears to be some correlation between the tomogram and the seismogram. In the region of approximate ray coverage (above the dashed green line), the event marked (1) in the figure appears to be conformable but there is no certainty to the true existence or if they are just artefacts in both the seismogram and the tomogram. In the region with approximately no ray coverage (below the dashed green line), the event marked (2) appears to be conformable between the seismic and the tomogram but as with the first event (1) there is no true knowledge of the existence of that event in the subsurface.

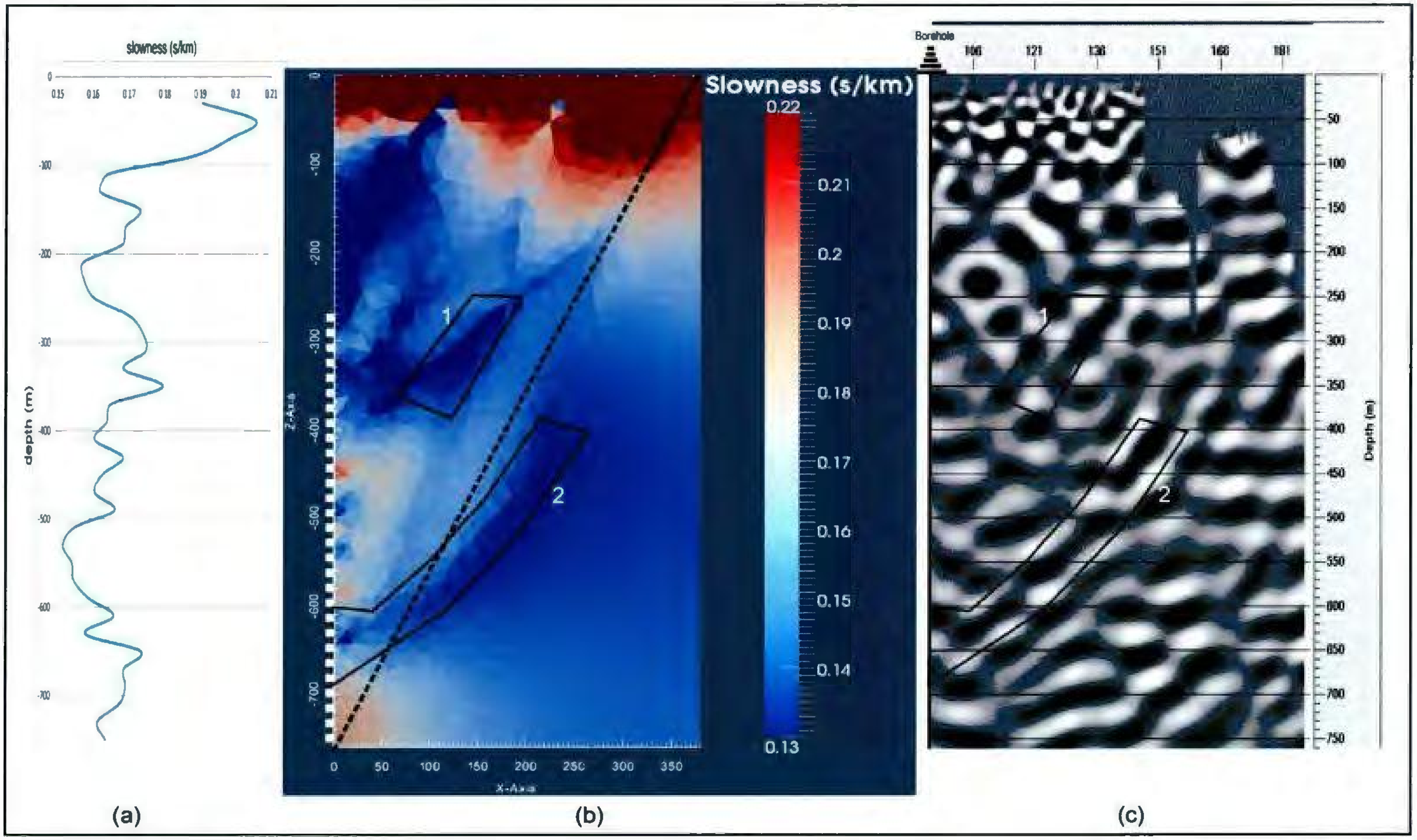

Figure 4.8: (a) Sonic log (in slowness) of borehole, (b) slowness tomogram of Reid Brook field data and(c) 2D seismic line of Reid Brook area. Dashed green line on tomogram indicates approximate zone of ray coverage. Dashed white line indicates general locations of receiver in borehole.

4.5: Conclusion

From the synthetic modeling test performed in this chapter, it was observed that a lack of recorded travel-time data in the near-surface reduced the resolution of geology in the deeper sections of the subsurface. Travel-times recorded close to the surface provide the inversion with data that can better constrain near-surface vertical resolution. Without the vertical constraints provided by the near-surface data, distribution of slowness in the deeper regions of the subsurface is poorly resolved.

In the field data inversion, the lack of recorded data in the top 271m of the subsurface likely affected the resolution of the tomograms in the regions where data were recorded. However, some of the events in the tomogram were correlated to events in the 2D seismogram. Although these events were correlated, they may be artefacts present in the tomogram and/or seismogram as well. Proper evaluation of the tomogram can only be done with data recorded from 0m to 750m depth in the borehole.

The residual travel-time plots (see appendix A) generated by the inversion of the synthetic and field data did not show any anomaly or trend to indicate any possibility of poor resolution in sections of the subsurface. This is because the inversion was able to generate a model tomogram that fits the observed travel-time data.

Chapter 5 : Discussion

The purpose of this research is to assess the capabilities of surface-to-borehole seismic travel-time tomography as a tool for mineral exploration and resource evaluation. In comparison to the currently preferred geophysical methods such as induced polarization, electrical, electromagnetic and potential field methods, surface-to-borehole tomography offers the potential to image deeper (>500m) in the subsurface and with higher resolution. Despite the potential for deeper subsurface imaging, the method has been relatively unused for mineral exploration purposes.

Assessment of the capabilities of surface-to-borehole tomography was carried out using several checkerboard models and a suite of increasingly realistic geologic models. Acoustic finite-difference modeling was used to generate seismic data for the series of synthetic models. A sum-of-squares minimum-structure inversion approach was then used to perform inversions on first-arrival travel-times. The slowness tomograms and residual travel-times generated were then analysed to evaluate the performance of the inversion.

Based on the acquisition parameters used, the inversion results for the synthetic models show that the surface-to-borehole tomography method has the capability to resolve geological structures of various shapes, orientations, sizes and at various depths. The presence of a near-surface low-velocity zone reduces the ability of the inversion to resolve the subsurface. However, constraining the near-surface based on additional information reduces the effects of the near-surface and resolution is enhanced.

The checkerboard tests were designed to evaluate the resolution of the tomography using the surface-to-borehole geometry. Because of the high degree of velocity heterogeneity present in the checkerboards, they represent a particularly challenging problem for the inversion. In addition to the large velocity contrasts, the 100 m and 250 m checkerboards are sampled by only 1 and 2-3 wavelengths respectively, at the dominant frequency of the seismic data. The results of 100 m (figure 3.16) and 250 m (figure 3.14) checkerboard show that resolution in the tomograms is good down to approximately 30% and 40% of the borehole depth. In the 500 m checkerboard test there is less slowness fluctuation in the model compared to the 100 m and 250 m checkerboards. As a result, the tomogram resolution in the 500 m (figure 3.12) checkerboard test is good down to approximately 50% of the borehole depth. Despite the complexity of the checkerboard tests, vertical and horizontal resolution is good in the well resolved regions of each tomogram. In a real exploration setting, the bodies of interest are more isolated bodies located in a subsurface that is less complex than the checkerboard tests and more similar to the geological model examples performed.

The checkerboard tests and several geological model tests demonstrate that resolution in the tomograms is sensitive to the acquisition geometry used. This sensitivity is comparable to the sensitivity experienced in the cross-hole tomography method. In the cross-hole geometry, the raypaths travel in a predominantly sub-horizontal direction from sources to receivers. Sub-horizontal raypaths produce good vertical resolution, but poor horizontal resolution (McMechan, 1983). McMechan also explained that horizontal resolution is poor because a smoothed slowness distribution fits the observed data equally well as a variety of slowness distributions that contain boundaries.

Similarly, in the surface-to-borehole geometry, the best resolution is obtained in the direction perpendicular to the raypaths, while resolution is poor in the direction parallel to the raypaths. The inversion result of model 9 (figure 3.28) demonstrates a situation whereby the resolution in a tomogram is good in the direction orthogonal to the raypaths. In model 7, when the inversion was performed using only data from borehole 1 (figure 3.19), the unresolved boundaries of the troctolite demonstrates how resolution is poor in the direction parallel to the raypaths. Based on the direction of raypaths in the surface-to-borehole geometry, the examples mentioned illustrate the optimal and least ideal direction of resolution in a tomogram.

Improving the resolution of a region in the subsurface can be done by increasing the range of angles of the rays that sample the region (Kanli et al., 2007). An approach used to increase angular ray coverage in this thesis was the use of multiple boreholes surrounding the region of interest. The inversion result from using two boreholes to invert model 7 (figure 3.21) illustrates how an increased angular sampling of a region can improve the resolution of that region in a tomogram. A combination of surface-to-borehole travel-times along with borehole-to-borehole travel-time data is another approach that can be used to increase the angular ray coverage and resolution of a region on a tomogram. Several authors (Moret et. al., 2006, Rogers et. al., 1987, Kanli et al., 2007, McMechan, 1983) have performed inversion with the combined use of cross-hole and surface-to-borehole data and have successfully demonstrated that the approach increases resolution.

The effect of a near-surface low-velocity layer on the resolution in a tomogram was studied in this dissertation. Near-surface weathering layers are typically characterized by low seismic velocity within the layer and a sharp increase in the velocity at the base of the layer. When unconstrained inversions were performed on examples with an overburden layer present (models 9 and 10), it was demonstrated that the inversion algorithm was unable to localize the overburden slowness to within the overburden region (figures 3.34 and 3.42). The reason is because minimum-structure inversions typically generate slowness boundaries as a transition, and not a sharp boundary. Therefore, the larger the slowness contrast at the boundary, the more smeared out the boundary in the tomogram. In order to reduce the smearing at the boundary between the overburden layer and the underlying geology, a constrained mesh was used to perform the inversion. In the constrained mesh, the structure of the near-surface layer was designed and assigned a slowness range which the inversion had to abide by when inverting travel-time data. In addition, the region below the overburden was assigned a range of slowness values which the inversion algorithm also had to honour when inverting the data. By constraining the inversion with structural and slowness bounds, we reduced the number of ways slowness can be distributed in the tomogram. Constrained inversion of models with an overburden layer (models 9 and 10), demonstrated that the use of a constrained mesh significantly improved resolution in the tomogram (figures 3.35 and figure 3.43). The result was improved because the constrained mesh (figure 3.32) confined the slowness of the overburden layer to within the overburden; therefore enabling a more accurate distribution of slowness in the underlying geology. As demonstrated in this thesis, constraining the geological structure and slowness of sections on a mesh based on previously known geological information can greatly improve the resolution of the tomogram.

As a way to evaluate the inversion results, the residual travel-times plot generated from an inversion was also analysed in this research. An anomalous trend observed in all the residual travel-time plots occurred in the travel-times of sources close to the borehole and receivers close to the surface (circle 1, figure 5.1a). The anomaly is interpreted to have been caused by the use of differing forward solvers in the forward modeling (finite-difference) and inversion (fast-marching) processes. The interpretation was tested by using the fast-marching method to provide forward model travel-times for model 1. The residual travel-time plot generated when the fast-marching method was used to calculate both observed and predicted travel-times is shown in figure 5.1b. Comparison of figure 5.1a and 5.1b demonstrates that the residuals in figure 5.1b do not exhibit the same high negative residuals that are observed in figure 5.1a. Therefore, the anomaly labeled 1 in figure 5.1a is likely restricted only to the finite-difference forward modeling and fast-marching solver combination. However, due to the uncertainty in identifying the exact cause of the high negative residual, it is possible that such anomaly will exist in a real data inversion as well.

Apart from the trends that occurred between the sources and receivers in close proximity, it is difficult to determine the cause of other residual patterns observed. For instance, a residual travel-time trend occurred at the slowness boundaries between the checkerboard model tests, but the same trend was not noticed in the geological model tests. Also, for the Eastern Deeps example (model 8), anomalous residual travel-times were observed in rays that passed through (or in the vicinity of) the sulphide. However, for the Reid Brook zone inversion (model 7), no anomalous trend was observed in rays that passed through (or in the vicinity of) the sulphide. Despite the similar slowness values and survey parameters used in model 7 and 8, the residuals from both models do not display similar anomalies. The reason is due to the ambiguity in associating anomalies on a residual to a particular slowness region the ray path passes through. With careful analysis, it is possible to narrow down the potential regions in the subsurface that generate the anomalous travel-time. Besides the residual trend between sources near the boreholes and receivers near the surface, no trend occurs in the residual travel-times for all of the models that can be used to interpret the tomograms. Hence, the residual plots along with the corresponding tomograms were analysed on a case by case basis.

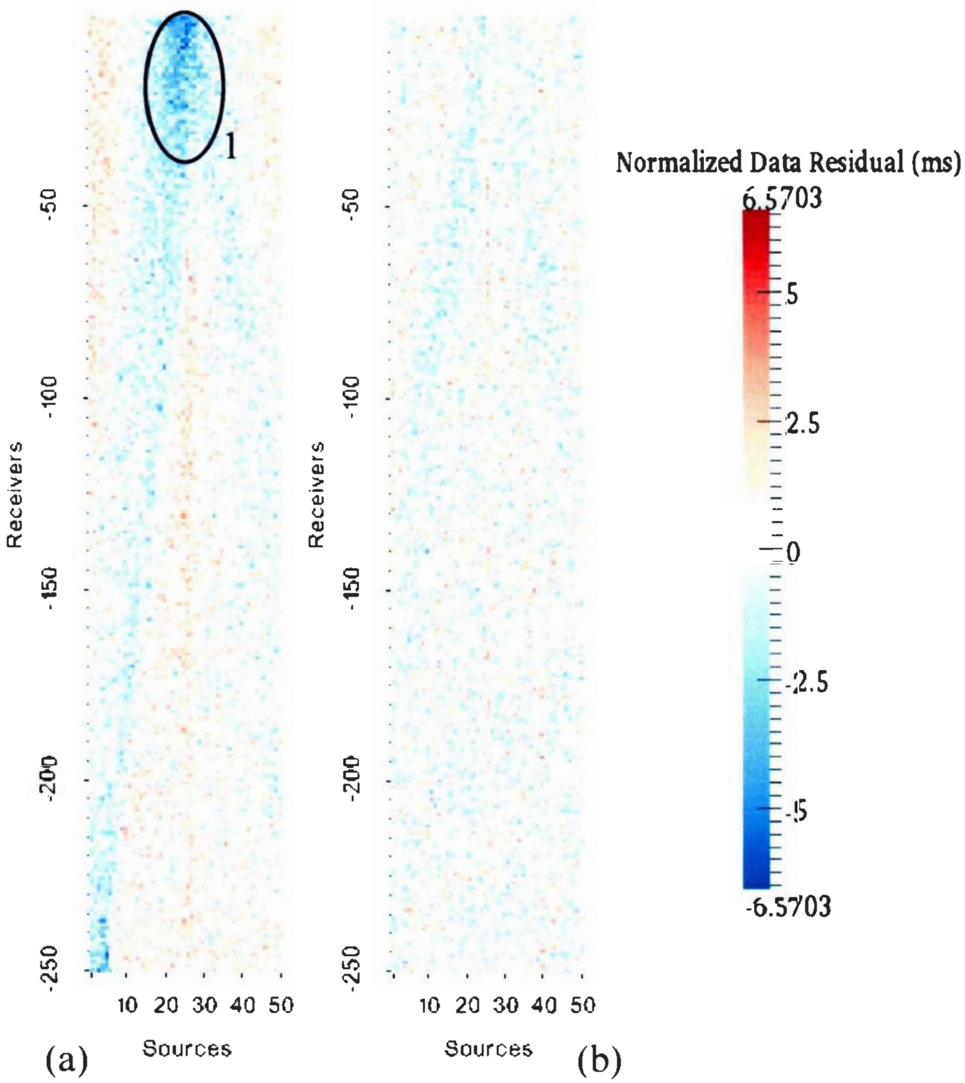

Figure 5.1: comparison between (a) Residual travel-time plot for model 1 using finite-difference for forward modeling and fast-marching in inversion. (b) Residual travel-time plot for model 1 using fast-marching technique for forward modeling and inversion.

Finally, based on the results of this study, it was determined that resolution was attainable up to a depth of approximately 40-50% of the depth of the borehole. However, as observed from the real data example and the synthetic model example in chapter 4, borehole receivers need to start at the surface and go down to twice the depth of the target.

Chapter 6 : Conclusions and Recommendation

In this dissertation, a foundation has been laid for the development of surface-to-borehole travel-time tomography as a new tool for subsurface imaging in the context of mineral exploration. The currently preferred geophysical imaging methods used in mineral exploration include electrical, electromagnetic, induced polarization and potential field methods. However, the method presented in this research produced results that demonstrated the potential for deeper subsurface imaging than the currently preferred tools.

Through the use of synthetic modeling experiments, we demonstrated that the best resolution in a slowness tomogram is obtained in the direction perpendicular to that of the recording raypaths. Also, the resolution of a region is improved when it is sampled by rays from a variety of angles. In addition, when a near-surface low-velocity layer is present, a constrained inversion mesh can be expected to produce a significantly improved resolution in the tomogram.

Due do the range of frequency (50-60Hz) used by the surface-to-borehole tomography method, only medium-to-large scale targets that were greater than 100m-150m in dimension can be resolved in the subsurface. Based on this, the method examined here can be classified as a resource evaluation tool for exploration. In the industry, the best approach for the application of the method will be for closer examination of a subsurface target that is already known to exist from a previously conducted larger scale survey.

With respect to the research carried out here, future work that can be done to improve results and accuracy of the method includes performing inversions using a combination of first-arrival and later-arrival travel-times (Greenhalgh et al.,2003). The use of later-arrival travel-times can eliminate the issue of first arrivals avoiding low-velocity zone as demonstrated in this thesis. In addition, the choice of inversion algorithm used can be changed to one that reproduces sharp slowness boundaries rather than fuzzy boundaries. It is my opinion that there will be an increased appeal for the use of the surface-to-borehole tomography method if slowness in the tomogram can be resolved with sharp boundaries. However, there are sufficient amounts of results and ideas presented in this dissertation that can be used as a stepping stone for future work to be done using the surface-to-borehole travel-time tomography method.

Bibliography

Abdalla, A., R. Stewart, and D. Henley, 1990, Crosshole Seismic Imagine at the Midale field, Southern Saskatchewan, Ann. Nat. Can. Expl. Geophys. Mtg, p. 82-83.

Bellefleur, G., C. Muller, D. Snyder, and L. Matthews, 2004, Downhole seismic imaging of a massive sulphide orebody with mode-converted waves, Halfmile Lake, New Brunswick, Canada. Geophysics, vol. 69, no. 2, p. 318-329.

Chen, G., H. Cao, Y. Wu, F. Zou, and Z. Yao, 2006, Effects of Velocity Contrasts on the Quality of Crosswell Traveltime Tomography and an Improved Method, Chinese Journal of Geophysics, vol. 49, no. 3, p. 810-818.

Deng, L., Cross-well Travel Time Tomography, available at: http://mesoscopic.mines.edu/~jscales/gp605/tomography.nb, Accessed 03/30, 2011.

Duff, D., 2007, Physical Property Analysis, Numerical and Scale Modeling for Planning of Surface Seismic Surveys: Voisey's Bay, Labrador, M.Sc. Thesis, Memorial University of Newfoundland.

Eaton, D., B. Milkereit, and M. Salisbury, 2003, Hardrock Seismic Exploration: Mature Technologies Adapted to New Exploration Targets, *in* Eaton, D., B. Milkereit, and M.

Salisbury, eds., Hardrock Seismic Exploration, Society of Exploration Geophysicists, Geophysical Developments Series, vol. 10, p. 1-6.

Evans-Lamswood, D., D. Butt, R. Jackson, D. Lee, M. Muggridge, R. Wheeler, and D. Wilton, 2000, Controls Associated with the Distrubution of Sulfides in the Voisey's Bay Ni-Cu-Co Deposit, Labrador, Economic Geology, vol. 95, p. 749-769.

Farquharson, C., 2008, Constructing Piecewise-Constant Models in Multidimensional Minimum-structure Inversions, Geophysics, vol. 73, no. 1, p. K1-K9.

Goulty, N., 1993, Contrlled-Source Tomography for Mining and Engineering Applications, *in* Iyer, H. and K. Hirahara, eds., Seismic Tomography: Theory and Practice, Chapman and Hall, p. 797-811.

Greenhalgh, S., T. Gruber, and B. Zhou, 2003, Velocity field imaging with an anomaly recovery algorithm, incorporating later arrivals, Geophysics, vol. 68, no. 2, p. 589-599.

Harris, J. M., 1989, Cross-well Seismic Measurement in Sedimentary Rocks, Proc. 64, Annual technological conference of petroleum engineering, San Antonio, Texas, p. 611-614.

Kanli, A., Z. Pronay, and R. Miskolczi, 2008, The Importance of the Spread System Geometry on the Image Reconstruction of Seismic Tomography, Journal of Geophysics and Engineering, vol. 5, p. 77-85.

Kelly, K., R. Ward, S. Treitel, and R. Alford, 1976, Synthetic Seismograms: A Finite-Difference Approach, Geophysics, vol. 41, no. 1, p. 2-27.

Kerr, A., 2008, Mineral Commodities of Newfoundland and Labrador: Nickel, Geological Survey Mineral Commodities Series, no. 2, p. 1-8.

LeBlanc, A., R. Fortier, M. Allard, C. Cosma, and S. Buteau, 2004, Seismic Cone Penetration Test and Seismic Tomography in Permafrost, Canadian Geotechnical Journal, vol. 41, no. 5, p. 796-813.

Lee, M., 1990, Traveltime Inversion using Transmitted waves of Offset VSP Data, Geophysics, vol. 55, no. 8, p. 1089-1097.

Lelièvre, P., C. Farquharson, and C. Hurich, 2011a, Computing First-Arrival Seismic Traveltimes on Unstructured 3-D Tetrahedral Grids using the Fast Marching Method, Geophysical Journal International, vol. 184, p. 885-896.

Lelièvre, P., C. Farquharson, and C. Hurich, 2011b, Inversion of First-Arrival Seismic Traveltimes without Rays, Implemented on Unstructured Grids, Geophysical Journal International, vol. 185, p. 759-763.

Lelièvre, P., C. Farquharson, and C. Hurich, 2012, Joint Inversion of Seismic Traveltimes and Gravity Data on Unstructured Grids with Application to Mineral Exploration, Geophysics, vol. 77, no. 1, p. K1-K15.

Levander, A., 1988, Fourth-order Finite-Difference P-SV Seismograms, Geophysics, vol. 53, no. 11, p. 1425-1436.

Leveque, J., L. Rivera, and G. Wittlinger, 1993, On the use of the Checker-board Test to Assess the Resolution of Tomographic Inversions, Geophysical Journal International, vol. 115, p. 313-318.

Li, Y., X. Zhao, R. Zhou, and D. Dushman, 2005, 3C VSP Tomography Inversion for Subsurface P- and S- Wave Velocity Distribution, Society for Exploration Geophysicists, Expanded Abstract, p. 2625-2628.

Mao, W. and G. Stuart, 1997, Transmission-Reflection Tomography: Application to Reverse VSP Data, Geophysics, vol. 62, no. 3, p. 884-894.

Mari, J. and F. Coppens, 2003, Main applications of well seismic, *in* Revol, J., ed., Well seismic surveying, Editions TECHNIP, p. 122.

McMechan, G., 1983, Seismic Tomography in Boreholes, Geophy. J.R. astr. Soc., vol. 74, p. 601-612.

Moret, G., M. Knoll, W. Barrash, and W. Clement, 2006, Investigating the Stratigraphy of an Alluvial Aquifer using Crosswell Seismic Travaltime Tomography, Geophysics, vol. 71, no. 3, p. B63-B73.

Mosher, C., 2009, Minimum-Structure Borehole Gravity Inversion, M.Sc. Thesis, Memorial University of Newfoundland.

Rawlinson, N., S. Pozgay, and S. Fishwick, 2010, Seismic Tomography: A Window into Deep Earth, Physics of the Earth and Planetary Interiors, vol. 178, p. 101-135.

Reynolds, J., 1997, Applied Seismology: Introduction and Principles, *in* John Wiley and Sons, ed., An Introduction to Applied and Environmental Geophysics, John Wiley & Sons Ltd, p. 212-275.

Rogers, P., S. Edwards, J. Young, and M. Downey, 1987, Geotomography for the Delineation of Coal Seam Structure, Geoexploration, vol. 24, p. 301-328.

Salisbury, M. and D. Snyder, 2007, Application of Seismic Methods to Mineral Exploration, *in* Goodfellow, W. D., ed., Mineral Deposits of Canada: A synthesis of Major Deposit Types, District Metallogeny, the Evolution of Geological Provinces and Exploration methods, Geological Association of Canada, Mineral Deposits Division, Special Publications 5, p. 971-982.

Sheriff, R. and L. Geldart, 1995, Seismic Velocity, *in* Exploration Seismology, Cambridge University Press, p. 107-143.

Stevenson, F., R. Higgs, and R. Durrheim, 2003, Seismic Imaging of Precious and Base-Metal Deposits in Southern Africa, *in* Eaton, D., B. Milkereit, and M. Salisbury, eds., Hardrock Seismic Exploration, Society of Exploration Geophysicists, Geophysical Developments Series, vol. 10, p. 141-156.

Tammerik, G., P. Stacey, and W. Crosby , 2009, Rock Slope Management at Sossego Mine, available at: http://dc265.4shared.com/doc/DJVy8VA5/preview.html, Accessed 02/16, 2012.

Wardell, J., 1970, A Comparison of Land Seismic Sources, Geoexploration, vol. 8, p. 205-229.

Widess, M., 1973, How Long is a Thin Bed? Geophysics, vol. 38, no. 6, p. 1176-1180.

Appendix A: Additional examples/figures

Appendix A is a compilation of addition model examples that were performed for this thesis. In chapter 3 and 4, the residual travel-times plot for models without an accompanying residual plot are also located in this section.

Figure A1 is the slowness tomogram for model 1 where the fast-marching method was used to generate travel-time data.

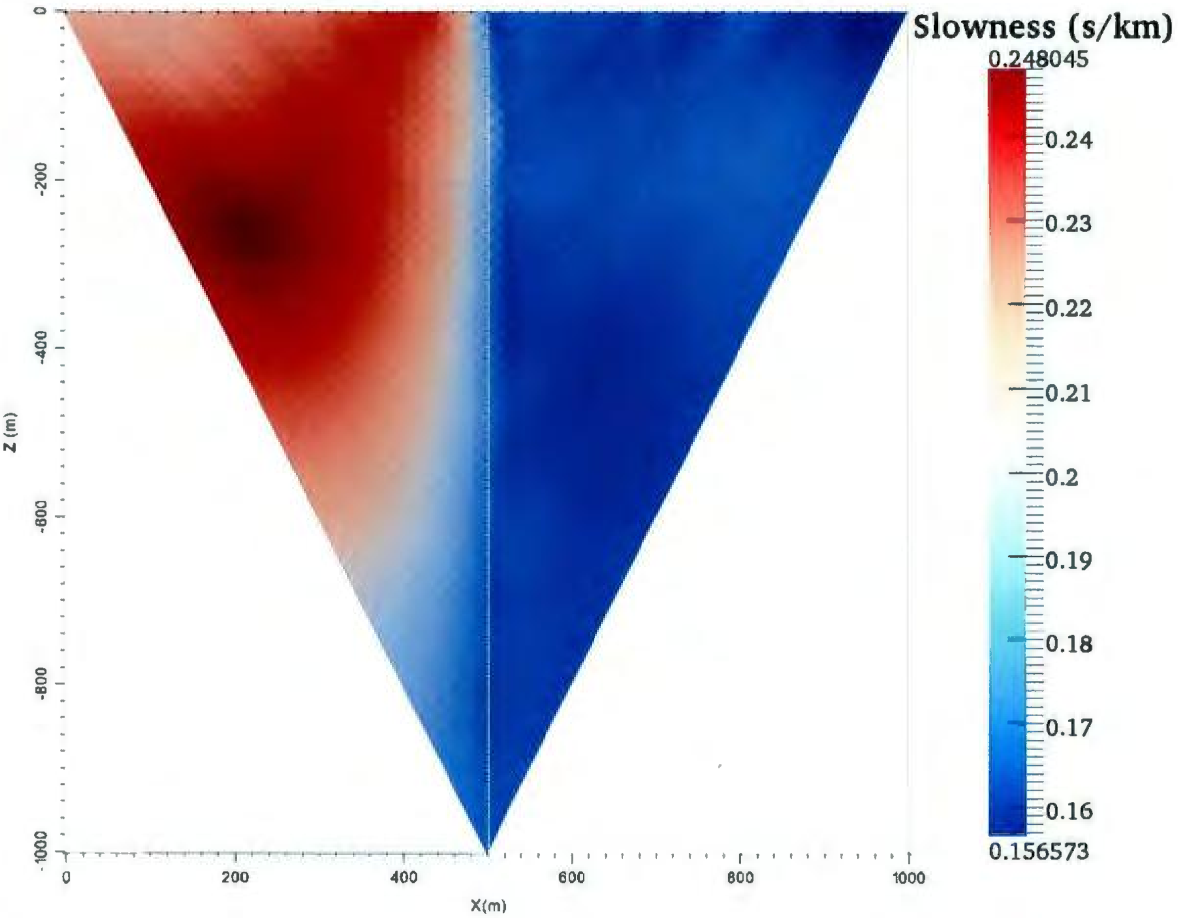

Figure A1: Model 1 slowness tomogram using a fast-marching forward solver to calculate first arrival travel-times for the inversion.

The model, shown in Figure A2, was designed to test the ability of the surface-to-borehole method in resolving vertical boundaries.

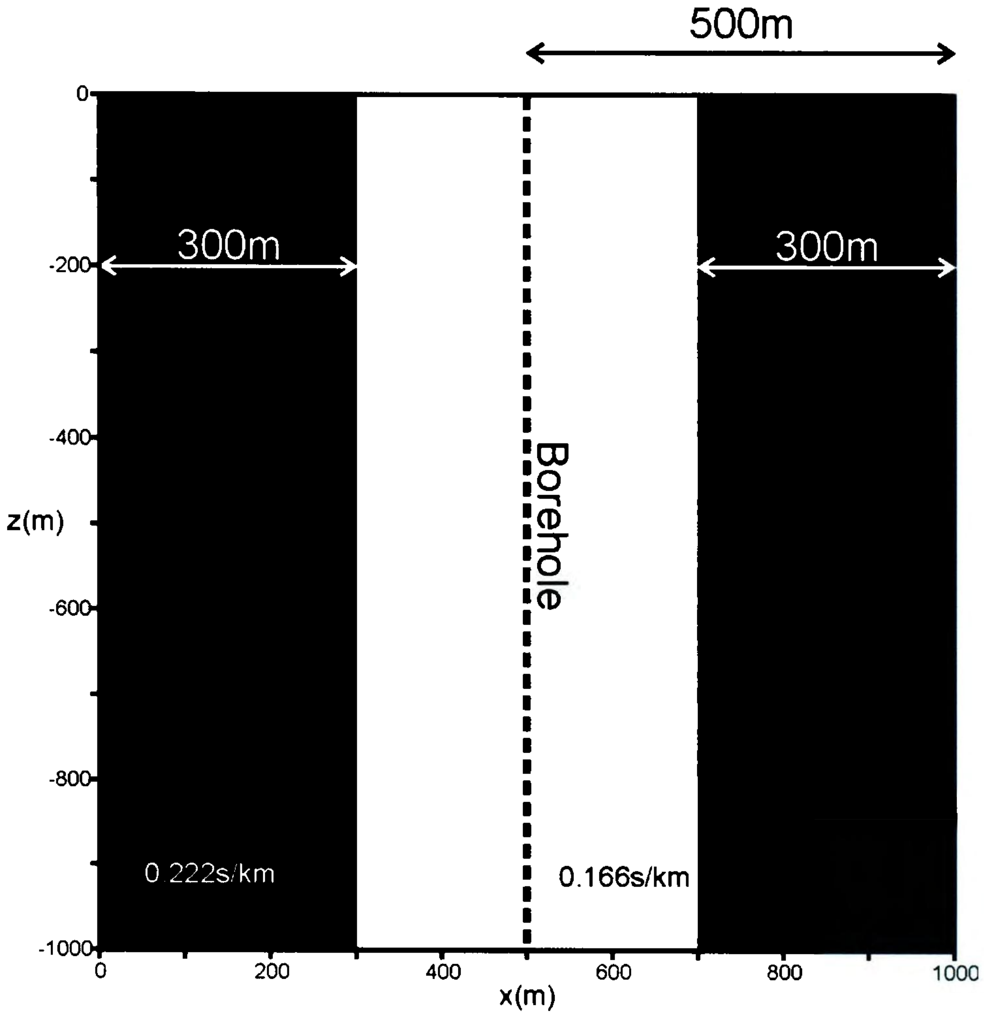

Figure A2: True Model for flag model.

The tomogram, shown in figure A3, is the result for the true model shown in figure A2.

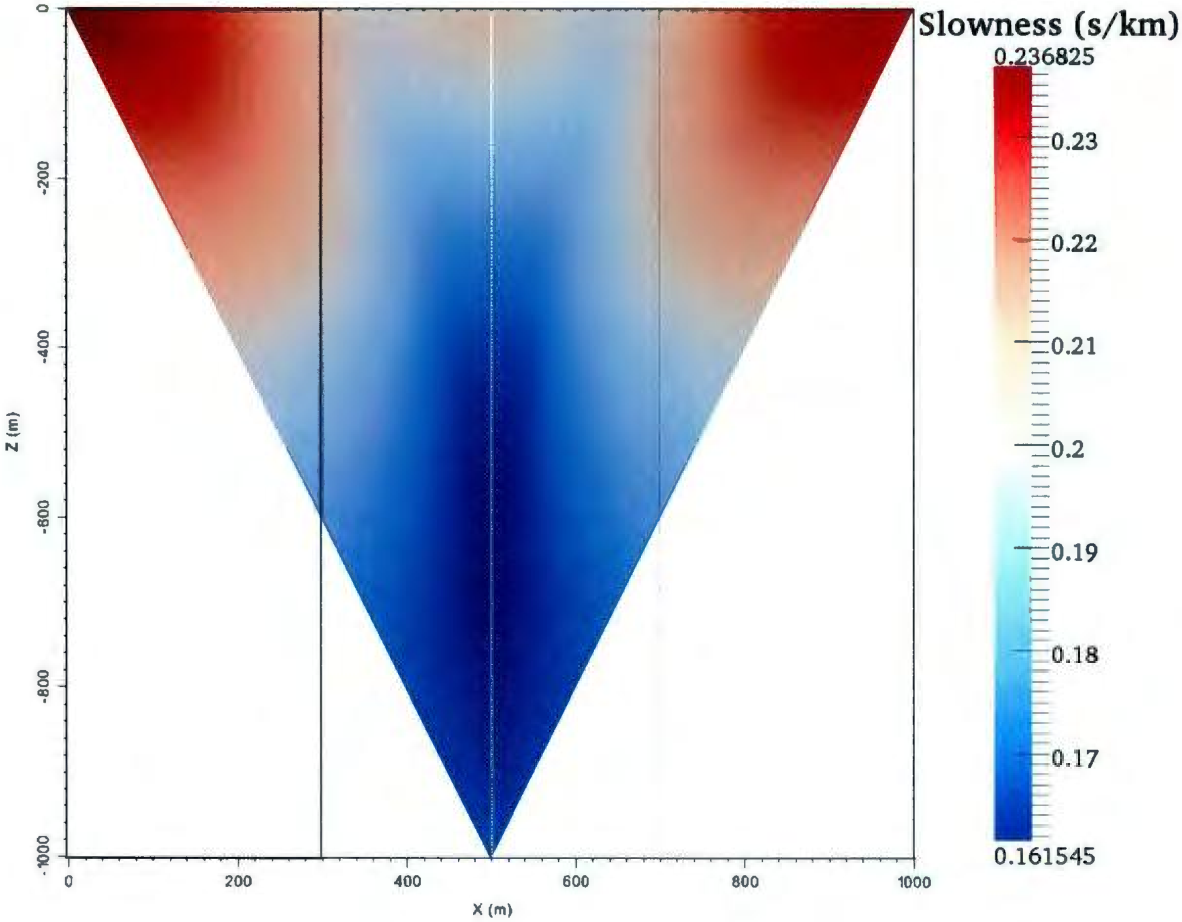

Figure A3: Slowness tomogram for flag model.

Figure A4 is the Reid Brook zone model slowness tomogram generated using travel-time data derived from the fast-marching method.

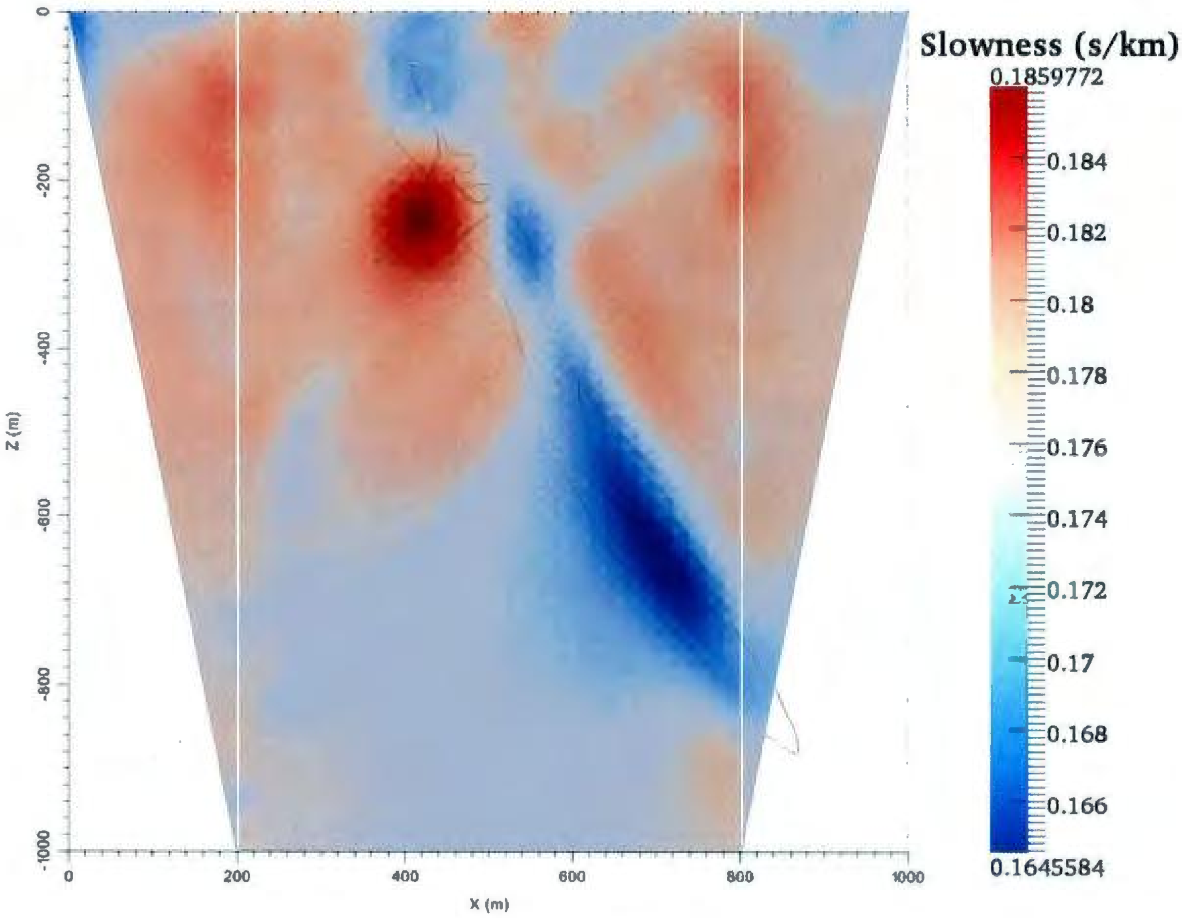

Figure A4: Reid Brook inversion result. Fast-marching forward solver was used to calculate the first arrival travel-times.

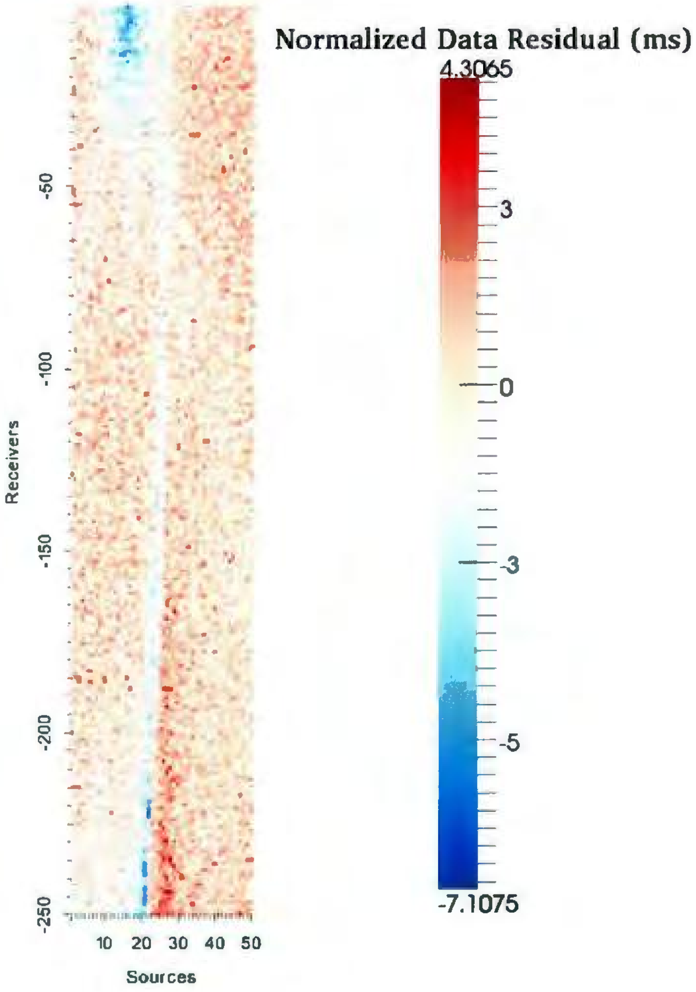

Figure A5: Residual travel-time plot for model 2.

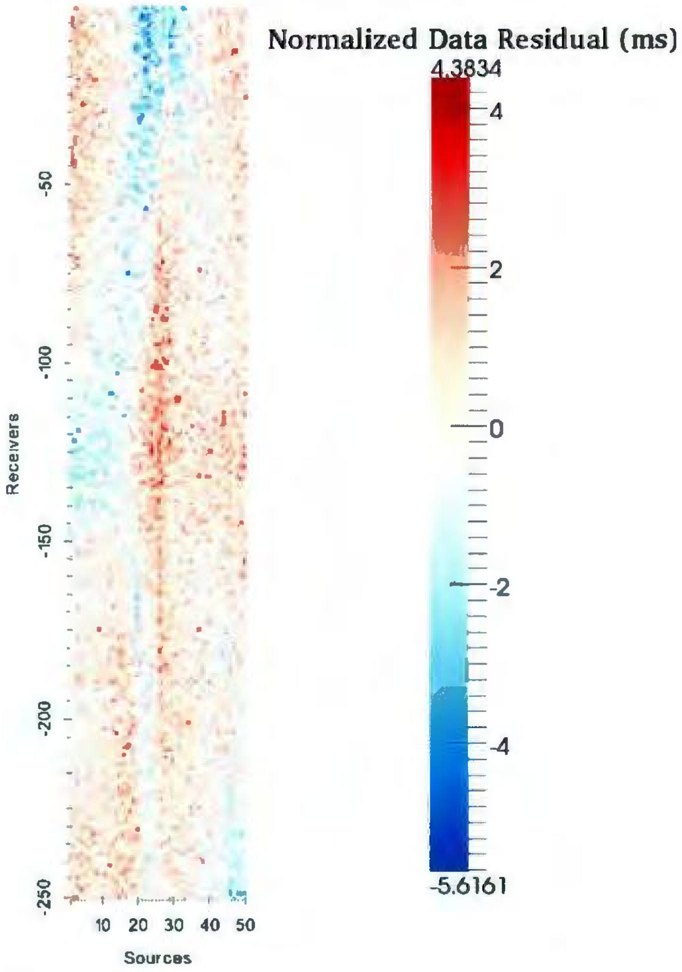

Figure A6: Residual travel-time plot for model 4.

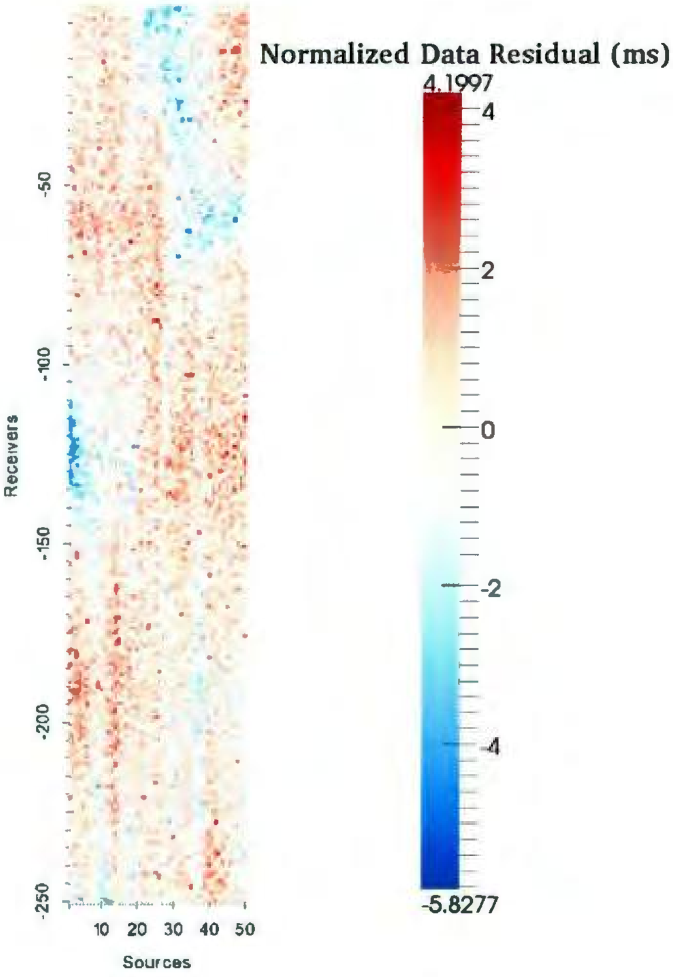

Figure A7: Residual travel-time plot for model 5.

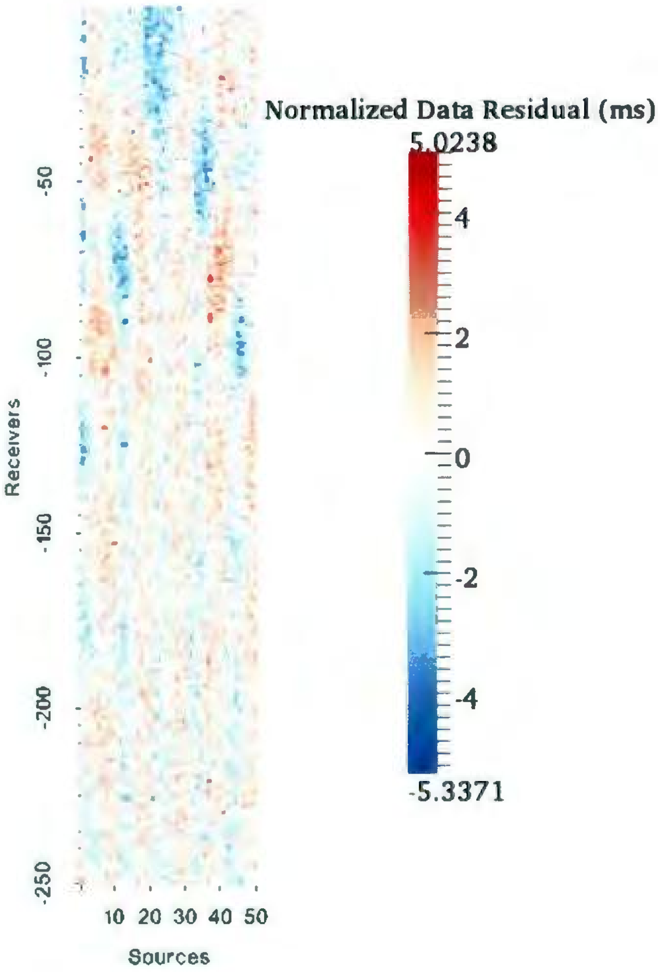

Figure A8: Residual travel-time plot for model 6.

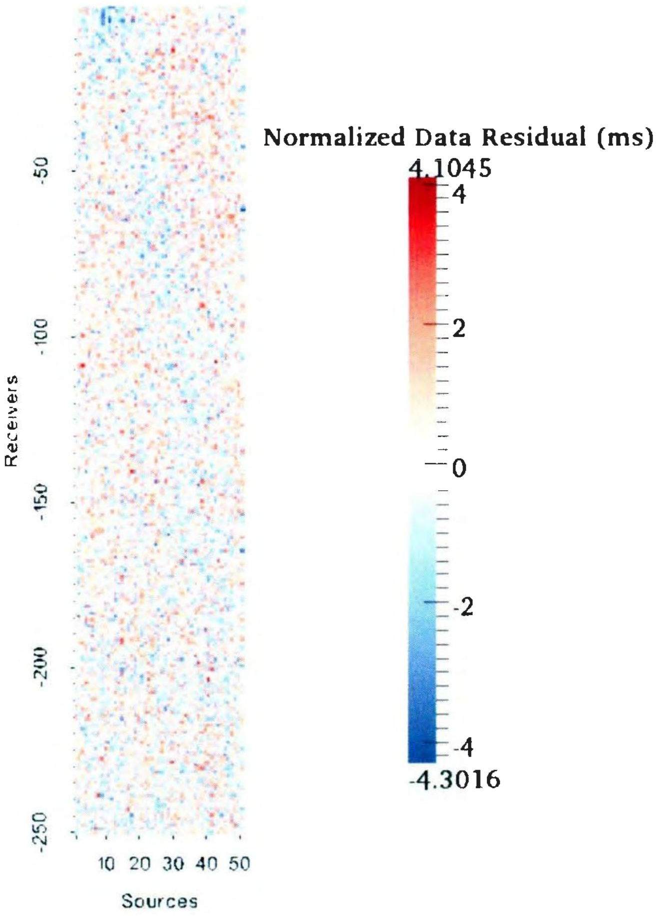

Figure A9: Residual travel-time plot for model 7 using borehole #1 only.

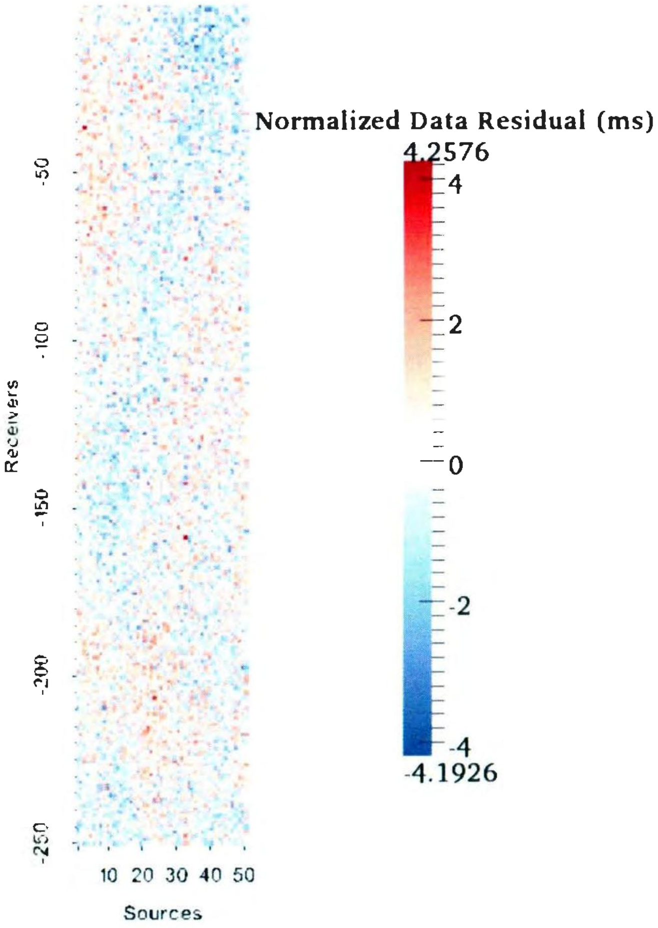

Figure A10: Residual travel-time plot for model 7 using borehole #2 only.

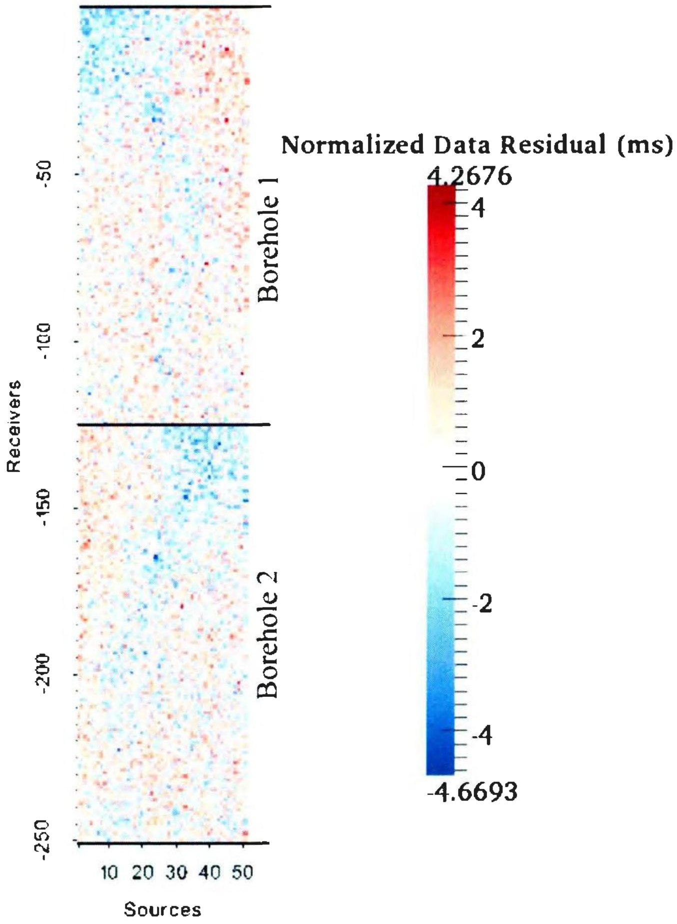

Figure A11: Residual travel-time plot for model 7 using boreholes #1 and #2.

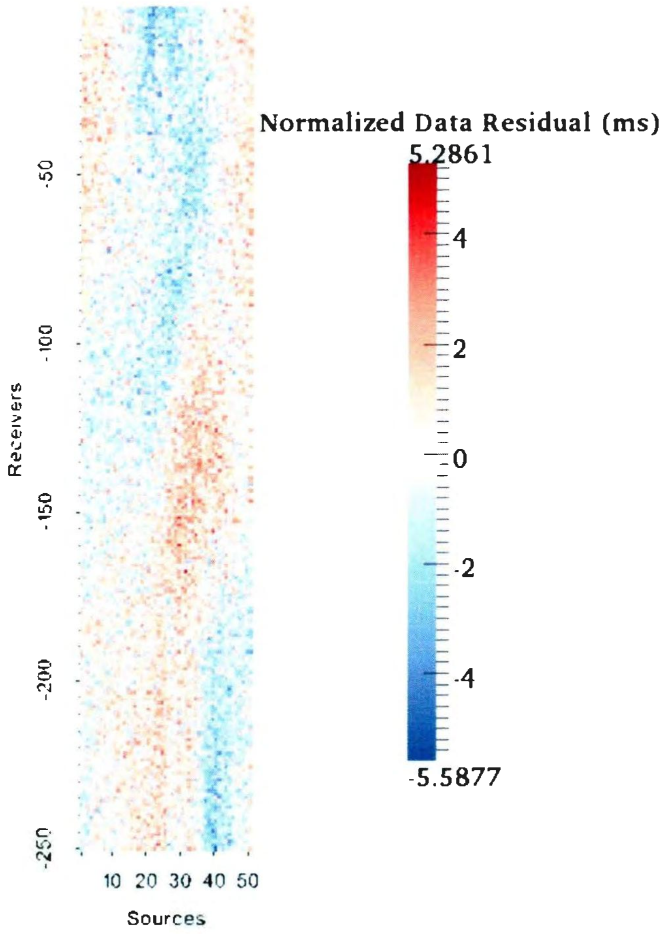

Figure A12: Residual travel-time plot for model 9 inversion with no overburden.

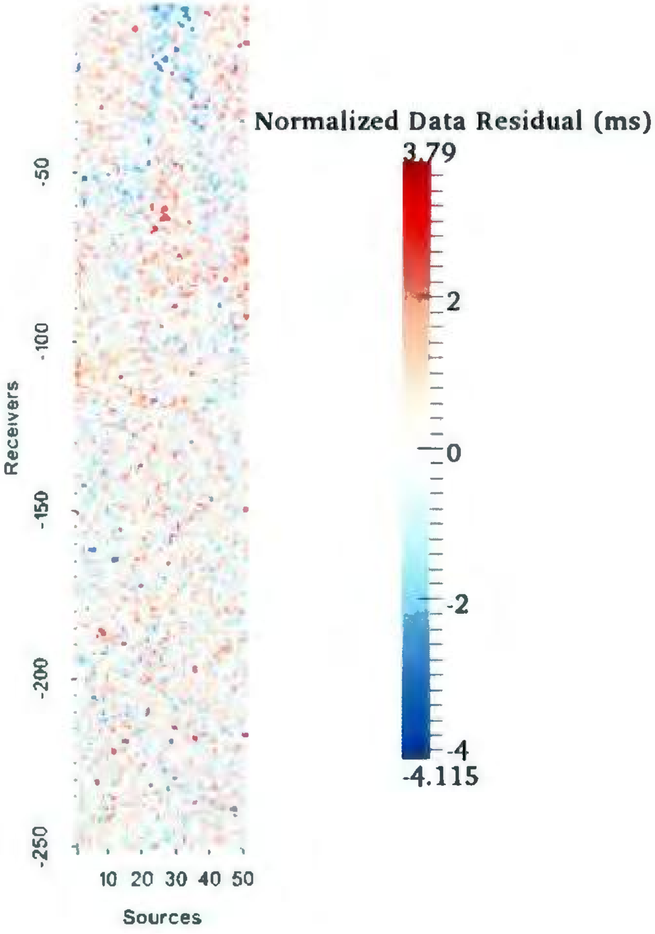

Figure A13: Residual travel-time plot for model 10.0 (no overburden) using borehole #2 only.

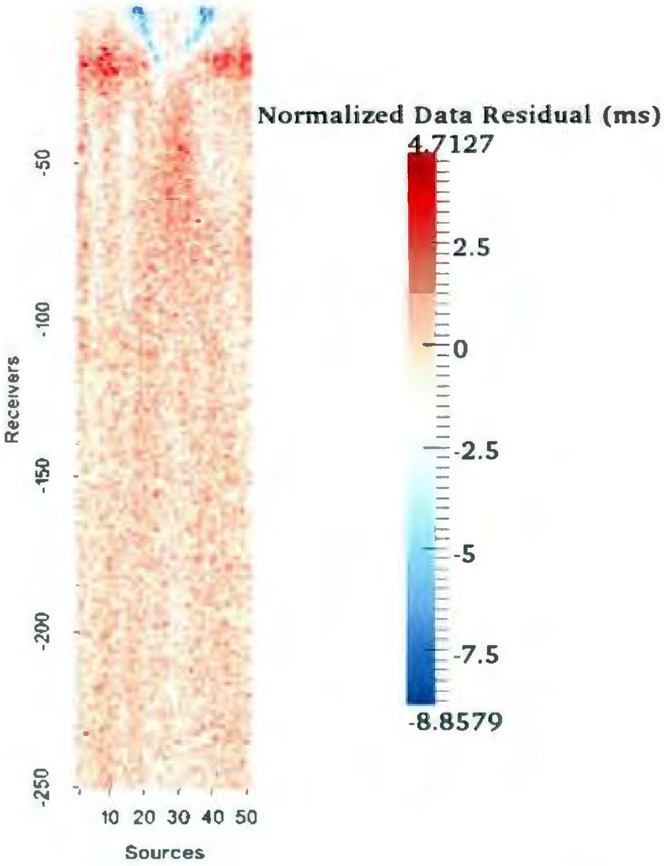

Figure A14: Unconstrained inversion residual travel-time plot for model 10.1 (with overburden) using borehole #2 only.

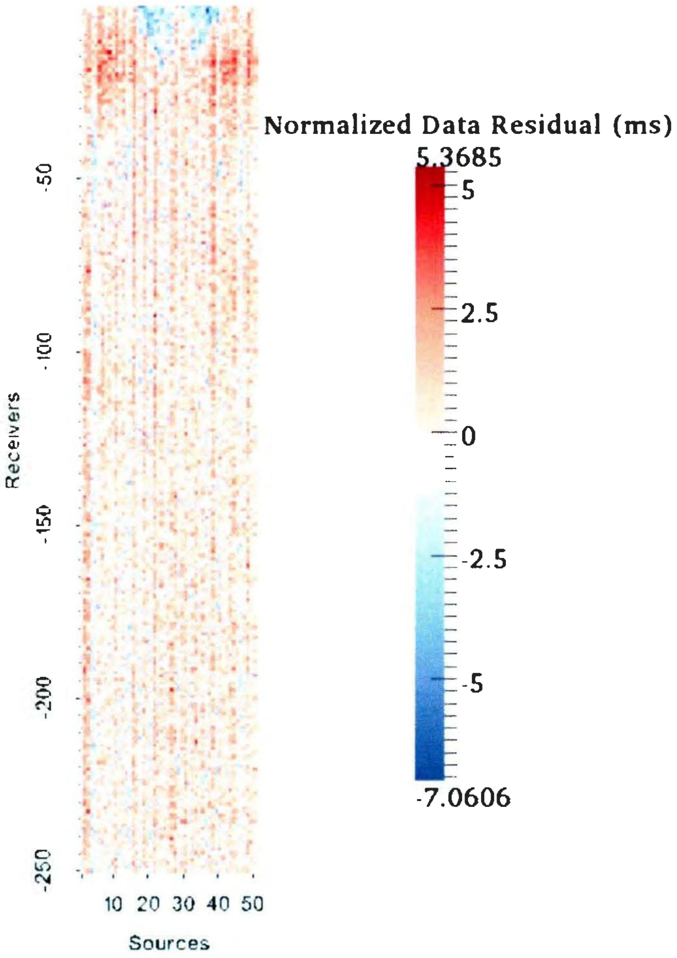

Figure A15: Constrained inversion residual travel-time plot for model 10.1 using borehole #2 only.

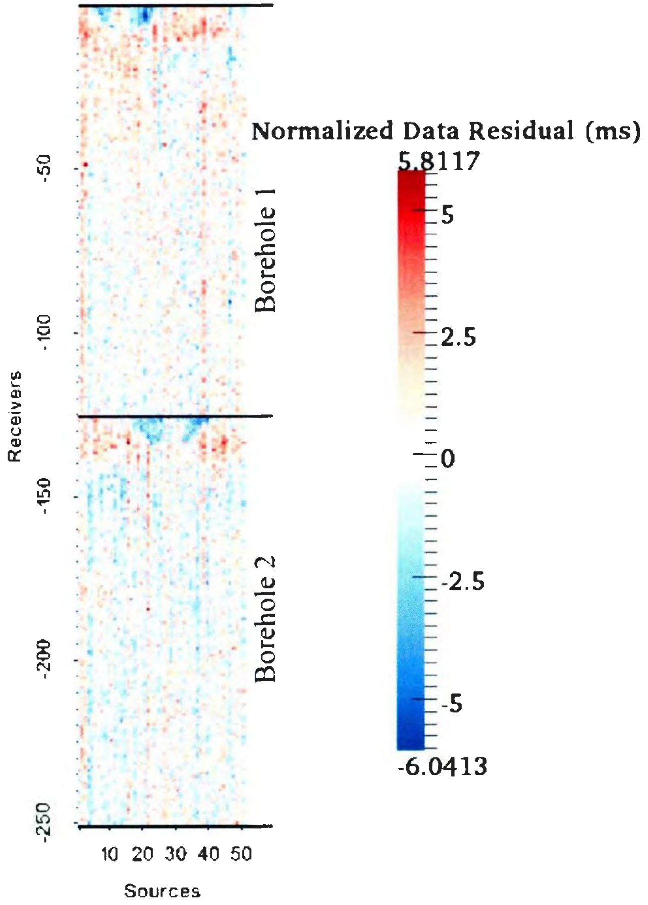

Figure A16: Constrained inversion residual travel-time plot for model 10.1 using boreholes #1 and #2.

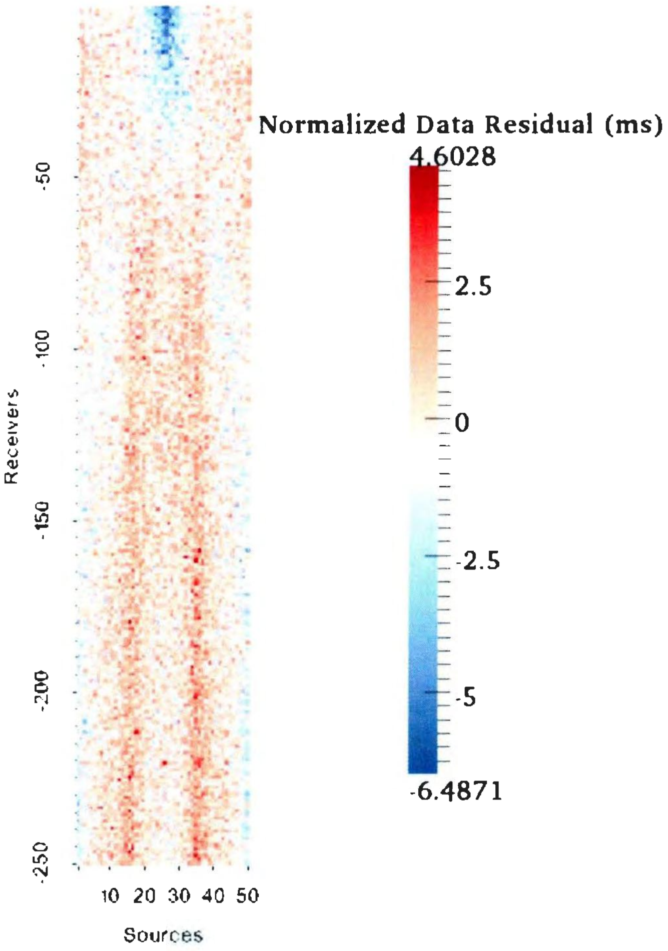

Figure A17: Residual travel-times for flag model.

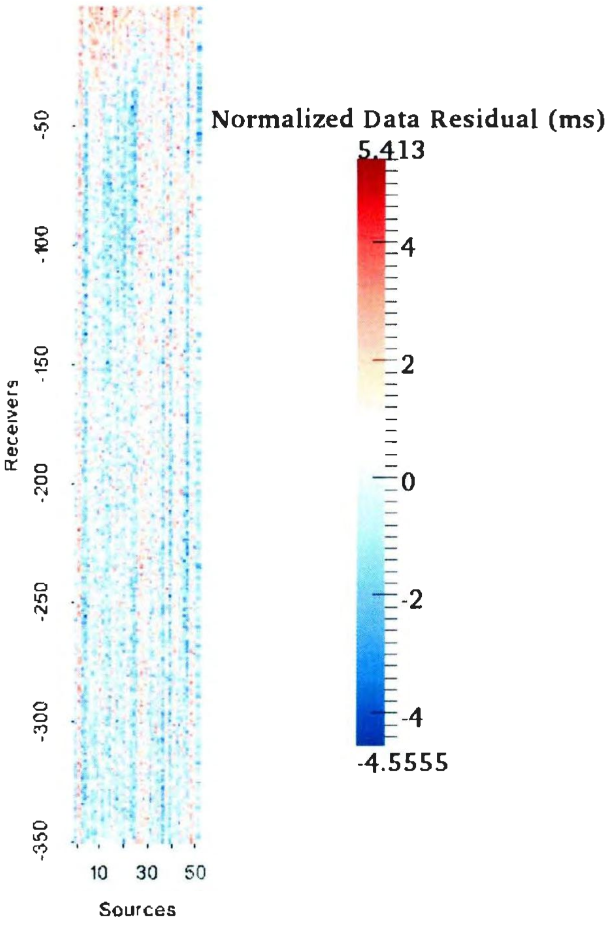

Figure A18: Residual travel-times plot for model 9 with receiver location starting at 301m depth.

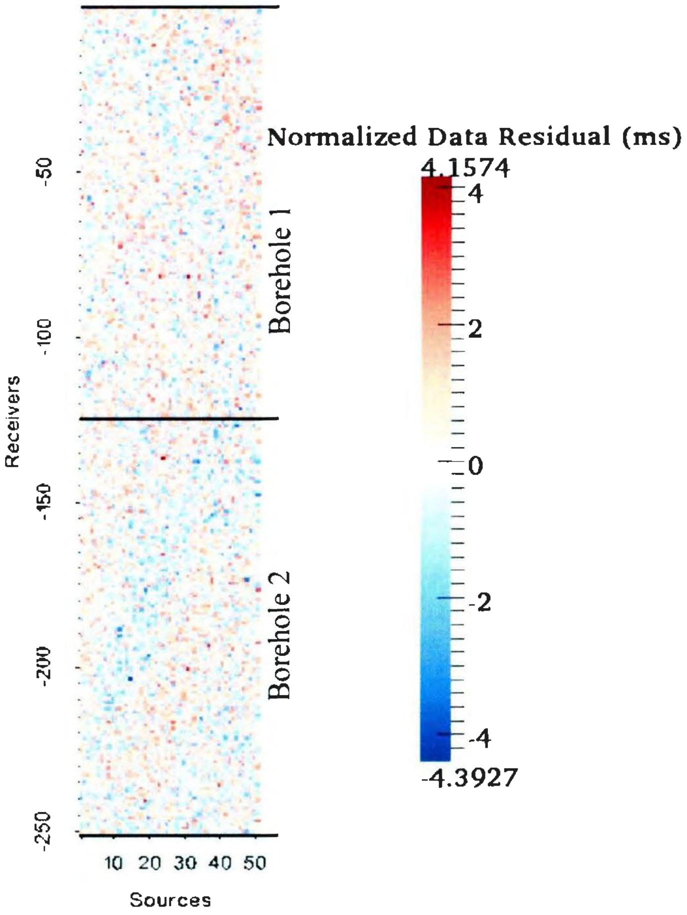

Figure A19: Reid brook model residual travel-times, using fast-marching method to calculate travel-times.

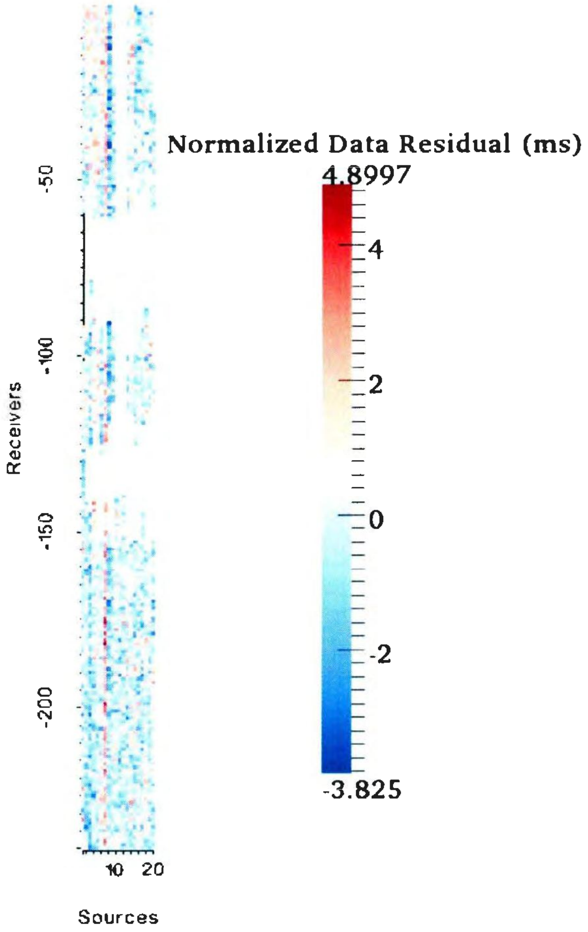

Figure A20: Field data residuals travel-time plot.

Appendix B: Forward and inverse parameters.

Appendix B contains tables showing forward modeling parameters used for each model in the thesis. The inversion parameters used for each model are also summarized in tables in this section.

Model	# of shots	# of receivers	Borehole location (m)	X location of first and last shot (m)	Z location of first and last receiver (m)	Shot spacing (m)	Receiver spacing (m)	Dominant source frequency (Hz)
1	50	499	500	0/980	-2/-998	20	2	50

Table A.1: Forward modeling parameters used for model 1

Model	# of shots used	Shot spacing (m)	First/ last shot location (m)	# of receivers used	Receiver spacing (m)	First/ last receiver depth (m)	Chifact used	Chi tolerance used	Standard deviation (ms)

1	50	20	0/980	250	4	-2/-998	1.5	0.1	2

Table A.2: Inversion parameters for model 1

Model	# of shots	# of receivers	Borehole location (m)	X location of first and last shot (m)	Z location of first and last receiver (m)	Shot spacing (m)	Receiver spacing (m)	Dominant source frequency (Hz)
2	50	499	300	0/980	-2/-998	20	2	50

Table A.3: Forward modeling parameters for model 2

Model	# of shots used	Shot spacing (m)	First/ last shot location (m)	# of receivers used	Receiver spacing (m)	First/ last receiver depth (m)	Chifact used	Chi tolerance used	Standard deviation (ms)

2	50	20	0/980	250	4	-2/-998	1.5	0.1	2

Table A.4: Inversion parameters for model 2

Model	# of shots	# of receivers	Borehole location (m)	X location of first and last shot (m)	Z location of first and last receiver (m)	Shot spacing (m)	Receiver spacing (m)	Dominant source frequency (Hz)
3	50	499	500	0/980	-2/-998	20	2	50

Table A.5: Forward modeling parameters for model 3

Model	# of shots used	Shot spacing (m)	First/ last shot location (m)	# of receivers used	Receiver spacing (m)	First/ last receiver depth (m)	Chifact used	Chi tolerance used	Standard deviation (ms)

3	50	20	0/980	250	4	-2/-998	1.5	0.1	2

Table A.6: Inversion parameters for model 3

Model	# of shots	# of receivers	Borehole location (m)	X location of first and last shot (m)	Z location of first and last receiver (m)	Shot spacing (m)	Receiver spacing (m)	Dominant source frequency (Hz)
4	50	499	500	0/980	-2/-998	20	2	50

Table A.7: Forward modeling parameters for model 4

Model	# of shots used	Shot spacing (m)	First/ last shot location (m)	# of receivers used	Receiver spacing (m)	First/ last receiver depth (m)	Chifact used	Chi tolerance used	Standard deviation (ms)

4	50	20	0/980	250	4	-2/-998	1.5	0.1	2

Table A.8: Inversion parameters for model 4

Model	# of shots	# of receivers	Borehole location (m)	X location of first and last shot (m)	Z location of first and last receiver (m)	Shot spacing (m)	Receiver spacing (m)	Dominant source frequency (Hz)
5	50	499	500	0/980	-2/-998	20	2	50

Table A.9: Forward modeling parameters for model 5

Model	# of shots used	Shot spacing (m)	First/ last shot location (m)	# of receivers used	Receiver spacing (m)	First/ last receiver depth (m)	Chifact used	Chi tolerance used	Standard deviation (ms)
5	50	20	0/980	250	4	-2/-998	1.5	0.1	2

Table A.10: Inversion parameters for model 5

Model	# of shots	# of receivers	Borehole location (m)	X location of first and last shot (m)	Z location of first and last receiver (m)	Shot spacing (m)	Receiver spacing (m)	Dominant source frequency (Hz)
6	50	499	500	0/980	-2/-998	20	2	50

Table A.11: Forward modeling parameters for model 6

Model	# of shots used	Shot spacing (m)	First/ last shot location (m)	# of receivers used	Receiver spacing (m)	First/ last receiver depth (m)	Chifact used	Chi tolerance used	Standard deviation (ms)

6	50	20	0/980	250	4	-2/-998	1.5	0.1	2

Table A.12: Inversion parameters for model 6

Model	# of shots	# of receivers per borehole	Borehole locations (m)	X location of first and last shot (m)	Z location of first and last receiver (m)	Shot spacing (m)	Receiver spacing (m)	Dominant source frequency (Hz)
7	51	500	201/801	0/1000	0/-998	20	2	60

Table A.13: Forward modeling parameter for model 7

Model	# of shots used	Shot spacing (m)	First/ last shot location (m)	# of receivers used	Receiver spacing (m)	First/ last receiver depth (m)	Chifact used	Chi tolerance used	Standard deviation (ms)
7(borehole 1 only)	51	20	0/1000	250	4	0/-996	1.0	0.1	2

7(borehole 2 only)	51	20	0/1000	250	4	0/-996	1.0	0.1	2
7(boreholes 1 and)2	51	20	0/1000	250	8	0/-992	1.0	0.2	2

Table A.14: Inversion parameters for model 7

Model	# of shots	# of receivers per borehole	Borehole locations (m)	X location of first and last shot (m)	Z location of first and last receiver (m)	Shot spacing (m)	Receiver spacing (m)	Dominant source frequency (Hz)
8	51	500	301/601/ 1001/1701	0/2000	0/-998	40	2	60

Table A.15: Forward modeling parameters for model 8

Model	# of shots used	Shot spacing (m)	First/ last shot location (m)	# of receivers used	Receiver spacing (m)	First/ last receiver depth (m)	Chifact used	Chi tolerance used	Standard deviation (ms)

8(boreholes 1, 3 and 4 only)	51	40	0/1000	250	8	0/-992	1.5	0.2	2
8(boreholes 1, 2, 3 and 4)	51	40	0/1000	500	8	0/-992	1.5	0.2	2

Table A.16: Inversion parameters for model 8

Model	# of shots	# of receivers per borehole	Borehole locations (m)	X location of first and last shot (m)	Z location of first and last receiver	Shot spacing (m)	Receiver spacing (m)	Dominant source frequency (Hz)
9	51	1000	451	0/1000	0/-998	20	1	60

Table A.17: Forward modeling parameters for model 9

Model	# of shots used	Shot spacing (m)	First/ last shot location (m)	# of receivers used	Receiver spacing (m)	First/ last receiver depth (m)	Chifact used	Chi tolerance used	Standard deviation (ms)
9.0	51	20	0/1000	250	4	0/-996	1.5	0.1	2
9.1, unconstrained	51	20	0/1000	250	4	0/-996	1.5	0.1	2
9.1, constrained	51	20	0/1000	250	4	0/-996	1.5	0.2	2

Table A.18: Inversion parameters for model 9

Model	# of shots	# of receivers per borehole	Borehole locations (m)	X location of first and last shot (m)	Z location of first and last receiver	Shot spacing (m)	Receiver spacing (m)	Dominant source frequency (Hz)
10	51	1000	250/550	0/1000	0/-998	20	1	60

Table A.19: Forward modeling parameters used for models 9 (9.0 and 9.1) and 10 (10.0 and 10.1).

Model	# of shots used	Shot spacing (m)	First/ last shot location (m)	# of receivers used	Receiver spacing (m)	First/ last receiver depth (m)	Chifact used	Chi tolerance used	Standard deviation (ms)
10.0	51	20	0/1000	250	4	0/-996	1.0	0.1	2
10.1, unconstrained(borehole 2 only)	51	20	0/1000	250	4	0/-996	1.5	0.1	2

10.1, constrained (borehole 2 only)	51	20	0/1000	250	4	0/-996	1.5	0.2	2
10.1, constrained (boreholes 1 and 2)	51	20	0/1000	250	8	0/-992	1.5	0.2	2

Table A.20: Inversion parameters used for models 9 and 10.

Appendix C: Forward modeling procedures and input files

This section of the appendix describes the steps used to create a model. The input files used to generate seismograms using the finite-difference method is also included in this section.

Creating Synthetic Seismograms

Prepare the model:

In CorelDraw:

- Create background box and superimpose bodies of interest
- Turn off all outlines
- Set grayscale values for all bodies according to what their velocity is
- Export as 'pcx' file setting pixels width according to actual size of model, keep in mind the model needs to have 10 grids per wavelength for stability, the limiting wavelength is calculated by dividing the smallest velocity by the largest frequency, take note of the number of pixels in rows & columns

ssh_ftp 'pcx' file to where you are working

convert to ascii file:

```
./convertpcx file.pcx >file.txt
```

convert to image file and plot for quality control:

```
a2b n1=1 <file.txt >file.bin
ximage n1=# of rows legend = 1 <file.bin &
```

create empty velocity files, run program for each separate velocity:

```
./consvel
```

create a single velocity model for input into finite difference calculator, manipulates ascii files and relates the constant velocities specified in consvel to bodies in the modl according to grey tone ranges.

```
./fillvel2
```

Note that previous file handling can create interpolated edges so the choice of range values can be used to group interpolated values into an appropriate velocity (For 2 body model, ranges used were 0,200(light) & 201,255(dark))

Input: model.txt.vel

display model file:

```
a2b n1=1<velfile.txt >velfile.bin
ximage n1=#rows legend=1 blockinterp = 0 <velfile.bin &
```

Run Finite Difference: SHOOT_VSP2

SHOOT_VSP2

```
#!/bin/csh -f

# Function: Shoot into fixed receiver array.

# convert windowed su file to straight binary file


set shotnum = 1      #shot number

set shotx = 0        #x location (distance) of first shot

set total = 51      #total number of shots to record

set count = 0

rm resamp.su


while ($count < $total)


echo Start FD modeling

date


sufdmod2 <flat_ovb.bin  >/dev/null \

dx=1 dz=1 \ #grid spacing

nx= 1000  nz= 1000 \ #number of grids

xs=$shotx \

zs=0 \

vsx=650 \

tmax=0.5  \ #maximum recording time in seconds

abs=1,1,1,1 \ #absorbing boundaries 0=false, 1=true
```

```
vsfile=$shotnum.su \
verbose=1 \
fpeak=60 \ #peak frequency

echo shotnum $shotnum complete

# Resample the seismogram
suresamp nt=500 dt=.001 <$shotnum.su >TEMP
cat TEMP >> resamp.su
echo resample complete
rm $shotnum.su

#write log file for present shot
#./writelog

# set up next shot
set shotnum  = `expr $shotnum + 1`
set count    = `expr $count + 1`
set shotx = `expr $shotx + 20`    #The increment is in terms of distance
not grids.

#date

end
```

```
# Convert to segy
segyhdrs <resamp.su
segywrite endian=0 tape=flat_ovb650.sgy <resamp.su
#segywrite endian=0 tape=tos_mov.sgy <resamp.su
echo segy file written

exit
```

The finite difference code used was supplied by Dr. Charles Hurich.

Appendix D: Inversion procedures and Input files

After the travel-times have been picked in ProMAX and geometry information has been assigned to the travel-times then they can be exported as a .node file to be prepared for inversion. In this section of the appendix, we describe the steps used in generating slowness tomograms from travel-time data. The input files used for performing the inversions are also included in this section of the appendix.

Node file format for data file containing geometry and travel-time information.

<# of Traces> <dimensions (4==2d ; 6==3d)> <# of attributes> <# of boundary markers>

[Trace# sx sz rx rz t]

or

[Trace# sx sy sz rx ry rz t]

sx, sy, sz = source x,y and z coordinate. rx, ry, rz= receiver x, y and z coordinate. t=travel-time

If the data file needs to be decimated then the following command can be used:

```
./decimate filename from to by
```

Decimates the number traces from trace 1 to trace n by a specified value

Split the data file into source, receiver and travel-time file:

```
./split_tobs filename ndim
```

Splits the geometry and travel-time file into:

```
1) source coordinate file (.node file)
2) receivers coordinate file (.node file)
3) travel-time file (.ele file)
```

For quality control and visualization purposes, the source, receiver and travel-time files can be converted to .vtu files:

```
./node2vtu root [zrev]
Or
./ele2vtu root
```

Noise or uncertainty can be added to the travel-time data using:

```
./add_noise datafile mode col1 col2 flo perflo per zrev
```

Inversion mesh can be created using either:

```
./ubcgif2vtu meshinfo model outroot [split]
 Or
triangle -cpqna250A meshinfo
```

The ubcgif2vtu creates rectilinear meshes and each rectangle/square in the mesh can be split into 2 or 4 equal triangles. The triangle program creates triangular meshes with each triangle having an area no greater than the specified area (250 in the above example). Meshinfo is the file containing the dimensions and coordinates of the mesh.

The noisy travel-time file, receivers, sources and mesh files can then be combined into a data input file which is then used to create an inversion input file. The inversion can be run using:

```
./vinv inversion_inputfile
```

This inverts the travel-time data and outputs the following results:

1) Slowness tomogram (.vtu)

2) calculated (predicted) travel-times and residual travel-times (.ele and .vtu)

3) aux and log file.

Data input file (sample:500v_deci_fwd.inp)

```
zdir        1          # specifies the coordinate system
   gridtype     'unstructured' # the type of grid (the other option is 'rectilinear')
   meshfile     'test_mesh_20.node'        # file containing mesh information
   modelfile    'test_mesh_20.ele'         # file containing model information
   neighfile    'test_mesh_20.neigh'           # another file containing mesh information
(unstructured grids only)
```

```
#   split       0           # how to convert from rectilinear to unstructured grid


  sourcesfile   '500v_decimated_sources.node'           # node file specifying the source
locations
  receiversfile '500v_decimated_receivers.node'              # node file specifying the
receiver locations
#   combosfile    '_ttime_data_noisy.ele'         # ele file specifying the source-receiver
combinations
  datafile    '500v_decimated_ttime_data_noisy.ele'



#   ai          1           # attribute index to use as the model
  tmul        1.0         # multiplicative scalar to convert model to slowness
  tadd        0.222         # additiative scalar to convert model to slowness
  trend       0.0         # backgrouund slowness depth trend
  recip       'f'         # set to true ('t') to perform reciprocal modelling
#   nmarch      1           # number of marches to perform in the fast marching
  radius      -10.0         # the initialization radius in the fast marching
#   thresh      0.0         # a threshold on the sensitivity values
  tracemode   'none'        # specifies the type of tracing to perform (if any)
  gradflag    't'         # how to interpolate traveltimes at the receiver locations
  senflag     'f'         # set to true ('t') to calculate the sensitivity matrix
```

```
  senfullflag  'f'        # set to true ('t') to use a full sensitivity matrix instead of sparse
  bruteflag    'f'        # set to true ('t') to perform a brute-force finite-difference sensitivity calculation
  writettimes  't'        # if true ('t') then the traveltimes are written to the output unstructured grid files
  writettypes  'f'        # if true ('t') then the travel types are written to the output unstructured grid files
  writesen     'f'        # if true ('t') then the sensitivity matrix is written to the output unstructured grid files
```

Inversion input file (sample: 500v_deci_inv.inp)

```
# MESH INFORMATION:
  zdir        1           # specifies the coordinate system
  gridtype    'unstructured' # the type of grid (the other option is 'rectilinear')
  meshfile    'test_mesh_20.node'      # file containing mesh information
  modelfile   'test_mesh_20.ele'       # file containing model information
  neighfile   'test_mesh_20.neigh'     # another file containing mesh information (unstructured grids only)
```

```
  #split        0          # how to convert from rectilinear to unstructured grid


# DATA-RELATED OPTIONS:
  ndatasets     1          # number of data sets to invert
  datatype    1 'fat'        # type of data (for a particular data set)
  datainp    1  '500v_deci_fwd.inp'        # input file (for a particular data set)
#   gamma     [] 1.0         # multiplier on the data misfit term (for a particular data set)
  chifact    1  1.5        # normalized target misfit
  chitol    1 0.1        # relative tolerance on the target misfit (for a particular data set)


# REGULARIZATION OPTIONS:
  rotate        'f'        # set to true to rotate the smoothness axes
  alphas       1 0.0          # multiplier on the smallness regularization (for a particular
physical property)
  alpham       1.0         # across-face smoothness regularization multiplier
  alphab     1 1.0         # multiplier on the regularization term (for a particular data set)
  measure0          'ell2'         # specifies the type of measure to use in the smallness
regularization term
  measure1          'ell2'         # specifies the type of measure to use in the smoothness
regularization term
  ekblomp          2.0            # the p-value for the Ekblom measure or total-variation
measure
```

```
   ekblome       0.0          # the epsilon value for the Ekblom measure


# CONSTRAINT OPTIONS:

   usebounds      't'         # set to true ('t') to perform a bound-constrained inversion

   lowervalue  1  -0.221          # lower bound value for the entire mesh

   uppervalue  1  100         # upper bound value for the entire mesh



# JOINT INVERSION OPTIONS


# OPTIMIZATION OPTIONS:

#    maxsteps0      2            # maximum number of model perturbations for each beta
value for beta-search stage

#    maxstepsj      4            # maximum number of model perturbations for each beta
value for joint inversion stage

#    cgtol          1.0E-3       # tolerance for the CG algorithm when solving for the search
direction

   betainit       1.0E-7        # initial beta value

#    minbetasteps   4            # minimum number of steps in beta-search

#    maxbetasteps   48           # maximum number of steps in beta-search

#    betafactmin    1.05         # minimum multiplication factor when adjusting beta

#    betafactmax    2.0          # maximum multiplication factor when adjusting beta
```

```
#    betamult        1.0          # increasing this factor will lead to larger adjustments when
close to the target
#    ratiomult       2.0          # increasing this factor will lead to larger adjustments when
close to the target
# OUTPUT OPTIONS:
#    betaitprefix    'f'          # set to true ('t') to output inversion results at every beta-search
iteration
#    stageprefix     'f'          # set to true ('t') to output inversion results at every iteration in
the joint inversion
#
# When specifying path/file names in the input file, place double quotes around them (e.g.
"../../mesh.txt").




# meshfile, modelfile, neighfile
#    The model may be a 2D or 3D rectilinear or unstructured grid.
#    The unstructured grid should contain triangular cells in 2D and tetrahedral cells in 3D.
#     For an unstructured grid, the meshfile and modelfile should be .node and .ele files
respectively
```

```
#      and the optional neighfile a .neigh file (if neighfile='null' then the neighbour information is calculated automatically).
#    For a rectilinear grid, the meshfile should be UBC-GIF format files (modelfile and neighfile are not used).
#
# split
#   This parameter is only used with a rectilinear grid.
#   A value of 0 splits rectangles symmetrically into four triangles (only applicable to 2D grids).
#   A value of +/-1 splits rectangles into two triangles and prisms into five tetrahedra with alternating splitting in neighbours.
#   A value of +/-2 splits rectangles into two triangles with the same splitting everywhere.
#   For the latter two, the sign determines the geometry of the asymetric splitting.
#
# ---- DATA-RELATED PARAMETERS ----
#
# ndatasets, datatype, datainp
#    Options for datatype are:
#      gz  - vertical gravity data
#      gg  - gravity tensor data
#      fat - first-arrival traveltime data
#    Each data set has its own input file (datainp).
```

```
#    See the documentation for programs gravity_fwd and seismics_fwd for the data-specific parameters.
#
# ---- REGULARIZATION PARAMETERS ----
#
# initfile, initindex, initvalue
#   The initindex column in the initfile (.ele or UBC-GIF file) is used as the initial model.
#   If initfile is specified as 'null' then the initial model value is initvalue for the entire mesh.
#
# reffile, refindex, refvalue
#    The refindex column in the reffile (.ele or UBC-GIF file) is used as the reference model.
#   If reffile is specified as 'null' then the reference model value is refvalue for the entire mesh.
#
# wsfile, wsindex
#   The wsindex column in the wsfile (.ele or UBC-GIF file) is used for the smoothness weights.
#   If wsfile is specified as 'null' then the smallness weights are 1.0 for the entire mesh.
#
# rotate
```

Directional smoothness operators (along each Cartesian axis) are always used for the smoothness on a rectilinear grid.

On an unstructured grid, directional smoothness operators are only used if rotate is set to true ('t').

#

wmfile, wmindex

The wmindex column in the wmfile (simple text file) is used for the across-face smoothness weights.

If wmfile is specified as 'null' then the across-face smoothness weights are 1.0 for the entire mesh.

#

weightsfile, wzindex, strikeindex, dipindex, tiltindex, strikevalue, dipvalue, tiltvalue

The wzindex column in the weightsfile (.ele or UBC-GIF file) is used for the z-direction cell-centred smoothness weights.

If weightsfile is specified as 'null' then the cell-centred smoothness weights are 1.0 for the entire mesh.

The strikeindex, dipindex and tiltindex columns in the weightsfile are used to specify the rotation of the smoothness axes.

If weightsfile is specified as 'null' then strikevalue, dipvalue and tiltvalue specify the rotations for the entire mesh.

The rotation parameters are only used if rotate is set to true ('t').

#

```
# measure0, measure1
#    Possible options are:
#    'ell2'    - the standard, sum-of-squares, L2 norm
#    'ekblom'  - the Ekblom measure
#    'totvar'  - the total variabion measure (can only be used for the measure1 and then only
if
#              directional smoothness operators are being used)
#     'compact' - the minimum-support measure (don't use this, for no other reason that I
don't like it)
#
# ---- CONSTRAINT PARAMETERS ----
#
# boundsfile, lowerindex, upperindex, lowervalue, uppervalue
#    The lowerindex and upperindex columns in the boundsfile (.ele or UBC-GIF file) are
used for the lower and upper bounds.
#    If boundsfile is specified as 'null' then the lower and upper bounds are lowervalue and
uppervalue for the entire mesh.
#
# ---- JOINT INVERSION PARAMETERS ----
#
# alphaj
#    Typically only set to 1.0 or 0.0.
```

```
#
# clusters, spreads, rotations
#    String buffers specifying the cluster information.
#    For example, if the first data set is gravity data and the second traveltime data, and there are three clusters at
#    (density,slowness) coordinates of (0.0,0.2), (0.5,0.3) and (1.0,0.4) then you will have the following lines in the input file:
#       clusters 1 "0.0 0.5 1.0"
#       clusters 2 "0.2 0.3 0.4"
#    The spreads are defined similarly.
#    The rotations specification assumes that there are only two data sets and an error will occur otherwise.
#
# searchr
#    If set to false ('f') to avoid ratio search for beta then the final misfits may not be as close to their targets as requested.
#
# ---- OPTIMIZATION PARAMETERS ----
#
# betainit
#    When there are multiple data sets, all beta values are initially set to betainit.
#
```

```
# ---- OUTPUT PARAMETERS ----
#
# betaitprefix
#     The names of the files are *_beta###.* where ### is an integer value indicating the
iteration number in the beta-search.
#
# stageitprefix
#     The names of the files are *_stage###.* where ### is an integer value indicating the
iteration number in the joint inversion.
```

The inversion codes used were supplied by Dr. Peter Lelièvre.

The triangular mesh code was supplied by Jonathan Richard Shewchuk